Magnetohydrodynamic equilibrium and stability in rotating tokamak plasmas

by

Omar Eulogio López Ortiz

A dissertation submitted to the Graduate Faculty of
Auburn University
in partial fulfillment of the
requirements for the Degree of
Doctor of Philosophy

Auburn, Alabama
May 4, 2019

Keywords: Tokamak, plasmas, equilibrium, stability, flows, MHD

Approved by

Luca Guazzotto, Chair, Physics Professor
Yu Lin, Physics Alumni Professor
David Maurer, Physics Professor
Edward Thomas, Jr., Charles W. Barkley Endowed Professor in Physics
Hans-Werner van Wyk, Mathematics and Statistics Assistant Professor

Abstract

Tokamak plasmas display finite macroscopic rotation in standard machine operation. Yet, the theoretical understanding of stationary states is lacking as compared to static configurations. In this work, we investigate the magnetohydrodynamic equilibrium and stability properties of high-beta tokamak plasmas flowing at a significant fraction of the sound speed.

In the equilibrium part, we introduce a new family of analytical solutions of the Grad-Shafranov-Bernoulli system with diffuse flows in both the toroidal and poloidal directions. Furthermore, our solution allows finite plasma shaping, making it suitable to model present-day tokamak devices. The solution strategy consists of a combination of a variational perturbative scheme in terms of the inverse aspect ratio, a boundary perturbation approach in terms of the triangularity and the Green's function method. While the equilibrium solution corresponding to a circular cross-section is given in closed-form, those for elliptical and D-shaped scenarios are provided in a series-form in terms of Mathieu functions, even so, they can accommodate experimentally relevant values for elongation and triangularity. All solutions show excellent performance when benchmarked against the code FLOW.

As an example of the applicability of our analytical equilibrium for the circular cross-section, we perform a linear stability analysis focusing on the development of ideal external kink modes and resistive wall modes for a purely toroidal velocity profile. The stability problem is expressed as a set of algebraic equations which incorporate a kink mode drive for instabilities and resistive wall effects, while pressure and shear-flow drives are captured at the eigenmode equation level. Solutions are found by a multidimensional shooting method for the coupled side-bands. Results are compared against a sharp-boundary model with a solid body rotation from the literature. Although, in general, results indicate that the qualitative character of the instabilities under study in the presence of a diffuse or a solid body rotation are similar, rotation has a stronger destabilizing effect in the former model. Arguably, this difference is due to a global shear-flow drive effect.

Acknowledgments

Above all, I would like to thank my advisor, Prof. L. Guazzotto, for his continuing support, insight, patience, and optimism these years. I understand better how professional physicists do their living because of him.

Prof. R. Betti graciously provided further details on a rotating-toroidal-resistive-plasma model of his, his notes have been illuminating.

I would like to acknowledge Profs. Y. Lin, D. A. Maurer, E. Thomas and Dr. H.-W. van Wyk for going through this work, but also for conversations I have had with them as his student. I am grateful to the physics department at Auburn University, but I would particularly like to thank Profs. J. D. Hanson and J. Dong, Dr. E. C. Howell (now at Tech-X), C. A. Johnson, Y. Zeng and J. Morris for their help or advice (in plasma research and/or administrative matters) at different points during my Ph.D.

Finally, I thank the USA Department of Energy, which has funded this work.

Table of Contents

List of Figures

List of Tables

Chapter 1

Introduction

1.1 Motivation

The immediate aim of the fusion energy enterprise is to create a reactor where light nuclei carry out enough fusion reactions to sustain a net positive power output. The thermonuclear approach to fusion consists in heating up light nuclei until their thermal energies are sufficient to overcome the Coulomb's potential barrier in head-on collisions. Among fusion reactions between light species like deuterium (D), tritium (T) and Helium-3 (^{3}He), the deuterium-tritium one:

$$D + T \rightarrow {}^{4}He(3.5\ MeV) + n(14.1\ MeV), \tag{1.1}$$
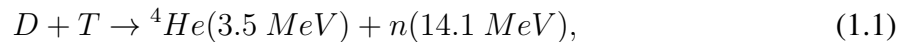
has a larger cross-section over a wide temperature range, making it the most technologically feasible. In classical energy balance considerations, the fusion energy production has to compensate for losses (Bremsstrahlung and to the reactor walls) and an optimum trade is reached when the fuel is heated up around $14\ keV$ [1] [1]. At such temperature, the fuel becomes an ionized state dominated by a collective behavior, i.e., a plasma.

Charged particles describe, to a first approximation, helical paths around magnetic field lines. This principle is the basis for the magnetic-confinement experimental line. Reversed-field pinches, Z-pinches, magnetic mirrors, stellarators, tokamaks and so on, all use this fact as the underlying confinement idea. In this thesis, we explore some characteristics of plasma configurations in tokamaks, one of the front-runners experimental concepts.

---

[1] By "optimum trade" we refer to the "ignition condition" where, in steady state, the ^{4}He power heating is larger than Bremsstrahlung and thermal conduction losses [2]. However, as recently indicated [3], this figure of merit might be insufficient.

Tokamak plasmas are typically composed of $\sim 10^{20} - 10^{22}$ charged particles; their statistical evolution being described by a kinetic model for the electron and ion distribution functions. Energy transport, plasma heating, and current drive are just some examples of phenomena for which a kinetic description is necessary. Yet, if the main interest is to evaluate the forces that keep the bulk of the plasma in place, that is, the overall equilibrium and stability properties, a simplified model is in order. The magnetohydrodynamic (MHD) model for a plasma constitutes a fluid-like description of machine size effects ($\sim 1\ m$), for phenomena evolving in the $\sim \mu s$ time scale, with characteristic velocities comparable to the ion thermal speed ($\sim 500\ km/s$). In general, MHD stability imposes the principal operational limits in tokamaks: maximum current [4, 5], plasma pressure [6, 7], and pressure gradient [8, 9]; surpassing MHD limits is associated with the onset of major disruptions [10]. These limits, in turn, constrain the maximum achievable power output, thus their importance. The tokamak equilibrium and stability considerations presented in this work are based on the MHD model.

In this introductory chapter, we cover some aspects of plasma confinement in tokamaks. In section 1.2 we introduce tokamak geometric parameters and figures of merit to be used throughout the rest of the thesis. A brief description of the necessity of a helical magnetic field in a tokamak and its mathematical description is presented in sections 1.2.2 and 1.2.3, respectively. The MHD model is introduced in section 1.3. Then, the MHD equilibrium and stability concepts are covered in sections 1.3.1 and 1.3.2, respectively. Finally, an overview of the present work is provided in section 1.4.

1.2 Tokamaks

1.2.1 Basic geometric parameters

Tokamaks are toroidally-shaped magnetic confinement devices with a global symmetry in the toroidal direction. As an instance, a tokamak with a circular cross-section is shown in figure 1.1. In actuality, high-performance experiments posses non-circular cross sections like the one illustrated in figure 1.2. The shape of the plasma cross-section is determined by reasons related to equilibrium, stability, and transport. In particular, elongated and "D-shaped" plasmas show

an improved energy confinement time [11], and an increase in both pressure [6] and density stability limits (Greenwald density limit) [12]. Still, arbitrarily increasing the elongation has a detrimental effect on plasma performance due to the onset of vertical MHD instabilities [13].

Coming back to figure 1.1, we introduce two right-handed systems to be used through this work: (R, φ, Z) and (r, φ, θ). Here, the Z axis is the major axis, the minor axis is a circular circuit that runs through the toroid. These axes characterize two basic directions: the toroidal direction (φ) which is parallel to the minor axis and the poloidal direction (θ) which wraps around the minor axis. R is the radial distance from the major axis, while r is the radial distance from the minor axis. The major radius (R_o) is the distance between the major axis and the minor axis, the minor radius (a) is the distance between the minor axis and the plasma edge. The inverse aspect ratio

$$\epsilon \equiv \frac{a}{R_o},$$

(1.2)

is a figure of merit typically employed as an expansion parameter in analytical theories.
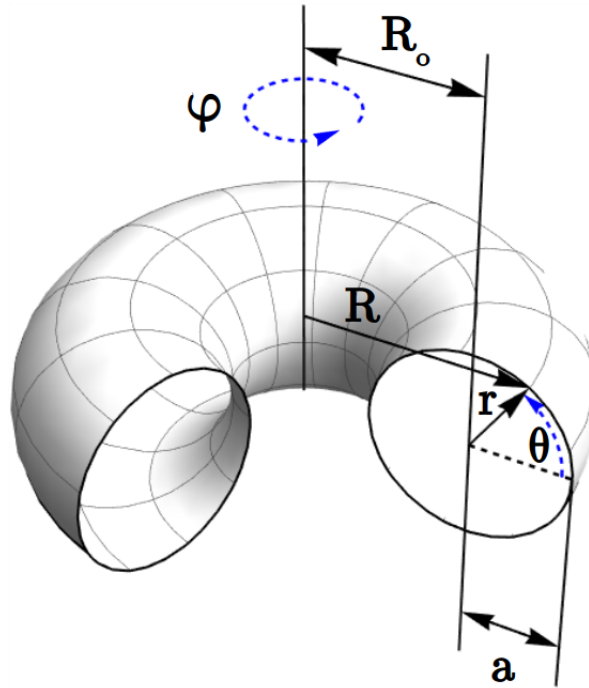
Figure 1.1: Tokamak configuration and standard coordinate systems.

Figure 1.2 illustrates a D-shaped configuration. Here, κ is the elongation and δ the so-called triangularity. This shape is parametrized by

$$R = Ro + a \cos\left(\tau + \alpha \sin\tau\right),$$
$$Z = \kappa \sin\tau,$$

(1.3)

where $\tau \in [0, 2\pi]$ and

$$\alpha \equiv \sin^{-1}\delta.$$

(1.4)

This parametrization will be useful in section 2.9.1.
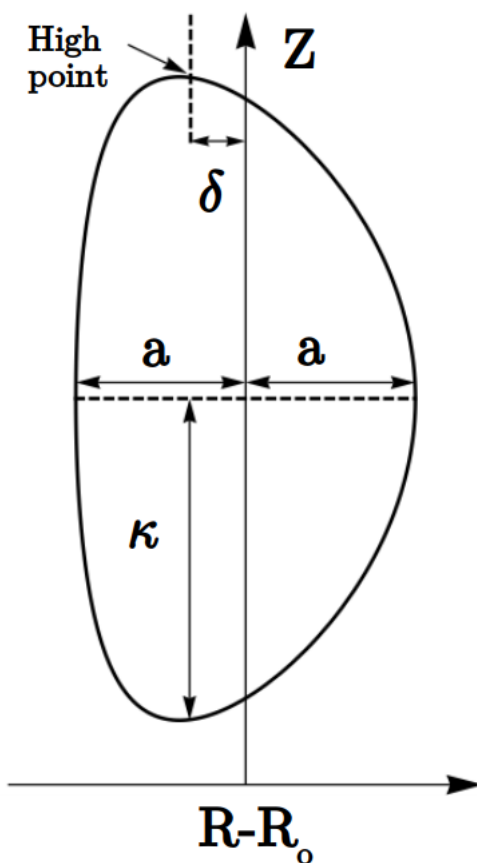
Figure 1.2: D-shape geometry. Based on [14].

1.2.2 The need for a helical magnetic field configuration

The toroidal magnetic field is the dominant component in a tokamak and is produced by a set of poloidal coils and, from a simple application of Ampère's law, it follows that its magnitude decreases as $1/R$. Even though particles follow magnetic field lines to a first approximation, the

inherent curvature and spacial variation of the toroidal field renders it insufficient for particle confinement. This is explained next.

Let us start by assuming a configuration with purely toroidal magnetic field. From single particle dynamical considerations, it is concluded that both the transverse gradient of the toroidal magnetic field and its curvature produce particle drifts which tend to build-up a vertical charge separation (in the Z direction). For a particle of mass m_j and charge q_j, the "∇B-drift" is

$$\boldsymbol{v}_{\nabla B} = \frac{m_j v_\perp^2}{2q_j} \frac{\boldsymbol{B}_\varphi \times \nabla B_\varphi}{B_\varphi^3},\qquad(1.5)$$

the parallel ($v_\parallel$) and perpendicular ($v_\perp$) velocity projections being taken with respect to the background magnetic field ($\boldsymbol{B}_\varphi$), while the curvature drift is

$$\boldsymbol{v}_R = \frac{m_j v_\parallel^2}{q_j B_\varphi^2} \frac{\boldsymbol{R}_c \times \boldsymbol{B}_\varphi}{R_c^2},\qquad(1.6)$$

where $\boldsymbol{R}_c$ is a vector which goes from the magnetic field line's center of curvature to the instantaneous particle's position. Equations 1.5 and 1.6 can be easily derived by considering a test particle in the presence of external fields, due to their charge dependence, it is clear that particles with different polarity undergo opposite drifts. Actually, these drifts are directed in the Z direction, therefore, they generate a vertical separation of charge. As a result, a corresponding vertical electric field is generated, which, together with the toroidal magnetic field, causes yet another drift

$$\boldsymbol{v}_E = \frac{\boldsymbol{E} \times \boldsymbol{B}_\varphi}{B_\varphi^2},\qquad(1.7)$$

but this time independent of the charge polarity and directed outwards. Therefore, a toroidal magnetic field by itself is unable to avoid the overall movement of a plasma column in the outward direction and the subsequent loss in confinement when it reaches the material wall.

In a tokamak, a magnetic field in the poloidal direction ($\boldsymbol{B}_p$) is generated by driving a toroidal current. The superposition of the toroidal magnetic field with the poloidal one causes magnetic field lines to twist around the plasma column. In this way, charges that would otherwise be accumulated on opposite sides are mixed together as they move along the helical

5

magnetic field and the spatial separation of charge is avoided. Particles still drift vertically while traveling in a helical path, yet, the net vertical drift cancels to zero (see, for example, [15]).

1.2.3   Magnetic surfaces

To a good approximation, tokamaks are symmetric in the toroidal direction (axisymmetry). This has strong implications in the form of the equilibrium quantities and, in particular, in the form of the equilibrium helical magnetic field. Mathematically, axisymmetry is expressed as

$$\frac{\partial f}{\partial \varphi} = 0, \tag{1.8}$$

where f is an arbitrary equilibrium quantity. From the magnetic potential relation

$$\boldsymbol{B} = \nabla \times \boldsymbol{A}, \tag{1.9}$$

and defining the stream function Ψ as a scaled component of the magnetic potential according to

$$\Psi(R, Z) \equiv RA_\varphi(R, Z), \tag{1.10}$$

it follows that the magnetic field can be written in a very special form

$$\boldsymbol{B} = \nabla\Psi \times \nabla\varphi + B_\varphi \hat{\boldsymbol{e}}_\varphi. \tag{1.11}$$

The contour labels of Ψ define concentric toruses where the magnetic field lines reside, i.e., magnetic surfaces. The limiting central torus is just a magnetic field line, i.e., a "magnetic axis". The poloidal magnetic flux between the magnetic axis and an arbitrary flux surface is $\Psi_p = 2\pi\Psi$; therefore, Ψ is also referred to as the "poloidal flux". Any quantity of the form $f = f(\Psi)$ is referred to as a being a "flux quantity" or "surface quantity". As will be seen in section 1.3.1, these quantities play a major role in describing equilibria in tokamaks.

1.3 The ideal magnetohydrodynamic model

The magnetohydrodynamic (MHD) model of a plasma is a description suited for low-frequency, long-wavelength macroscopic phenomena. It can formally be obtained from the set of Boltzmann equations for electrons and ions together with Maxwell's equations by taking successively higher velocity moments, passing through an intermediate two-fluid description, and then assuming a high collisionality regime, among other approximations [16]. In ideal MHD, the state of the system is characterized by the plasma velocity ($\boldsymbol{u}$), the magnetic field ($\boldsymbol{B}$), the mass density (ρ), and the kinetic pressure (p). The current density ($\boldsymbol{J}$) and the electric field ($\boldsymbol{E}$) are regarded as intermediate variables. The resulting model can be thought of as describing the coupling between a compressible, adiabatic gas with infinite conductivity and pre-Maxwell's equations:

$$\frac{\partial \rho}{\partial t} + \nabla \cdot (\rho \boldsymbol{u}) = 0, \tag{1.12}$$

$$\rho \left(\frac{\partial \boldsymbol{u}}{\partial t} + \boldsymbol{u} \cdot \nabla \boldsymbol{u} \right) = -\nabla p + \boldsymbol{J} \times \boldsymbol{B}, \tag{1.13}$$

$$\frac{d}{dt} \left(p \rho^{-\gamma} \right) = 0, \tag{1.14}$$

$$\frac{\partial \boldsymbol{B}}{\partial t} = -\nabla \times \boldsymbol{E}, \tag{1.15}$$

$$\nabla \times \boldsymbol{B} = \mu_o \boldsymbol{J}, \tag{1.16}$$

$$\nabla \cdot \boldsymbol{B} = 0, \tag{1.17}$$

$$\boldsymbol{E} + \boldsymbol{u} \times \boldsymbol{B} = \boldsymbol{0}, \tag{1.18}$$

where μ_o is the permeability of free space and $\gamma = 5/3$ is the ratio between specific heats. Among these equations, ideal Ohm's law (Eq. 1.18) leads to a constraint on the allowed fluid motion known as the "frozen-in-field" theorem: the magnetic flux across an arbitrary open surface moving with the fluid remains the same [16], which is a very important feature of ideal MHD.

1.3.1 MHD axisymmetric equilibrium

As shown before, axisymmetry has strong consequences on the form of the equilibrium magnetic field (Eq. 1.11). The same is true for all equilibrium quantities and their governing equations. In fact, the equilibrium is specified by five flux quantities $F(\Psi), S(\Psi), H(\Psi), \Omega(\Psi)$ and $\Phi(\Psi)$ commonly referred to as "free functions". Once they are given, it is possible to solve the pair of equations known as the Grad-Shafranov-Bernoulli (GSB) system:

$$\frac{1}{\mu_o} \nabla \cdot \left[\left(1 - \frac{\Phi^2}{\rho} \right) \frac{\nabla \Psi}{R^2} \right] = -\frac{B_\varphi}{\mu_o R} \frac{dF}{d\Psi} - \frac{1}{\sqrt{\mu_o}} \boldsymbol{u} \cdot \boldsymbol{B} \frac{d\Phi}{d\Psi} - \rho R u_\varphi \frac{d\Omega}{d\Psi} - \rho \frac{dH}{d\Psi} + \frac{\rho^\gamma}{\gamma - 1} \frac{dS}{d\Psi}, \quad (1.19)$$

$$\frac{\Phi^2 B^2}{2\mu_o \rho^2} - \frac{R^2 \Omega^2}{2} + \frac{\gamma S \rho^{\gamma-1}}{\gamma - 1} = H, \quad (1.20)$$

for the poloidal flux and mass density [17, 18, 19]. This formalism constitutes a non-linear coupled system of a partial differential equation (PDE) and an algebraic equation. Although Eq. 1.19 is found to be elliptic for standard tokamak operation, it may possess hyperbolic regions for certain rotation profiles [18, 19, 20]. While the component of the momentum equation along $\nabla \Psi$ gives rise to the Grad-Shafranov equation (1.19), the projection along $\boldsymbol{B}$ leads to Bernoulli's equation (1.20). On the other hand, the projection along $\hat{\boldsymbol{e}}_\varphi$ sets the form of the toroidal magnetic field:

$$B_\varphi = \frac{F + \sqrt{\mu_o} R^2 \Phi \Omega}{R \left(1 - \Phi^2/\rho \right)}. \quad (1.21)$$

A combination of ideal Ohm's and Faraday's laws implies that streamlines are tangent to magnetic surfaces

$$\boldsymbol{u} = \frac{\Phi \boldsymbol{B}}{\sqrt{\mu_o \rho}} + R \Omega \hat{\boldsymbol{e}}_\varphi. \quad (1.22)$$

Finally, the kinetic pressure is given by

$$p = S\rho^{\gamma}. \tag{1.23}$$

The static ($\boldsymbol{u} = 0$) equilibrium's description is simpler than the stationary one ($\boldsymbol{u} \neq 0$). This is mainly due to the disappearance of hyperbolic regions but also because the problem consists in solving a single PDE instead of a system of equations. In this static regime, equilibrium configurations are governed by the Grad-Shafranov / Lüst-Schlüter equation [21, 22, 23]:

$$\nabla \cdot \left[\frac{\nabla \Psi}{R^2} \right] = -\frac{F}{R^2} \frac{dF}{d\Psi} - \mu_o \frac{dp}{d\Psi}. \tag{1.24}$$

It depends on only two free functions: $F(\Psi)$, which is proportional to the poloidal current and $p(\Psi)$, which is the plasma pressure. Much of the theoretical understanding of tokamak MHD confinement obtained in previous decades has originated by studying the static regime. Analytic static solutions are abundant [24, 25, 16, 26, 27, 28, 29, 30, 31, 32, 33, 14], and essentially all fusion laboratories have constructed their own equilibrium solvers.

Tokamak plasmas do present finite equilibrium rotation values, in fact, macroscopic flows can reach a significant fraction of the sound speed. Rotation is typically induced by plasma heating as neutral beam injection (NBI) or radio-frequency (RF) heating [34, 35]. Poloidal rotation shear is related to the transition from low to high modes in confinement (L-H transition) [36, 37]. As illustrated in [38], failure to self-consistently incorporate the effect of flow at the equilibrium level can lead to dissimilar results "even at modest flows speeds". Thus, rotation is an important effect that should be included in tokamak equilibrium calculations from the outset.

1.3.2   MHD linear stability

In general, steady-state operation is considered to be an important requirement of future fusion plants [39, 40]. Currently, record times of continuous operation have been reported to last as long as $30 \; s$ in the high-confinement regime of EAST tokamak [41], similarly, other machines

routinely operate in the second time scale. In this context, the aim of MHD is not only to model equilibrium states but, equally important, to determine their stability properties. Given that the characteristic MHD time ($\tau_{MHD} \sim a/V_{Ti}$), as estimated by the minor radius (a) and the ions thermal velocity (V_{Ti}), is of the order of microseconds, the only experimentally realizable configurations are the ones that, first of all, are robust against macroscopic fluctuations, i.e., MHD stable.

In static ideal MHD, instabilities develop either because of pressure gradients or parallel currents (to the equilibrium magnetic field) [16]. Much of our physical intuition about instabilities in fusion devices comes from the static case, where it can be proved that incompressible perturbations are the most unstable, but this is not guaranteed to happen in stationary scenarios anymore. In stationary configurations centrifugal, Doppler, Coriolis, and sheared-flow effects come into play both at the equilibrium and stability levels.

The most common definition of stability employed in MHD is that of linear stability [42], although other definitions such as Lyapunov stability [42, 43, 44], are possible. In the MHD linearization procedure any given quantity $Q(\boldsymbol{r}, t)$ is expressed as a sum of a time-independent part $Q_0(\boldsymbol{r})$ and a small perturbation $\widetilde{Q}(\boldsymbol{r}, t)$ about the equilibrium position:

$$Q(\boldsymbol{r}, t) = Q_0(\boldsymbol{r}) + \widetilde{Q}(\boldsymbol{r}, t), \quad \text{where} \ \ |\widetilde{Q}| << |Q_0|, \tag{1.25}$$

next, this decomposition is substituted back into the MHD Eqs. 1.12-1.18 and all terms quadratic or higher order in the small quantities are neglected. Continuing, it is assumed that

$$\widetilde{Q}(\boldsymbol{r}, t) = \widetilde{Q}(\boldsymbol{r})e^{-i\omega t}. \tag{1.26}$$

In this way, the original problem is cast as a linear system in the small quantities, to be solved for the characteristic eigenfrequencies (ω). The MHD equilibrium state is said to be exponentially stable if $\mathbb{Im}\{\omega\} \leq 0$ and exponentially unstable if $\mathbb{Im}\{\omega\} > 0$.

In the formalism introduced by Frieman and Rotenberg [45] disturbances in the velocity, the magnetic field, pressure, and density (denoted with a tilde) are expressed in terms of equilibrium quantities (without a tilde) and the perturbed plasma displacement ($\boldsymbol{\xi}$) away from the equilibrium trajectory according to the following expressions:

$$\widetilde{\boldsymbol{V}} = \frac{\partial \boldsymbol{\xi}}{\partial t} + \boldsymbol{V} \cdot \nabla \boldsymbol{\xi} - \boldsymbol{\xi} \cdot \nabla \boldsymbol{V}, \tag{1.27}$$

$$\widetilde{\boldsymbol{B}} = \nabla \times (\boldsymbol{\xi} \times \boldsymbol{B}), \tag{1.28}$$

$$\widetilde{p} = -\gamma p \nabla \cdot \boldsymbol{\xi} - \boldsymbol{\xi} \cdot \nabla p, \tag{1.29}$$

$$\widetilde{\rho} = -\rho \nabla \cdot \boldsymbol{\xi} - \boldsymbol{\xi} \cdot \nabla \rho. \tag{1.30}$$

A Fourier decomposition in time (as given by Eq. 1.26) transforms the momentum equation into the non-linear (in ω) vectorial eigenvalue equation:

$$\boldsymbol{G}(\boldsymbol{\xi}) - 2\omega U(\boldsymbol{\xi}) + \rho \omega^2 \boldsymbol{\xi} = 0, \tag{1.31}$$

where the Doppler-Coriolis operator (U) represents the advection of the plasma perturbation due to the equilibrium flow

$$U(\boldsymbol{\xi}) \equiv -i\rho \boldsymbol{V} \cdot \nabla \boldsymbol{\xi}, \tag{1.32}$$

and the generalized force operator ($\boldsymbol{G}$) has contributions due to pressure gradients, magnetic and centrifugal forces, as well as an additional advective term

$$\boldsymbol{G}(\boldsymbol{\xi}) \equiv -\nabla \widetilde{p} + \boldsymbol{J} \times \widetilde{\boldsymbol{B}} + \widetilde{\boldsymbol{J}} \times \boldsymbol{B} + \nabla \cdot (\boldsymbol{\xi} \rho \boldsymbol{V} \cdot \nabla \boldsymbol{V}) - \rho (i\boldsymbol{V} \cdot \nabla)^2 \boldsymbol{\xi}. \tag{1.33}$$

For the eigenvalue problem 1.31 to be well-defined, it has to be supplied with appropriate boundary conditions. For the study of fixed-boundary modes (internal modes) it is required that

the normal component of the plasma perturbation vanishes at the plasma edge

$$\boldsymbol{\xi}_n(a) = 0, \tag{1.34}$$

(where the subscript "n" denotes the component normal to the boundary) while regularity at $r = 0$ is also imposed. On the other hand, for the study of free-boundary modes (external modes) the perturbed value of the total pressure

$$\widetilde{P} \equiv \widetilde{p} + \frac{B\widetilde{B}_{\parallel}}{\mu_o} + \xi_n \nabla_n \left(p + \frac{B^2}{2\mu_o} \right), \tag{1.35}$$

($\widetilde{B}_{\parallel}$ being the perturbed magnetic field parallel to the equilibrium magnetic field) should be continuous at the plasma edge [46, 16, 47]:

$$\left[\left[\widetilde{P}\right]\right]_a = 0. \tag{1.36}$$

Additionally, the normal component of the perturbed magnetic field should also be continuous at the plasma edge

$$\left[\left[\widetilde{B}_n\right]\right]_a = 0, \tag{1.37}$$

and regularity at the origin is required as well. As usual, a double bracket represents a jump of a given quantity

$$[[f]]_a \equiv \lim_{h \to 0} \left(f(a+h) - f(a-h) \right). \tag{1.38}$$

The contributions in 1.35 should make intuitive sense: the first two terms measure the variation of the total pressure at a fixed position, while the term proportional to the plasma displacement is what allows the boundary to move. In chapter 3, we will discuss these boundary conditions in further detail.

Formally, what is done is to endow the linear stability problem with the structure of a Hilbert space [47] by defining the inner product between arbitrary allowed perturbations $\boldsymbol{\xi}$ and $\boldsymbol{\eta}$ as

$$\langle \boldsymbol{\eta} | \boldsymbol{\xi} \rangle \equiv \frac{1}{2} \int \rho \boldsymbol{\eta}^* \boldsymbol{\xi} d^3 r, \tag{1.39}$$

and requiring the quantity

$$I[\boldsymbol{\xi}] \equiv \langle \boldsymbol{\xi} | \boldsymbol{\xi} \rangle , \tag{1.40}$$

to be finite [2], which is to say that the kinetic energy; defined as the quadratic form

$$K[\boldsymbol{\xi}] \equiv \frac{1}{2} \int \rho \frac{\partial \boldsymbol{\xi}^*}{\partial t} \cdot \frac{\partial \boldsymbol{\xi}}{\partial t} d^3 r = \frac{|\omega|^2}{2} I[\boldsymbol{\xi}], \tag{1.41}$$

should be bounded.

The non-linear eigenvalue problem 1.31 is self-adjoint. We recall that the concept of self-adjointness depends on both the functional space the operator acts on (in this case, the space of allowed plasma perturbations) and, equally important, on the imposed boundary conditions [48]. Changing the boundary conditions, in general, destroys the self-adjointness nature of an operator. Under the inner product 1.39 and either the boundary conditions for internal modes 1.34 or for external modes 1.36-1.37, it is then shown that $\rho^{-1}\boldsymbol{G}$ and $\rho^{-1}U$ are self-adjoint [45, 47]. Self-adjointness is related to energy conservation, and is the basis for the introduction of Goedbloed's Spectral-Web-Method in appendix E.1.

The key difference between static and stationary equilibrium configuration is that in the former case eigenvalues are either purely real or purely imaginary, while in the latter case eigenvalues are genuinely complex in general. This is easy to see. By introducing two extra quadratic forms: one associated with the potential energy

$$W[\boldsymbol{\xi}] = -\frac{1}{2} \int \boldsymbol{\xi}^* \cdot \boldsymbol{G}(\boldsymbol{\xi}) d^3 r, \tag{1.42}$$

and the other related to the Doppler-Coriolis operator

$$V[\boldsymbol{\xi}] = \frac{1}{2} \int \boldsymbol{\xi}^* \cdot U(\boldsymbol{\xi}) d^3 r, \tag{1.43}$$

we can cast eigenvalue problem 1.31 as

$$I[\boldsymbol{\xi}]\omega^2 - V[\boldsymbol{\xi}]\omega - W[\boldsymbol{\xi}] = 0. \tag{1.44}$$

---

[2]This excludes the consideration of the continuum, where eigenvectors are not normalizable.

The quantities $W[\boldsymbol{\xi}]$, $V[\boldsymbol{\xi}]$ and $I[\boldsymbol{\xi}]$ are real for all allowed perturbations. In static configurations $V[\boldsymbol{\xi}] = 0$, therefore, ω^2 is real, i.e., ω is either purely real or purely imaginary. On the other hand, in stationary configurations $V[\boldsymbol{\xi}] \neq 0$ and ω is genuinely complex in the general case.

1.4 Overview of the present work

Magnetically confined plasmas can display significant rotation levels throughout standard machine operation, for example, a deuterium plasma has reached toroidal velocities of about 40% the sound speed in the DIII-D tokamak [49, Fig 9] and the National Spherical Torus Experiment (NSTX) has reported toroidal velocities of about half the Alfvén speed [50, p. 641]. On the other hand, poloidal rotation shear is related to the transition from the low- to the high-mode in confinement (L-H transition) [51] or the quiescent H-mode (QH-mode) [52]. High confinement modes facilitate the operation of machines in states of high kinetic pressure (p) relative the externally imposed magnetic pressure ($B_o^2/2\mu_o$); states referred to as "high-β", where $\beta_\varphi \equiv 2\mu_o p/B_o^2$, and which intuitively are favorable in terms of confinement performance.

Although our theoretical understanding of stationary configurations under even the simplest plasma model, ideal MHD, is not as comprehensive as our understanding of static scenarios, there is significant work done on the subject. Theoretical studies include the effect of flow or flow shear on interchange modes [53, 54], on ballooning modes [55, 56], toroidal rotation effects on internal modes [57, 38, 58] and on resistive-wall-modes [59, 60], etc. In a spirit similar to the previous works, we study the stability of external resistive-wall-modes for a high-β plasma with diffuse flowing profiles at a significant fraction of the sound speed. These modes represent the most dangerous MHD instability in a tokamak, by causing the movement of the plasma towards the first wall they lead to the catastrophic termination of the plasma confinement, a scenario referred to as a "disruption" [16].

This work is organized as follows. In chapter 2, MHD stationary axisymmetric states are constructed as solutions of the Grad-Shafranov-Bernoulli system which include both rotation in the toroidal and poloidal direction. We do this by taking advantage of a variational formulation of the equilibrium problem, which is introduced in section 2.3. Under a high aspect ratio approximation, we reduce the equilibrium problem to a linear PDE in section 2.4, which we

solve for circular 2.7 and elliptical cross-sections 2.8 by constructing the corresponding Green's functions (see appendix A). The end result is a closed-form solution for a circular geometry and a series solution in terms of Mathieu function for an elliptical geometry, both of which are then benchmarked against the code FLOW [61] in section 2.6. In section 2.9 the previously constructed Green's functions for the elliptical case are used as the basis to obtain a solution for a D-shaped cross-section. This is done by means of a boundary perturbation technique. As a first step towards studying external modes in the presence of resistive and ideal walls, we construct a self-consistent vacuum equilibrium (section 3.2). The stability problem is approached using the Frieman-Rotenberg's formulation and following Betti's work [60] (section 3.3). In fact, we use a modification of the solid toroidal rotation formalism elaborated in [60] as a "first guess generator" in order to find approximate eigenvalues and eigenmodes for our diffuse equilibrium. Beta-limits for ideal and resistive walls, for static and toroidally rotating plasmas, are then given in section 3.6. Finally, appendices D and E deal with other equilibrium and stability aspects. In two-fluid theory, the ion velocity develops a component normal to magnetic surfaces which is not present in single-fluid ideal MHD, even though we do not consider its stability implications, we provide an approximation of such velocity component based on our single-fluid equilibrium model. In appendix E, we revisit the classical Kelvin-Helmholtz instability studied by Chandrasekhar [62] and we recover his results using a continuous but strongly sheared velocity profile instead of a discontinuous one.

Chapter 2

Construction of a high-beta, analytic axisymmetric equilibrium with poloidal and toroidal diffuse flow profiles in circular, elliptical and D-shaped scenarios.

2.1   Introduction

We have argued that the equilibrium and stability properties of fusion scenarios must be analyzed in a self-consistent way. If sizable background flows are present in axisymmetric devices, they should be included in the equilibrium formulation by solving the Grad-Shafranov-Bernoulli (GSB) set of coupled equations 1.19-1.20.

The first numerical effort to solve the Grad-Shafranov-Bernoulli system corresponds to the CLIO code [63]. Later on, FINESSE [64] was developed for fusion and astrophysical purposes. It has been employed, for example, for solving the system in different elliptic flow regimes and under different cross-sections [65]. FINESSE is used as the equilibrium module in the PHOENIX MHD spectral code [66]. Transonic equilibria, where the poloidal velocity transitions from values below to above the poloidal sound speed, were studied numerically as the result of the FLOW code development [61]. FLOW has also been used to investigate inverted Shafranov-shift scenarios, having a poloidal flow of the order of the poloidal Alfvén speed [67].

The canonical analytic solution for the static Grad-Shafranov equation (Eq. 1.24) in the context of fusion was introduced by Solov'ev [24]. Under a simple choice for the pressure and poloidal current free functions, the equilibrium problem was reduced to an inhomogeneous PDE, which was then solved analytically. Since then, plenty of analytic solutions to

16

the static problem have been obtained (see, for example, [14] and references therein). In contrast, analytic solutions for the stationary problem are scarce, but analytic work has been done nonetheless [18, 68, 69, 70, 71, 72].

Analytic equilibrium solutions are valuable because they provide simple formulas which highlight the interrelation between the competing contributions (centrifugal effects, gradients of pressure, currents, etc.). Analytic solutions can be used as the first stage in a parameter space scan and they are also valuable for code benchmarking.

Analytic solutions of the GSB system are tailored to explore one or other physical regime. The simplifying assumptions needed to make analytical progress are the actual form of the free functions on the poloidal flux and the targeted geometrical boundary. Additionally, a common practice is to expand the governing equations in terms of an intrinsically occurring small parameter to obtain a sequence of subproblems, whose solutions should be easier to compute, and which correspond to successively higher order corrections.

In this chapter, we construct a family of analytic solutions with toroidal and poloidal background diffuse flows for cross-sections which are relevant to existing experiments. We do this by a combination of an expansion in terms of the inverse aspect ratio (Eq. 1.2) and another in terms of the triangularity (Eq. 1.4). The resulting formulation can be implemented in stability analyses and in fact, that is what we do in the next chapter, where external ideal- and resistive-wall-modes are analyzed.

The discussion is organized as follows. The physical regime of interest is specified in section 2.2. In section 2.3, we introduce an alternative formulation of the GSB system, which is then used as the basis for the large aspect ratio approximation in section 2.4. Solutions for a circular and elliptical cross-sections are given in sections 2.7 and 2.8, respectively. Some figures of merit for the circular-cross section are introduced in subsection 2.7.1. Convergence tests against the FLOW code for these scenarios are presented in section 2.6. A solution method for a D-shaped cross-section is built upon the elliptical solution; it is explained in section 2.9. . Results are summarized in 2.10.

2.2 Ordering: defining the relevant regime

It is advantageous for fusion purposes to confine as much pressure given an externally imposed magnetic field. Therefore, our aim is to obtain self-consistent solutions of the GSB system for a high-beta scenario which incorporate both toroidal and poloidal flows.

In high-beta scenarios $\beta_\varphi \sim O(\epsilon)$[1], where the inverse aspect ratio has been defined before (Eq. 1.2) . We will employ the inverse aspect ratio as an expansion parameter. This is a common tool to deal with axisymmetric devices. Experiments like ITER ($R_o \sim 6.2m$, $a \sim 2m$ and $\epsilon \sim 0.32$), DIII-D ($R_o \sim 1.68m$, $a \sim 0.62m$ and $\epsilon \sim 0.36$), ASDEX Upgrade ($R_o \sim 1.65m$, $a \sim 0.65m$ and $\epsilon \sim 0.39$) and CTH in its tokamak-like operation ($R_o \sim 0.75m$, $a \sim 0.29m$ and $\epsilon \sim 0.39$), all have inverse aspect ratios below unity by definition, so that higher-order solutions are progressively smaller ($\epsilon^{n+1} < \epsilon^n \ for \ n = 1, 2, 3...$).

The toroidal velocity will be assumed to scale as $V_\varphi / C_s \sim O(\epsilon^{1/2})$, where

$$C_s \equiv \sqrt{\gamma p_o / \rho_o}, \tag{2.1}$$

is the sound speed, and p_o and ρ_o are the kinetic pressure and mass density at the geometrical axis, respectively. For the poloidal velocity we assume one order smaller, i.e., $V_p \sim \epsilon V_\varphi$. Finally, the poloidal magnetic field is assumed to scale as $B_p / B_o \sim O(\epsilon)$, which implies that the kink safety factor (defined in Eq. 2.37 for a circular cross-section) is of order $q_* \sim O(1)$.

2.3 Variational formulation of MHD axisymmetric equilibrium configurations

The GSB system describes equilibrium states with background flow. Additionally, these states are given as the stationary points of the action G:

$$G \equiv \int \mathcal{L}(\Psi, \rho, \nabla\Psi) R dR dZ, \tag{2.2}$$

---

[1]As opposed to a low-beta or ohmically heated scenario, where $\beta_\varphi \sim O(\epsilon^2)$ [16].

where the associated Lagrangian is defined as

$$\mathcal{L}(\Psi, \rho, \nabla\Psi) \equiv \left(1 - \frac{\Phi(\Psi)^2}{\rho}\right) \frac{|\nabla\Psi|^2}{2R^2\mu_o} + \frac{S(\Psi)\rho^\gamma}{\gamma - 1} - H(\Psi)\rho - \frac{1}{2}\rho R^2 \Omega(\Psi)^2$$
$$- \frac{1}{2\mu_o} \frac{\left[F(\Psi)/R + \sqrt{\mu_o}R\Phi(\Psi)\Omega(\Psi)\right]^2}{[1 - \Phi(\Psi)^2/\rho]}, \tag{2.3}$$

and the generalized coordinates are taken here as the poloidal flux and the mass density [73]. Indeed, a straightforward application of Euler-Lagrange equations:

$$\frac{\partial}{\partial R}\left(\frac{\partial(R\mathcal{L})}{\partial\left(\frac{\partial\Psi}{\partial R}\right)}\right) + \frac{\partial}{\partial Z}\left(\frac{\partial(R\mathcal{L})}{\partial\left(\frac{\partial\Psi}{\partial Z}\right)}\right) = \frac{\partial(R\mathcal{L})}{\partial\Psi}, \tag{2.4}$$

$$\frac{\partial}{\partial R}\left(\frac{\partial(R\mathcal{L})}{\partial\left(\frac{\partial\rho}{\partial R}\right)}\right) + \frac{\partial}{\partial Z}\left(\frac{\partial(R\mathcal{L})}{\partial\left(\frac{\partial\rho}{\partial Z}\right)}\right) = \frac{\partial(R\mathcal{L})}{\partial\rho}, \tag{2.5}$$

leads to the GS and Bernoulli's equations, in that order.

The usefulness of performing an asymptotic analysis of the variational formulation comes from a theorem proved by Hameiri [74]. In particular, this theorem guarantees that by taking the asymptotic expansion at the functional level (Eq. 2.2) it is possible to recover the asymptotic expansion of the GSB system if an appropriate order-by-order variational process is applied. In this sense, the operations "take the variation" and "perform the asymptotic expansion" are commutative. The subtlety is that, after performing the asymptotic expansion at the functional level, it is not immediately clear how to take the variation with respect to the generalized co-ordinates anymore, since these quantities have been expanded as well. The answer is that the variation should be taken with respect to the leading order term in their expansion [74]. In practice, taking the asymptotic expansion first and applying the variational process later, eases the algebraic manipulations.

2.4 Scaling, notation conventions and asymptotic expansion

As a preamble to carrying out the asymptotic expansion, we introduce scaled quantities. In general, scaled quantities will be denoted with an overline, an exception being the poloidal flux; throughout this text, we *always* use (Ψ) to denote the poloidal flux in SI units and (ψ) to

Original [SI units]	=	Scaled	×	Factor
Ψ		ψ		$a^2 B_o$
ρ		$\overline{\rho}$		ρ_o
$\mathbf{B}_p$		$\overline{\mathbf{B}}_p$		ϵB_o
$\mathbf{B}_\varphi$		$\overline{\mathbf{B}}_\varphi$		B_o
$\mathbf{V}_p$		$\overline{\mathbf{V}}_p$		$\epsilon^2 V_{Ao}$
$\mathbf{V}_\varphi$		$\overline{\mathbf{V}}_\varphi$		ϵV_{Ao}
r		$\overline{r}$		a
Z		$\overline{z}$		a
R		$\overline{R}$		R_o
x		$\overline{x}$		a
∇		$\overline{\nabla}$		a^{-1}
$F(\Psi)$		$\overline{F}(\psi)$		$R_o B_o$
$\Omega(\Psi)$		$\overline{\Omega}(\psi)$		$a V_{Ao}/R_o^2$
$\Phi(\Psi)$		$\overline{\Phi}(\psi)$		$\epsilon \sqrt{\rho_o}$
$H(\Psi)$		$\overline{H}(\psi)$		ϵV_{Ao}^2
$S(\Psi)$		$\overline{S}(\psi)$		$\epsilon V_{Ao}^2/\rho_o^{\gamma-1}$
$L(\Psi, \rho, \nabla\Psi)$		$\overline{L}(\psi, \overline{\rho}, \overline{\nabla}\psi)$		$a R_o^2 B_o^2$

Table 2.1: Physical quantities in SI units and associated scaling factors. A given quantity in SI units is obtained by multiplying the scaled one by its corresponding factor. These factors are consistent with the ordering established in section 2.2 and are introduced with the philosophy of ensuring that scaled quantities are not only dimensionless but also of $\sim O(1)$ in the inverse aspect ratio. B_o and ρ_o are the toroidal magnetic field and mass density at the geometrical axis, respectively; $V_{Ao} \equiv B_o/\sqrt{\rho_o \mu_o}$ is the Alfvén velocity. $x \equiv R - R_o$ is a chamber-centered coordinate. The definition of the scaled free functions involves a change of coordinates from Ψ to ψ.

denote its dimensionless form:

$$\Psi(r, \theta) = B_o a^2 \psi(\overline{r}, \theta). \tag{2.6}$$

The complete list of scaled quantities and corresponding scaling factors is given in Table 2.1.

These factors are consistent with the ordering established in section 2.2 and are introduced with

the philosophy of ensuring that scaled quantities are not only dimensionless but also of $\sim O(1)$

in the inverse aspect ratio.

We can then write down expressions for the scaled action

$$\overline{G}(\psi, \overline{\rho}, \overline{\nabla}\psi) = \int \overline{\mathcal{L}}(\psi, \overline{\rho}, \overline{\nabla}\psi)(1 + \epsilon\,\overline{x})\,d\,\overline{x}\,d\,\overline{z}, \tag{2.7}$$

and for the Lagrangian of the system

$$\overline{\mathcal{L}}(\psi, \overline{\rho}, \nabla \psi) = \frac{\epsilon^2 |\overline{\nabla}\psi|^2}{2\overline{R}^2}\left[1 - \frac{\epsilon^2 \overline{\Phi}^2}{\overline{\rho}}\right] - \epsilon \overline{H}\overline{\rho}$$
$$- \frac{1}{2}\frac{\left[F/\overline{R} + \epsilon^2 \overline{R}\,\overline{\Phi}\,\overline{\Omega}\right]^2}{1 - \epsilon^2 \overline{\Phi}^2/\overline{\rho}} + \frac{\epsilon \overline{S}\overline{\rho}^\gamma}{\gamma - 1} - \frac{\epsilon^2 \overline{\rho}\,\overline{R}^2 \overline{\Omega}^2}{2}, \tag{2.8}$$

where $\overline{R} = 1 + \epsilon\,\overline{x}$. Proceeding further, we expand all scaled quantities $(\overline{Q})$ as

$$\overline{Q} = \overline{Q}_0 + \epsilon\,\overline{Q}_1 + \epsilon^2\,\overline{Q}_2 + ..., \quad \text{where} \quad \overline{Q}_k \sim O(1) \quad \text{for} \quad k = 0, 1, 2, ... \tag{2.9}$$

The first three contributions in the Lagrangian expansion are

$$\overline{\mathcal{L}}_0 = \frac{1}{2}\overline{F}_0^2, \tag{2.10}$$

$$\overline{\mathcal{L}}_1 = \overline{F}_0\left(\overline{F}_0'\psi_1 - \overline{x}\overline{F}_0 + \overline{F}_1\right) + \overline{H}_0\overline{\rho}_0 - \frac{\overline{S}_0\overline{\rho}_0^\gamma}{\gamma - 1}, \tag{2.11}$$

and

$$\overline{\mathcal{L}}_2 = \frac{1}{2}\overline{F}_0^2\left[\frac{\overline{\Phi}_0^2}{\overline{\rho}_0} + 3\overline{x}^2\right] + \overline{F}_2\overline{F}_0 + \frac{1}{2}\overline{F}_1^2 + \overline{F}_0\overline{\Phi}_0\overline{\Omega}_0 + \frac{1}{2}\psi_1^2\left[\overline{F}_0'^2 + \overline{F}_0\overline{F}_0''\right]$$
$$+ \overline{\rho}_1\left[\overline{H}_0 - \frac{\gamma\overline{S}_0\overline{\rho}_0^{\gamma-1}}{\gamma - 1}\right] + \psi_1\left[\overline{H}_0'\overline{\rho}_0 - \frac{\overline{S}_0'\overline{\rho}_0^\gamma}{\gamma - 1} + (\overline{F}_0\overline{F}_1)' - 2\overline{x}\overline{F}_0\overline{F}_0'\right] \tag{2.12}$$
$$+ \left[\overline{H}_1 + \frac{1}{2}\overline{\Omega}_0^2\right]\overline{\rho}_0 - \frac{\overline{S}_1\overline{\rho}_0^\gamma}{\gamma - 1} - 2\overline{x}\overline{F}_0\overline{F}_1 - \frac{|\overline{\nabla}\psi_0|^2}{2}.$$

For the scaled action in Eq. 2.7, the 0-th term is

$$\overline{G}_0 = \int \overline{\mathcal{L}}_0\, d\,\overline{x}\, d\,\overline{z}, \tag{2.13}$$

and the k-th term is given by

$$\overline{G}_k = \int \left(\overline{\mathcal{L}}_k + \overline{x}\,\overline{\mathcal{L}}_{k-1}\right) d\,\overline{x}\, d\,\overline{z}, \quad \text{for} \quad k = 1, 2, 3... \tag{2.14}$$

21

Clearly, successive orders of the Lagrangian density ($\overline{\mathcal{L}}_{k-1}$ and $\overline{\mathcal{L}}_k$) appear in this expression because of the Jacobian's determinant $1 + \epsilon\,\overline{x}$ in Eq. 2.7.

As pointed out earlier, the generalized coordinates themselves have been expanded. To recover the Grad-Shafranov-Bernoulli contributions at each order, it is now necessary to take the variations of equations 2.13-2.14 with respect to the lowest order scaled poloidal flux (ψ_0) and scaled mass density ($\overline{\rho}_0$) [74]. We now proceed to take the variations.

The variation of Eq. 2.13 with respect to the poloidal flux results in

$$\overline{F}_0 = \text{constant,} \tag{2.15}$$

and its variation with respect to the mass density leads to a trivial result. For $k = 1$, the variation of Eq. 2.14 with respect to $\overline{\rho}_0$ leads to a Bernoulli's equation which can be solved for the lowest-order mass density:

$$\overline{\rho}_0(\overline{x}, \overline{z}) = \overline{\rho}_0(\psi_0) = \left(\frac{(\gamma - 1)\overline{H}_0(\psi_0)}{\gamma\overline{S}_0(\psi_0)} \right)^{1/(\gamma - 1)}, \tag{2.16}$$

and the variation with respect to ψ_0 results in a constraint for $\overline{F}_1$:

$$\overline{F}'_1 = \frac{\overline{\rho}_0{}^\gamma \overline{S}'_0 - (\gamma - 1)\overline{\rho}_0 \overline{H}'_0}{(\gamma - 1)\overline{F}_0}. \tag{2.17}$$

These expressions can also be obtained in a straightforward way from the GSB system by a direct calculation. It is when dealing with higher order terms that using the variational principle eases the algebraic manipulation. For $k = 2$, taking the variation of Eq. 2.14 with respect to $\overline{\rho}_0$ leads to:

$$\overline{\rho}_1(\overline{x}, \overline{z}) = \overline{\rho}'_0(\psi_0)\psi_1(\overline{x}, \overline{z}) - \frac{\overline{F}_0^2 \overline{\Phi}_0{}^2 \overline{\rho}_0^{-\gamma}}{2\gamma\overline{S}_0} + \frac{\overline{\rho}_0^{2-\gamma}}{\gamma\overline{S}_0}\left(\overline{H}_1 + \frac{\overline{\Omega}_0^2}{2} \right) - \frac{\overline{\rho}_0 \overline{S}_1}{(\gamma - 1)\overline{S}_0}. \tag{2.18}$$

This signifies that the first-order plasma density is a flux quantity. From the variation with respect to ψ_0 and further algebraic manipulations the outcome is the leading order GS equation:

$$\overline{\nabla}^2\psi_0 + \overline{F}_1\overline{F}_1' + \overline{F}_0\overline{F}_2' + \frac{\overline{F}_0^2\overline{\Phi}_0\overline{\Phi}_0'}{\overline{\rho}_0} - \frac{\overline{\rho}_0\overline{S}_1\overline{H}_0'}{(\gamma-1)\overline{S}_0} + \frac{\gamma\overline{S}_1\overline{\rho}_0^\gamma\overline{S}_0'}{(\gamma-1)^2\overline{S}_0}$$

$$+ \frac{\overline{\rho}_0^{-\gamma}\overline{H}_0'\left[\overline{\rho}_0^2\left(2\overline{H}_1 + \overline{\Omega}_0^2\right) - \overline{F}_0^2\overline{\Phi}_0^2\right]}{2\gamma\overline{S}_0} - \frac{\overline{S}_0'\left[\overline{\rho}_0^2\left(2\overline{H}_1 + \overline{\Omega}_0^2\right) - \overline{F}_0^2\overline{\Phi}_0^2\right]}{2(\gamma-1)\overline{\rho}_0\overline{S}_0} \qquad (2.19)$$

$$- \frac{\overline{\rho}_0^\gamma\overline{S}_1'}{\gamma-1} + \overline{F}_0(\overline{\Omega}_0\overline{\Phi}_0)' + \overline{\rho}_0\left[\overline{H}_1' + \overline{\Omega}_0\overline{\Omega}_0'\right] - 2\overline{x}\overline{F}_0\overline{F}_1' = 0.$$

For an arbitrary choice of the free functions, this PDE is non-linear in the poloidal flux (in general) and is still difficult to solve in an analytic way.

2.5 Choice of the free functions and simplification to a Helmholtz equation

In order to make analytical progress, we look for a simple yet sufficiently flexible set of free functions which transform the GS equation into a linear PDE. By assuming a polynomial dependence of the free functions on the poloidal flux

$$\overline{F}(\psi) = f_0 + \epsilon\left(f_1\psi\right) + \epsilon^2\left(f_2\psi + \frac{1}{2}f_{22}\psi^2\right),$$

$$\overline{S}(\psi) = s_0\psi + \epsilon\left(s_1\psi + \frac{1}{2}s_{11}\psi^2\right),$$

$$\overline{H}(\psi) = h_0\psi + \epsilon\left(h_1\psi + \frac{1}{2}h_{11}\psi^2\right), \qquad (2.20)$$

$$\overline{\Phi}(\psi) = \phi_0\psi,$$

$$\overline{\Omega}(\psi) = \omega_0\psi,$$

Eq. 2.19 turns into a two-dimensional inhomogeneous Helmholtz equation:

$$(\overline{\nabla}^2 + \lambda)\psi = A + C\,\overline{x}, \qquad (2.21)$$

where the constants A, C and λ are given by:

$$A = -f_0 f_2 - \rho_0 h_1 + \frac{s_1 \rho_0^\gamma}{\gamma - 1},$$

$$C = 2 f_0 f_1, \tag{2.22}$$

$$\lambda = f_1^2 + f_0 f_{22} + \frac{(f_0 \phi_0 + \rho_0 \omega_0)^2}{\rho_0} + \rho_0 h_{11} - \frac{s_{11} \rho_0^\gamma}{\gamma - 1}.$$

On the other hand, the leading order mass density in Eq. 2.16 reduces to the constant value

$$\rho_0 = \left[\frac{(\gamma - 1) h_0}{\gamma s_0} \right]^{1/(\gamma-1)}. \tag{2.23}$$

A lowest-order density and the first-order poloidal flux in Eq. 2.18; which can now be simplified to

$$\rho_1(\psi_0) = \frac{\rho_0}{2\gamma C} \left[A + f_0 f_2 + s_1 \rho_0^\gamma \right] + \frac{\psi_0}{2\gamma s_0} \left[\rho_0^{2-\gamma}(h_{11} + \omega_0^2) - \frac{f_0^2 \phi_0^2}{\rho_0^\gamma} + \frac{\gamma s_{11} \rho_0}{1 - \gamma} \right]. \tag{2.24}$$

Several remarks are in order. We have introduced a set of dimensionless constants (the "*free coefficients*"): f_0, f_1, f_2, f_{22}, s_0, s_1, s_{11}, h_0, h_1, h_{11}, ϕ_0 and ω_0 which should be of $\sim O(1)$. In consistency with Eq. 2.15 the leading order term in $\overline{F}$ has been chosen to be constant (f_0); this term controls the vacuum toroidal magnetic field. Its diamagnetic depression (or paramagnetic response in the case, e.g., of a reversed field pinch or possibly an ohmic tokamak) is determined by f_1, f_2 and f_{22}. The pressure profile is controlled by a combination of s_0, s_1, s_{11} and mass density according to the closure Eq. 1.23. From Eq. 2.17 we obtain the leading order term in the diamagnetic depression

$$f_1 = \frac{\rho_0 h_0 (1 - \gamma)}{\gamma f_0} = -\frac{p_o'(\psi_o)}{f_0}, \tag{2.25}$$

where the leading order pressure is a linear function on the poloidal flux

$$p_0(\psi_0) = s_0 \rho_0^\gamma \psi_0 \equiv p_0 \psi_0, \tag{2.26}$$

i.e., in this approximation, isobaric surfaces are flux surfaces to lowest order. Clearly, ϕ_0 and ω_0 are scaling factors for the velocity profile. Ultimately, it is the parameters A, C, and λ which determine the poloidal flux. They will be related to physical quantities for a circular-cross section in the next section. Finally, notice that the inhomogeneous Helmholtz equation has been considered before [75, 76] but for scenarios without background flow. The analytical solutions constructed in this work are more general.

In the following sections, we provide a solution to the inhomogeneous Helmholtz equation under the Dirichlet condition ($\psi_0 = 0$) and over fusion-relevant cross-sections: circular, elliptical and D-shaped. The solutions are constructed by the Green's function method.

2.6 Benchmark against the code FLOW

In this section, we provide a short description of the FLOW code [61], which is used to benchmark the analytic approximations we construct throughout this chapter. FLOW computes numerical solutions for the complete Grad-Shafranov-Bernoulli system without any approximations. Its input is an alternative set of free functions: the quasi-density $D(\Psi)$, quasi-pressure $P(\Psi)$, quasi-sonic poloidal Mach number $M_\theta(\Psi)$, quasi-sonic toroidal Mach number $M_\varphi(\Psi)$ and quasi-toroidal magnetic field $B_o(\Psi)$, which were first introduced in [77]. The relation between the standard and quasi-physical free functions is given by

$$\left(R_o^2 \Omega^2(\Psi) + 2H(\Psi) \right) D^2 - \frac{2\gamma S(\Psi) D^{\gamma+1}}{\gamma - 1} = \Phi^2(\Psi) F^2(\Psi), \tag{2.27}$$

$$P = S(\Psi) D^\gamma, \tag{2.28}$$

$$M_\theta = \frac{\Phi(\Psi) F(\Psi)}{\sqrt{\gamma P D}}, \tag{2.29}$$

$$M_\phi = M_\theta + R_o \Omega(\Psi) \sqrt{\frac{D}{\gamma P}}, \tag{2.30}$$

$$B_o = \frac{F(\Psi)}{R_o}, \tag{2.31}$$

where an MHD closure has been chosen. The alternative set of free functions approaches the corresponding physical variables in the vanishing flow and infinite aspect ratio limit, in this respect, it is more useful for practical applications than the original set of free functions.

For a given self-consistent set of free coefficients and geometrical parameters we can then transform our original free functions profiles given by Eqs. 2.20 to the quasi-physical ones. In the adiabatic case, where $\gamma = 5/3$, Eq. 2.27 defines a fourth order polynomial for D^2, which is trivially solved. The other quasi-physical free functions are obtained in a direct way.

Finally, we define the relative error between the analytical approximation ($\Psi_{analytical}$) and the numerical solution (Ψ_{FLOW}) as

$$\text{E}(\Psi_{FLOW}, \Psi_{analytical}) = \frac{||\Psi_{analytical} - \Psi_{FLOW}||}{||\Psi_{FLOW}||} \times 100\%, \tag{2.32}$$

where $||.||$ stands for the usual 2-norm, that is to say, given a matrix X of dimensions $M \times N$

$$||X|| \equiv \sqrt{\sum_{i,j}^{M,N} (X_{ij})^2}. \tag{2.33}$$

2.7 Circular solution

To deal with a circular cross-section we use the dimensionless polar coordinates $\overline{x} = \overline{r}\cos(\theta)$, $\overline{z} = \overline{r}\sin(\theta)$ centered at the geometrical axis (R_o). In order to guarantee that the lowest order plasma pressure (Eq. 2.26) vanishes at the plasma edge, we choose $\psi_0(1, \theta) = 0$ for $\theta \in [0, 2\pi]$ as our boundary condition. We construct two Green's functions based on an expansion in a complete set of functions for θ and a piecewise function for $\overline{r}$, they correspond to λ being positive or negative and are given in Appendix A. After integrating the sources over the cross-section we obtain a closed-form solution for the poloidal flux of the simple form:

$$\psi_0(\overline{r}, \theta) = \psi_a(\overline{r}) + \psi_b(\overline{r})\cos(\theta), \tag{2.34}$$

The first contribution includes Bessel functions of the first kind

$$\psi_a(\bar{r}) = \frac{J_0\left(\sqrt{\lambda}\right) - J_0\left(\bar{r}\sqrt{\lambda}\right)}{q_* J_1\left(\sqrt{\lambda}\right)\sqrt{\lambda}}, \tag{2.35}$$

while the second term depends on Bessel functions of the first kind and second kind, the regularized hypergeometric function and the Meijer-G-function:

$$\psi_b(\bar{r}) = \frac{2\nu J_1\left(\sqrt{\lambda}\right)\pi}{q_*\,_0\tilde{F}_1\left(;3;-\frac{\lambda}{4}\right)\lambda}\left\{\bar{r}^2 J_2\left(\sqrt{\lambda}\bar{r}\right)Y_1\left(\sqrt{\lambda}\bar{r}\right) - J_1\left(\sqrt{\lambda}\bar{r}\right)\left[\frac{J_2\left(\sqrt{\lambda}\right)Y_1\left(\sqrt{\lambda}\right)}{J_1\left(\sqrt{\lambda}\right)}\right.\right.$$

$$\left.\left. - G_{2,4}^{2,1}\left(\frac{\sqrt{\lambda}}{2},\frac{1}{2}\Big|\begin{matrix}0,-\frac{1}{2}\\0,1,-1,-\frac{1}{2}\end{matrix}\right) + \frac{\sqrt{\lambda}\bar{r}^3}{2}G_{2,4}^{2,1}\left(\frac{\bar{r}\sqrt{\lambda}}{2},\frac{1}{2}\Big|\begin{matrix}-\frac{1}{2},-1\\-\frac{1}{2},\frac{1}{2},-\frac{3}{2},-1\end{matrix}\right)\right]\right\}. \tag{2.36}$$

Details about the Meijer-G-function can be found in [78]. When writing these expressions we have replaced the constants A and C with two new parameters: q_* and ν. For a circularly shaped plasma the kink safety factor is defined as [16, pp. 68-70]:

$$q_* = \frac{aB_\varphi}{R_o B_p} = \frac{2\pi a^2 B_o}{\mu_o R_o I}, \tag{2.37}$$

where I represents the total toroidal current and the other quantities have been defined before. On the other hand, the parameter ν is a combination of the kink safety factor, the inverse aspect ratio and the average value of the plasma beta:

$$\nu \equiv \frac{\beta q_*^2}{\epsilon}. \tag{2.38}$$

In this definition, the average plasma beta is taken over the whole plasma volume (V_p):

$$\beta \equiv \frac{2\mu_o\langle p\rangle}{B_o^2} = \frac{2\mu_o}{B_o^2}\frac{1}{V_p}\int p d^3 r. \tag{2.39}$$

Thus, following Eqs. 2.37-2.39 we can derive

$$A = \frac{\sqrt{\lambda} J_0\left(\sqrt{\lambda}\right)}{q_* J_1\left(\sqrt{\lambda}\right)},$$

(2.40)

and

$$C = \frac{4\nu J_1\left(\sqrt{\lambda}\right)}{q_* \, _0\tilde{F}_1\left(;3;-\frac{\lambda}{4}\right)\sqrt{\lambda}}.$$

(2.41)

Alternatively, we can construct Green's functions which involve an expansion in a complete set of functions in both the θ and $\bar{r}$ directions. After integrating out the inhomogeneity we obtain a series representation for both Eq. 2.35 and Eq. 2.36:

$$\psi_a(\bar{r}) = \sum_{k=1}^{\infty} \frac{2\sqrt{\lambda} J_0\left(\sqrt{\lambda}\right) J_0\left(\bar{r} j_{0,k}\right)}{q_* J_1\left(\sqrt{\lambda}\right) j_{0,k}\left(\lambda - (j_{0,k})^2\right) J_1\left(j_{0,k}\right)},$$

(2.42)

$$\psi_b(\bar{r}) = \sum_{k=1}^{\infty} \frac{32\nu J_1\left(\sqrt{\lambda}\right) J_2\left(j_{1,k}\right) J_1\left(\bar{r} j_{1,k}\right)}{q_*\sqrt{\lambda} \, _0\tilde{F}_1\left(;3;-\frac{\lambda}{4}\right) j_{1,k}\left(\lambda - (j_{1,k})^2\right)\left(J_0\left(j_{1,k}\right) - J_2\left(j_{1,k}\right)\right)^2},$$

(2.43)

where $j_{0,k}$ and $j_{1,k}$ represent the k-th zero of the first and second Bessel function of the first kind, respectively. The series representation 2.43 might be useful if the Meijer-G-function is not defined in the programing language of preference.

It is apparent that the points $\lambda = j_{0,k}^2$ and $\lambda = j_{1,k}^2$ for $k = 1, 2, 3...$ are problematic. In fact, our problem does not have a solution for such cases. The reason is that at least one term in the Fourier-Bessel expansion (needed to deal with the "radial part" of Eq. 2.21 after separation of variables) would vanish, effectively removing a function from either one of the complete sets: $\{J_0\left(j_{0,k}\bar{r}\right)\}$ or $\{J_1\left(j_{1,k}\bar{r}\right)\}$. The first zeros of the Bessel functions are $j_{0,k} = 2.4048, 5.5201, 8.6537$ and $j_{1,k} = 3.8317, 7.0156, 10.1735$. Since these points are far apart from each other, the lack of a solution in those cases does not represent a problem.

Figure 2.1 compares the analytical circular solution against the code FLOW in a typical case. We observe good flux surfaces with an outward Shafranov-Shift, furthermore, the analytical solution satisfies boundary conditions exactly (by construction). There is a relative shift between the analytical and FLOW-generated solution. This is due to the fact that the analytical solution is the lowest-order approximation in terms of the inverse aspect ratio, while the numerical solution corresponds to the exact GSB system.
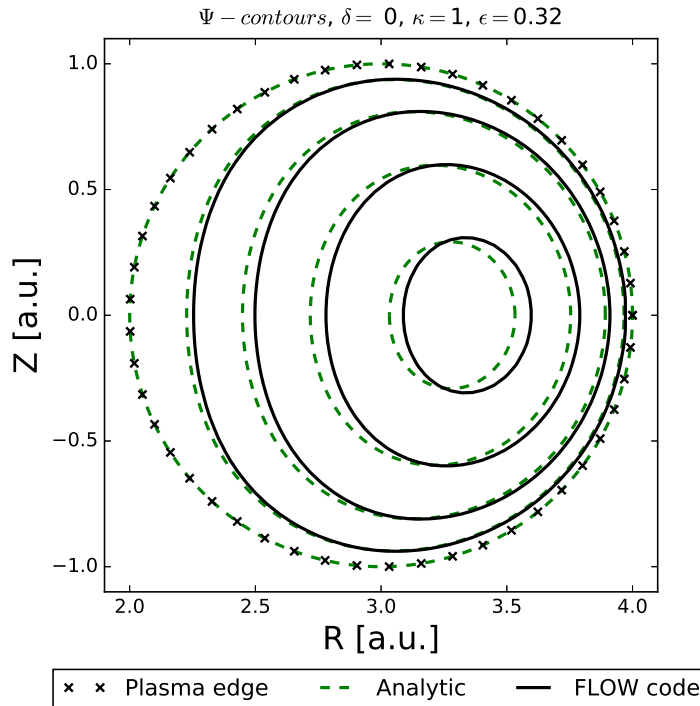
Figure 2.1: Analytic and FLOW-generated magnetic surfaces for a circular configuration with $\epsilon = 0.32$. The analytical poloidal flux vanishes at the plasma edge by construction. The relative shift between the analytic and numerical solution is explained by the fact that the former is a large aspect ratio approximation for the GSB system, while the later solves the exact system. The equilibria correspond to the set of parameters listed as Case II in Table 2.2.

2.7.1 Recovering J. P. Freidberg's static solution as a limiting case and evaluation of some figures of merit

As in Freidberg's high-beta static equilibrium formulation ([16, pp. 154-164]) our solution is expressed in terms of the kink-safety factor ($q* \sim 1$) and the parameter $\nu = \beta q_*^2 / \epsilon$. Even though our stationary (and Freidberg's static) equilibrium solution is formally derived for high-beta scenarios ($\nu \sim 1$), it is possible to explore low-beta configurations ($\nu << 1$) as well. λ

Variable	Case I	Case II	Case III
f_0	1.00	1.00	1.00
f_1	-0.75	-0.75	-0.75
f_2	0.93	0.64	0.44
f_{22}	-0.09	-0.41	-0.41
s_0	4.00	3.00	3.00
s_1	1.00	1.00	1.00
s_{11}	-0.50	-0.50	-0.50
h_0	0.75	4.31	4.31
h_1	1.00	1.00	1.00
h_{11}	1.00	1.00	1.00
ω_0	0.50	0.60	0.60
ϕ_0	0.30	0.30	0.30
A	-1.00	-0.70	-0.50
C	-1.50	-1.50	-1.50
λ	1.50	1.50	1.50
γ	5/3	5/3	5/3
a	1 m	1 m	1 m
R_o	4.5 m	varying	3 m
ϵ	0.22	varying	0.32
κ	1	varying	1.70
δ	0	varying	0.33

Table 2.2: Three sets of parameters defining equilibrium configurations. These parameters define the equilibrium states in the circular, elliptical and D-shaped cross-sections in figures 2.1-2.7.

is a dimensionless parameter which, in its vanishing limit, leads to Freidberg's high-beta static solution [16, Eq. (6.103)] exactly:

$$\lim_{\lambda \to 0} \psi_0(\bar{r}, \theta) = \frac{1}{2q_*} \left[(\bar{r}^2 - 1) + \nu(\bar{r}^3 - \bar{r}) \cos(\theta) \right] . \tag{2.44}$$

As in Solov'ev [24] and other models, the equilibrium current described by our solution undergoes a discontinuous jump to zero at the plasma edge.

It also instructive to notice that the safety factor at the plasma edge for our diffuse equilibrium

$$q_a = \frac{F(\psi)}{2\pi} \oint \frac{dl}{R^2 B_p} = \frac{q_*}{\sqrt{1 - \nu^2}}, \tag{2.45}$$

is the same that Freidberg arrives at with his model [16, Eq. (6.114)], i.e., the equilibrium beta-limit ($\nu < 1$) is independent of the flow strength. Intuitively, this has to be the case, as we

approach the boundary (where $\psi_0 = 0$ by construction), the Helmholtz equation approaches the Poisson's equation Freidberg considers in his formulation, therefore the "plasma-edge" quantities should be the same. As commonly indicated in the literature, the kink safety factor and the safety factor at the plasma edge coincide only for low beta-plasmas.

Another important figure of merit is the magnetic shear. This quantity measures the change of the relative orientation of field lines in neighboring magnetic surfaces. Larger shear is related to better stability properties, in general. In low-beta, large aspect ratio configurations, where the poloidal flux is radially dependent (to leading order) a simple expression for the magnetic shear can be found [16]:

$$s(\overline{r}) \equiv \frac{\overline{r}}{q}\frac{dq}{d\overline{r}}, \tag{2.46}$$

(not to be confused with the entropy free function) where $q(\overline{r})$ is the safety factor defined as

$$q(\overline{r}) \equiv \left(\frac{1}{\overline{r}}\frac{d\psi}{d\overline{r}}\right)^{-1}. \tag{2.47}$$

We can regard the λ parameter as a measure of the magnetic shear. This is more easily seen by considering a low-beta approximation first. In that regime, the average value of the magnetic shear over the cross-section of the plasma (A_p) has a simple form:

$$\langle s \rangle \equiv \frac{1}{A_p}\int s(\overline{r})d^2\overline{r} = 1 - 2\ln\left(J_1\left(\sqrt{\lambda}\right)\right) + 4\int_0^1 \overline{r}\ln\left(J_1\left(\sqrt{\lambda}\overline{r}\right)\right)d\overline{r} + O(\nu). \tag{2.48}$$

This is to be understood as an implicit definition for λ as a function of the magnetic shear:

$$\lambda = \lambda\left(\langle s \rangle\right). \tag{2.49}$$

Figure 2.2a shows a monotonic dependence between $\langle s \rangle$ and λ. Positive (negative) values for the average shear correspond to positive (negative) values for λ. Moreover, as the magnetic shear increases, λ approaches the squared value of a Bessel function's zero ($j_{1,1}^2 = 14.682$) asymptotically. As exemplified in figure 2.2b for a low-beta configuration, the safety factor's concavity goes from downward to upward in accordance with the sign of λ, being flat when λ

vanishes. For high-beta scenarios Eq. 2.48 is not valid anymore. Nevertheless, λ is still a good measure of the magnetic shear in this regime. We motivate why this is so in connection with Shafranov-Shift next.

The Shafranov-Shift (Δ) refers to the displacement of the magnetic axis away from the geometrical center (R_o) in a toroidal configuration. In standard cases, this displacement occurs in the outward direction as a mechanism to provide toroidal force balance by the compression of the poloidal magnetic field against the conducting wall of the confinement vessel. For a $\lambda = 0$ scenario the Shafranov-Shift is given by

$$\Delta/a = \frac{\sqrt{3\nu^2 + 1} - 1}{3\nu}, \tag{2.50}$$

This is illustrated in figure 2.2c. As expected, a similar dependence on ν is seen when $\lambda \neq 0$.

Starting from the shearless scenario in a low-beta configuration ($\lambda = 0$), consider an infinitesimal (quasi-static) increase $+d\lambda$. As previously argued, in a low-beta regime λ is a good measure of the magnetic shear, therefore, this infinitesimal change is accompanied with a magnetic shear variation ($+d\langle s \rangle$) which, in turn leads to an extra accumulation of poloidal magnetic field in the outer region; as a result, a smaller Shafranov-Shift is needed to restore toroidal force balance and the other way around for an infinitesimal decrease ($-d\lambda$). This explains the relative position of the three curves in the low-beta region of figure 2.2c. In the same way, an infinitesimal magnetic shear variation ($\pm d\langle s \rangle$) in a high-beta configuration induces a change in the Shafranov-Shift: inward if there is an extra poloidal magnetic field in the outward region and vice versa. Finally, the relative position of the three curves in figure 2.2c stays the same all the way up to the high-beta region, therefore, we can extend our identification of λ as a reasonable measure for the magnetic shear to high-beta configurations as well.

To sum up, the poloidal flux is specified by the kink safety factor (q_*), the plasma-beta regime (ν) and a measure for the average magnetic shear (λ).
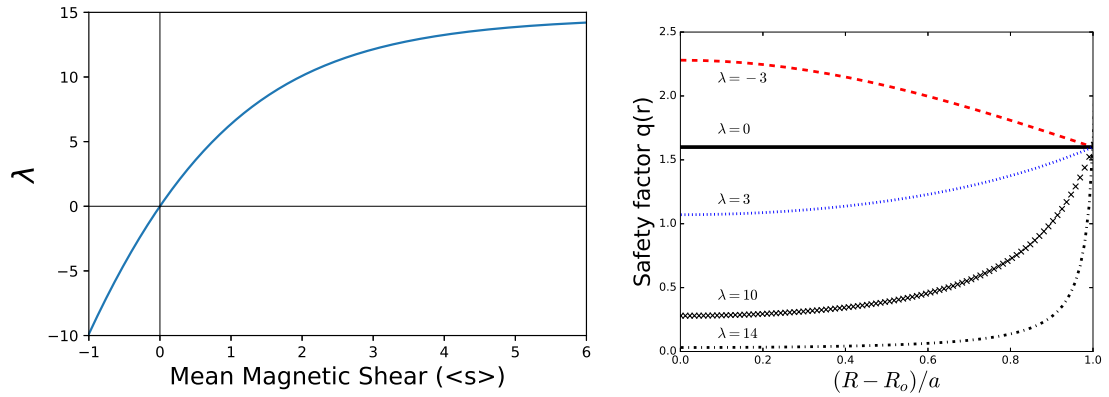
(a) λ parameter as a function of the average magnetic shear in a low-beta approximation.

(b) Safety factor profiles in a zero-beta scenario.
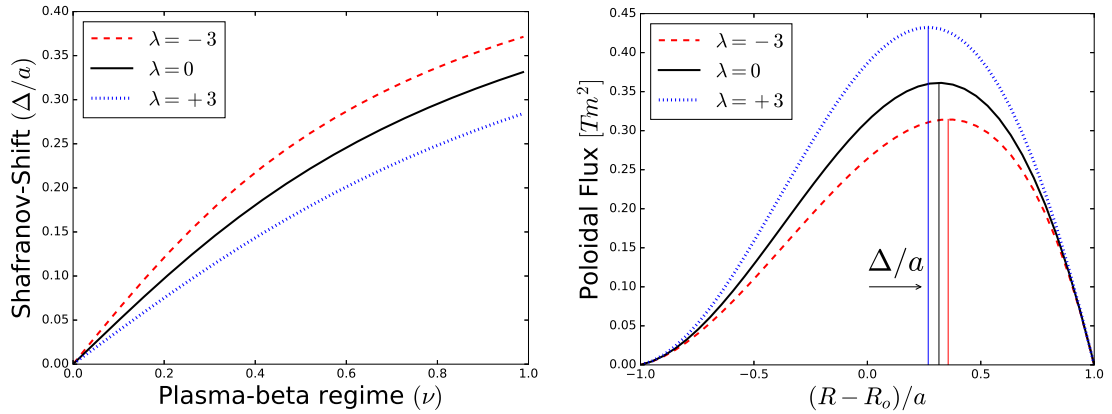
(c) Shafranov-Shift increases with plasma-beta and decreases with magnetic shear (λ).

(d) Shafranov-Shift (Δ) induced by a changing magnetic shear (λ) in a high-beta ($\nu = 0.9$) scenario.

Figure 2.2: Shafranov-Shift (Δ) and average magnetic shear ($\langle s \rangle$). a) Monotonic increase of λ with the average magnetic shear ($\langle s \rangle$). b) Typical profiles for the safety factor for several values of λ. c) Shafranov-Shift induced by a changing plasma pressure and magnetic shear. d) High-beta illustration for the Shafranov-Shift at different λ values.

2.8 Elliptical Solution

The solution's construction for an elliptical cross-section is similar to the circular one. We build appropriate Green's functions and carry out the source term integration. However, the resulting integrals are difficult to evaluate in a closed-form and the end result is a series-form solution.

We consider a vertical ellipse with semi-minor axis 1 and semi-major axis $\kappa > 1$ (the elongation). The semi-focal distance is given by

$$\overline{f} \equiv \kappa\sqrt{1 - \kappa^{-2}}. \tag{2.51}$$

Points inside the ellipse are specified in terms of the elliptical coordinates (ζ, η), which behave as a radial and an angular coordinate, respectively. The transformation to the chamber-centered dimensionless Cartesian coordinate system is

$$\overline{x} = \overline{f}\sinh(\zeta)\sin(\eta), \tag{2.52}$$

$$\overline{z} = \overline{f}\cosh(\zeta)\cos(\eta), \tag{2.53}$$

where $\eta \in [0, 2\pi]$ and $0 \leq \zeta \leq \zeta_o$. The boundary of the ellipse occurs at the value $\zeta = \zeta_o$ which is given in terms of the elongation by

$$\zeta_o = \operatorname{arctanh}(\kappa^{-1}). \tag{2.54}$$

Therefore, in elliptical coordinates, the homogeneous Dirichlet boundary condition is expressed as $\psi_0(\zeta_o, \eta) = 0$ for $\eta \in [0, 2\pi]$.

From the standard separation of variables

$$\psi_0(\zeta, \eta) = \Upsilon(\zeta)\chi(\eta), \tag{2.55}$$

the Helmholtz equation leads to the angular and radial Mathieu differential equations:

$$\frac{d^2\chi}{d\eta^2} + (c - 2\Lambda\cos(2\eta))\,\chi = 0, \quad \chi(\eta) = \chi(\eta + 2\pi), \tag{2.56}$$

$$\frac{d^2\Upsilon}{d\zeta^2} - (c - 2\Lambda\cosh(2\zeta))\,\Upsilon = 0, \qquad \Upsilon(\zeta_o) = 0, \tag{2.57}$$

where c is a separation constant and $\Lambda \equiv \overline{f}^2\lambda/4$ contains information about the chamber elongation (through $\overline{f}$) and magnetic shear (through λ). The solution of Eq. 2.57 is required to be regular at the origin. Mathieu functions are well studied [79, 78, 80, 81] and have been employed in static equilibrium solutions for axisymmetric scenarios before [75, 82].

Solutions of the angular Mathieu functions can be thought of as the generalization of the *sine* and *cosine* trigonometric functions. They are known as the *cosine-elliptic* and *sine-elliptic* functions. The periodicity condition $\chi_m(\eta) = \chi_m(\eta + 2\pi)$ restricts the allowed values of the separation constant to a discrete set $c = c_m$. These values are discriminated into two classes; denoted by $a_m(\Lambda)$ and $b_m(\Lambda)$, the first class corresponds to the values of the separation constant associated with the cosine-elliptic function, while the second class corresponds to the sine-elliptic function. In a similar way, the radial Mathieu functions are the generalization of the Bessel function of the first or second kind: J_m, N_m, I_m and K_m [81]. For the same characteristic values c_m, the radial Mathieu ODE has two pairs of linearly independent solutions, which are oscillatory (for $\Lambda > 0$) or evanescent (for $\Lambda < 0$). Table 2.3 summarizes the solutions of the angular and radial Mathieu functions.

Parity	Even	Odd
Eigenvalue	$a_m(\Lambda)$	$b_m(\Lambda)$
Angular	$\mathrm{ce}_m\,(\eta,\Lambda)$	$\mathrm{se}_m\,(\eta,\Lambda)$
Radial	$\mathrm{Je}_m\,(\zeta,\Lambda)$	$\mathrm{Jo}_m\,(\zeta,\Lambda)$
$\Lambda > 0$	$\mathrm{Ne}_m\,(\zeta,\Lambda)$	$\mathrm{No}_m\,(\zeta,\Lambda)$
Radial	$\mathrm{Ie}_m\,(\zeta,\Lambda)$	$\mathrm{Io}_m\,(\zeta,\Lambda)$
$\Lambda < 0$	$\mathrm{Ke}_m\,(\zeta,\Lambda)$	$\mathrm{Ko}_m\,(\zeta,\Lambda)$

Table 2.3: The angular and radial Mathieu functions can be interpreted as the generalizations of the harmonic and Bessel functions.

In analogy to the procedure to tackle the circular case, we construct Green's function which involves an expansion for η in angular Mathieu functions and a piecewise function for ζ in terms of the radial Mathieu functions. (see in Appendix A). After integrating the source term we obtain a series solution of the form

$$\overset{\text{elliptical}}{\psi_0(\zeta, \eta)} = \sum_{m=0}^{\infty} [A_{2m}(\zeta, \Lambda)\text{ce}_{2m}(\eta, \Lambda) + C_{2m+1}(\zeta, \Lambda)\text{se}_{2m+1}(\eta, \Lambda)]. \qquad (2.58)$$

The functions $A_m(\zeta, \Lambda)$ and $C_m(\zeta, \Lambda)$ are integrals in the radial-like direction that have to be evaluated numerically. For $\Lambda > 0$ these are

$$A_m(\zeta, \Lambda) \equiv \frac{A\overline{f}^2\pi}{4\text{Je}_m(\zeta_o, \Lambda)} \int_0^{\zeta_o} \text{Je}_m(\zeta_<, \Lambda)\text{JNe}_m(\zeta_>, \Lambda)\text{KA}_m(\zeta', \Lambda)d\zeta', \qquad (2.59)$$

$$C_m(\zeta, \Lambda) \equiv \frac{C\overline{f}^3\pi}{4\text{Jo}_m(\zeta_o, \Lambda)} \int_0^{\zeta_o} \text{Jo}_m(\zeta_<, \Lambda)\text{JNo}_m(\zeta_>, \Lambda)\text{KC}_m(\zeta', \Lambda)d\zeta', \qquad (2.60)$$

The integration is carried out trough the variable ζ'. $(\zeta_<, \zeta_>)$ refer to the minimum or maximum between the point of observation ζ and the integration variable ζ', i.e., for a given point of interest ζ, the value of $\zeta_<$ will be equal to the integration variable if $\zeta' < \zeta$ and equal to the point of interest if $\zeta < \zeta'$, and the opposite for $\zeta_>$. Additionally, we have defined JNe_m and JNo_m as an antisymmetric combination of the corresponding radial Mathieu functions (Je_m, Ne_m, Jo_m, No_m). This is a standard combination that appears when constructing a Green's function using a piecewise function for the radial direction. The combination arises in order to satisfy the boundary condition $\Upsilon(\zeta_o) = 0$. Furthermore, the integrals 2.58 and 2.59 involve extra functions: $\text{KA}_m(\zeta, \Lambda)$ and $\text{KC}_m(\zeta, \Lambda)$. They are given by

$$\text{KA}_m(\zeta, \Lambda) \equiv 2D_0^m(\Lambda)\cosh(2\zeta) - D_2^m(\Lambda), \qquad (2.61)$$

$$\text{KC}_m(\zeta, \Lambda) \equiv \left[B_1^m(\Lambda) \left[\frac{1}{2} + \cosh(2\zeta) \right] - \frac{1}{2}B_3^m(\Lambda) \right] \sinh(\zeta). \qquad (2.62)$$

36

$D_0^m(\Lambda)$, $D_2^m(\Lambda)$, $B_1^m(\Lambda)$ and $B_3^m(\Lambda)$ are Fourier components of the angular Mathieu functions (see Appendix B). Similar expressions could be constructed for the $\Lambda < 0$ case employing the evanescent radial Mathieu functions instead.

An equilibrium configuration under realistic values of elongation ($\kappa = 1.7$) and inverse aspect ratio ($\epsilon = 0.32$) is shown in Fig. 2.3. As in the circular case, the analytic solution satisfies the vanishing poloidal flux condition at the plasma edge by construction. In the test cases shown here, the analytic approximations underestimate the Shafranov-Shift.
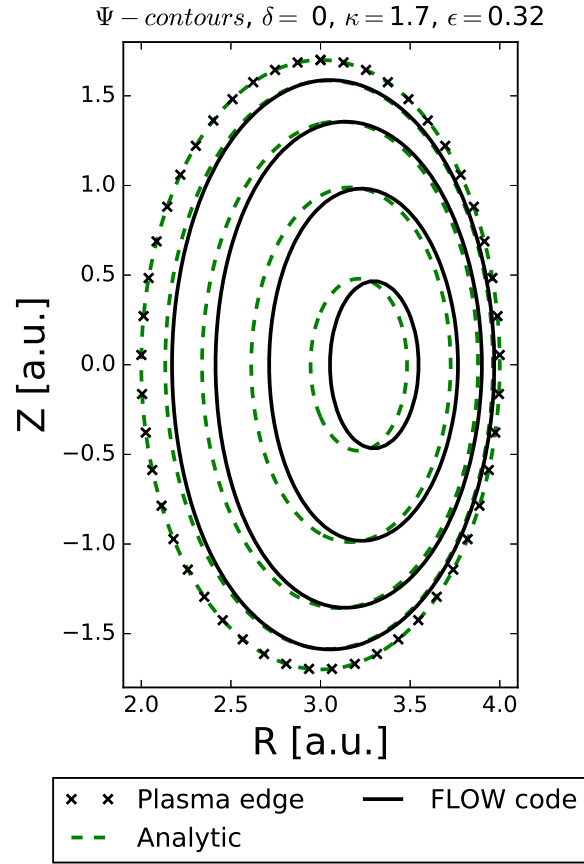
Figure 2.3: Analytic and FLOW-generated magnetic surfaces for an elliptical ($\kappa = 1.7$) configuration with $\epsilon = 0.32$. The analytic poloidal flux vanishes at the plasma edge by construction. The relative shift between the analytic and numerical solution is explained by the fact that the former is a large aspect ratio approximation for the GSB system, while the latter solves the exact system. The equilibria correspond to the set of parameters listed as Case II in Table 2.2.

Figures 2.4 and 2.5 illustrate midplane profiles of several quantities of interest (magnetic field, pressure, number density and velocity fields) for a standard configuration. In particular, observe the correct shaping of the density profile in figure 2.4d. In accordance with Eq. 2.24, this shaping can be calculated without solving for the first-order poloidal flux (ψ_1). This feature

results from our ordering and free function choosing. We have assumed a deuterium plasma with ion mass $m_d = 3.34 \times 10^{-27} kg$. Figure 2.5a shows a maximum plasma-beta of the order $\beta_{\varphi\ max} \sim O(\epsilon)$, which corresponds to a high-beta configuration. Figures 2.5c-2.5d show toroidal and poloidal velocities in the range they are present in experiments.

(a) Toroidal magnetic field

(b) Poloidal magnetic field

(c) Pressure

(d) Number density
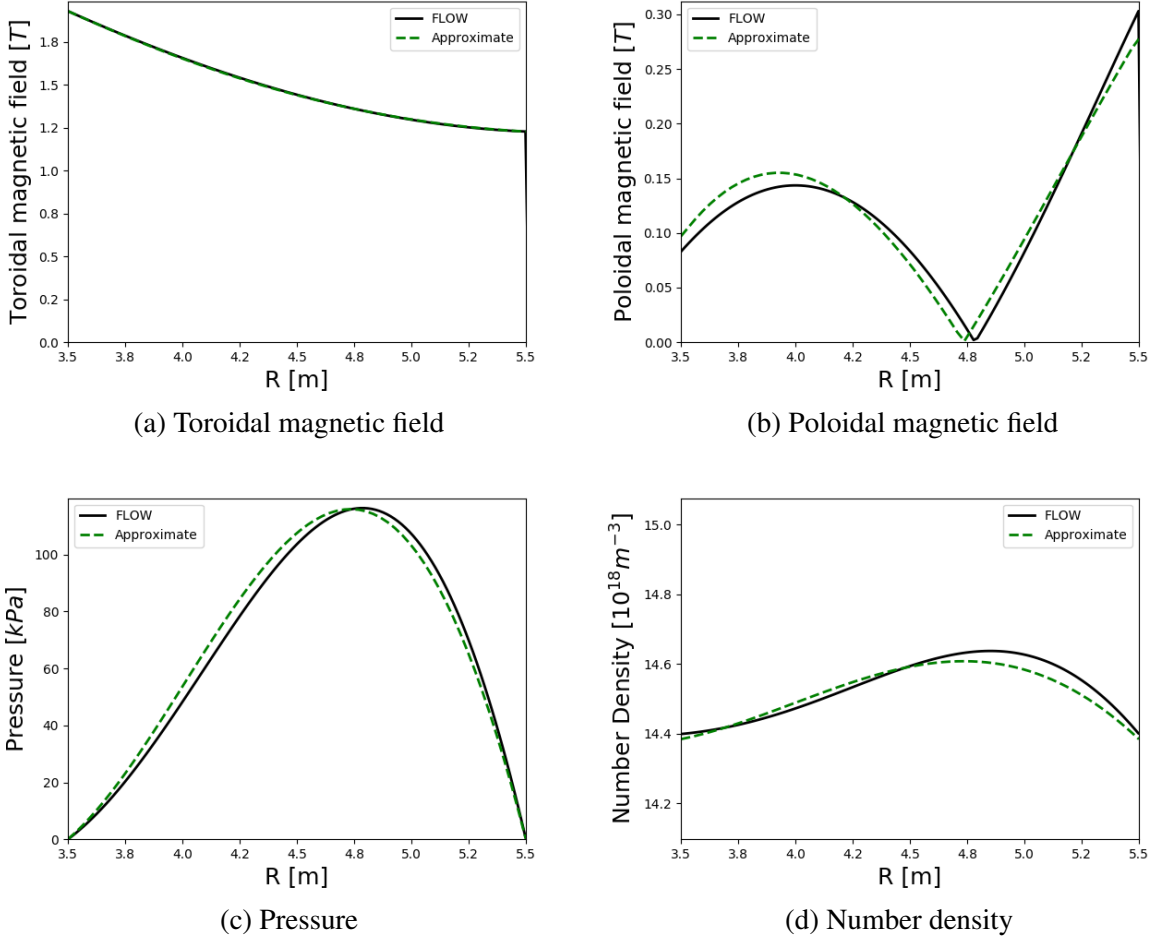
Figure 2.4: Typical midplane equilibrium quantities for a circularly shaped plasma of a small inverse aspect ratio ($\epsilon = 0.22$) determined analytically and with the code FLOW. (a) toroidal magnetic field, (b) poloidal magnetic field, (c) kinetic pressure and (d) number density. The profiles correspond to the equilibrium parameters listed as Case I in Table 2.2.

All the analytic approximations we have constructed correspond to the lowest-order part in a power series expansion in terms of the inverse aspect ratio. On the other hand, numerical solutions can be regarded as exact since FLOW solves the GSB with only numerical approximations. It follows that the relative error between the two should be linear in the expansion parameter. This trend is confirmed in Fig. 2.6 for the circular and elliptical cases.

The elliptical solution we have constructed is given in a series-form (Eq. 2.58). As exemplified in figures 2.6a, 2.6b and 2.6c for scenarios with realistic elongations ($\kappa = 1.3 - 2$), convergence is reached by considering a "small" number of terms in the series. Furthermore, by progressively reducing the elongation (the number of terms in the series-form solution being fixed) the relative error diminishes, reaching a minimum value for the circular configuration (which is computed by the closed-form solution in Eqs. 2.35-2.36). This is illustrated in figure 2.6d.

(a) Beta toroidal

(b) Poloidal magnetic flux

(c) Toroidal velocity

(d) Poloidal velocity
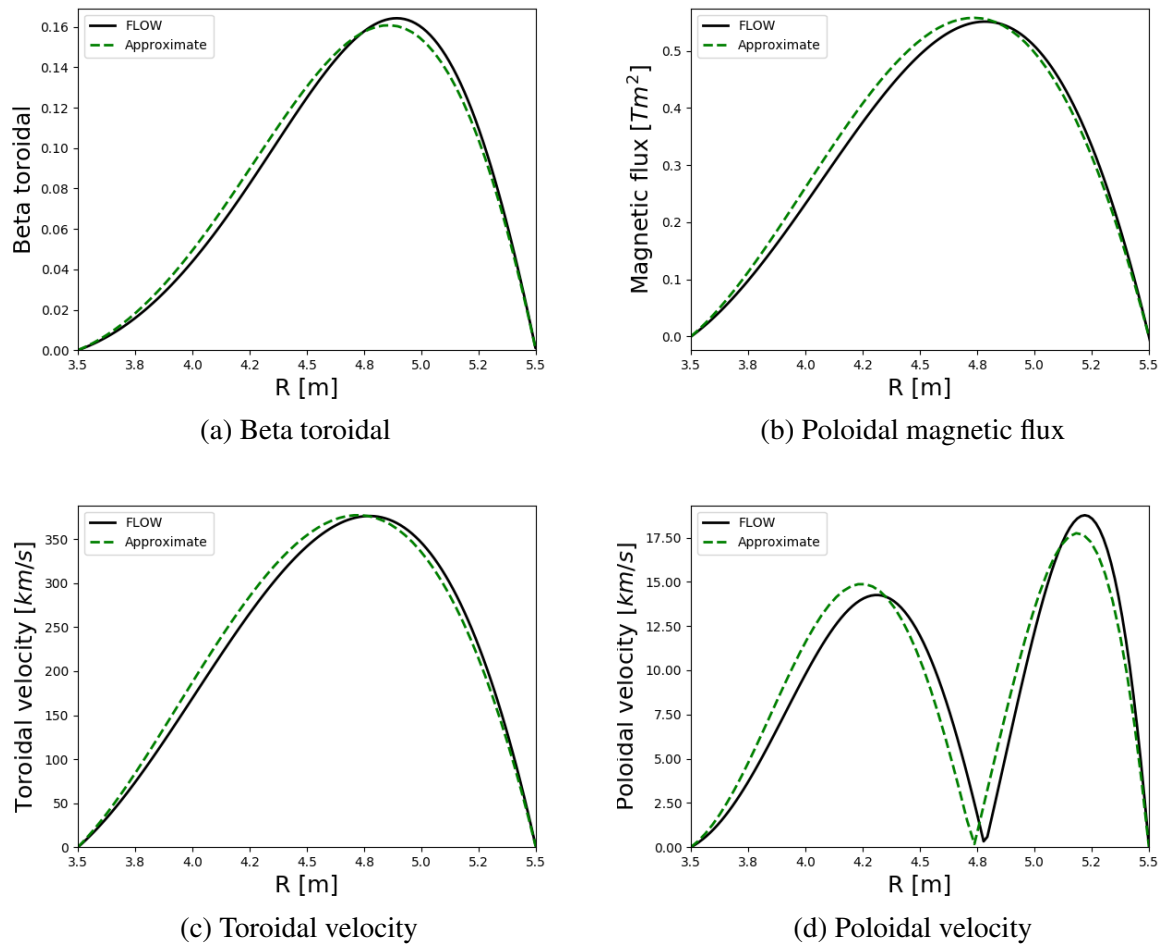
Figure 2.5: Typical midplane equilibrium quantities for a circularly shaped plasma of a small inverse aspect ratio ($\epsilon = 0.22$) determined analytically and with the code FLOW. (a) beta toroidal, (b) poloidal magnetic flux, (c) toroidal velocity and (d) poloidal velocity. The profiles correspond to the equilibrium parameters listed as Case I in Table 2.2.
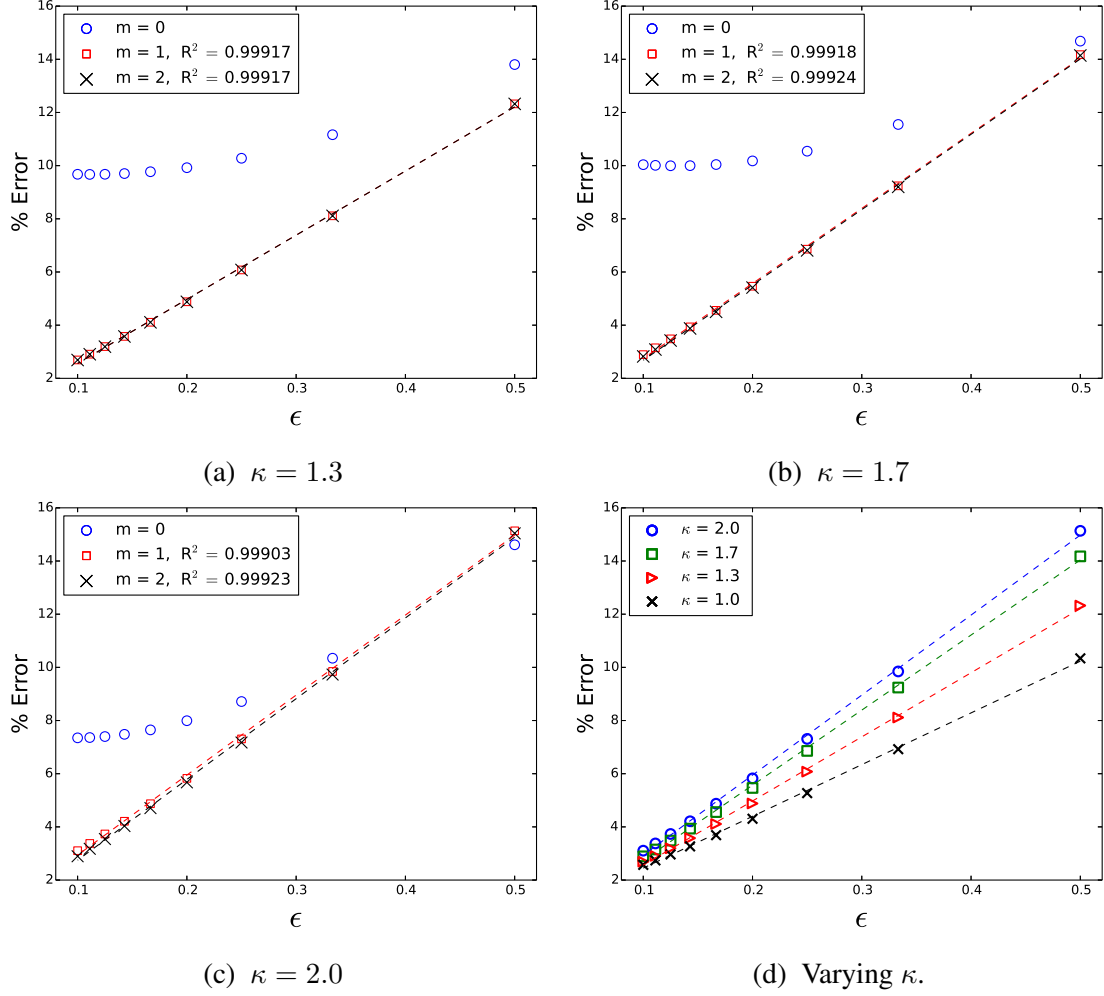
Figure 2.6: Relative error between the analytical and FLOW-generated poloidal flux as a function of the inverse aspect ratio for elliptically and circularly shaped configurations. R^2 stands here for the coefficient of determination. For the fixed set of parameters corresponding to Case II in Table 2.2, figures (a), (b) and (c) illustrate the error for a varying number of terms in the series-form elliptical solution (Eq. 2.58). The number of considered terms is equal to $2m + 2$, where m is an integer assuming the indicated values. Fig. (d) shows an error comparison for a varying elongation (with $m = 2$ fixed) having as the lower-bound the error associated with the circular solution ($\kappa = 1$).

2.9   D-shape solution

The main difficulty when dealing with a tokamak having a D-shaped cross-section is geometrical. For this problem, we employ another solution strategy. The underlying idea is to successively approximate the D-shape solution with correction terms which are computed by solving PDE's *over an ellipse* and, in this way, trading the D-shape geometrical difficulties to solve an infinite sequence of simpler problems. Furthermore, we will be able to reutilize the

Green's functions in elliptical coordinates constructed in the last section, making the approach even more economical in terms of extra calculations.

2.9.1 D-shape reparametrization

A D-shape boundary parametrization has been given in Eq. 1.3. A dimensionless representation in chamber-centered coordinates is

$$\overline{x} = \cos(\tau + \alpha \sin(\tau)), \tag{2.63}$$

$$\overline{z} = \kappa \sin(\tau), \tag{2.64}$$

where the triangularity (δ) has been defined before in terms of the α parameter. Convex boundaries satisfy $\alpha \leq 1$. Negative triangularity scenarios are also a possibility. For the cases we will be interested in we will assume $|\delta| << 1$, and from Eq. 1.4 it follows that $\delta \sim \alpha$. It is also clear that if $\alpha = 0$ the parametrization traces the vertical ellipse of semi-minor axis 1 and semi-mayor axis $\kappa > 1$ we dealt with in section 2.8.

In order to exploit the "elliptical Green's functions" later on we introduce an alternative parametrization:

$$\overline{x} = \overline{f} \sinh(\zeta_0) \sin \left(\eta - \alpha \cos(\eta) \right), \tag{2.65}$$

$$\overline{z} = \overline{f} \cosh(\zeta_o) \cos(\eta), \tag{2.66}$$

where ζ_o has been defined in Eq. 2.54 and the semi-focal distance ($\overline{f}$) is given by 2.51. Clearly, $\eta \in [0, 2\pi]$ is an elliptic-like angular coordinate. From the change of variables $\tau = \eta - \pi/2$ it follows that, up to direction of parametrization Eqs. 2.63-2.64 are equivalent to Eqs. 2.65-2.66.

2.9.2 D-shape solution from a boundary perturbation technique

A comparison of the $\overline{x}$ coordinate parametrization for the elliptical boundary (Eq. 2.52) against its parametrization for the D-shape boundary (Eq. 2.65) suggests that we expand the latter in

terms of the triangularity:

$$\overline{x} = \overline{f} \sinh(\zeta_0) \left[\sin(\eta) - \alpha \cos^2(\eta) - \frac{\alpha^2}{2} \cos^2(\eta) \sin(\eta) + ... \right]. \qquad (2.67)$$

The first term in this expansion corresponds to Eq. 2.52 and the remaining ones can be thought of as deviations away from the elliptical boundary. The overall perturbation is denoted by

$$\overline{\delta x} \equiv \alpha \, \overline{\delta x}_1 + \alpha^2 \, \overline{\delta x}_2 + ... \, , \qquad (2.68)$$

where

$$\begin{aligned}
\overline{\delta x}_1 &= -\overline{f} \sinh(\zeta_0) \cos^2(\eta), \\
\overline{\delta x}_2 &= -\overline{f} \sinh(\zeta_0) \cos^2(\eta) \sin(\eta)/2,
\end{aligned} \qquad (2.69)$$

and so on. We denote by ∂D and ∂E the exact D-shaped and elliptical boundaries, respectively. Let us now recall that the problem we need to solve is given by the leading GS equation (Eq. 2.21), which we rewrite here for convenience:

$$(\overline{\nabla}^2 + \lambda)\psi_0 = A + C \, \overline{x}, \qquad \psi_0|_{\partial D} = 0. \qquad (2.70)$$

We recall also that ψ_0 denotes the lowest-order poloidal flux in the inverse aspect ratio expansion. To transfer the boundary conditions from ∂D to ∂E in Eq. 2.70 we make use of the Taylor expansion

$$\psi_0|_{\partial D} = \psi_0|_{\partial E} + \left. \frac{\partial \psi_0}{\partial \overline{x}} \right|_{\partial E} \overline{\delta x} + \frac{1}{2} \left. \frac{\partial^2 \psi_0}{\partial \overline{x}^2} \right|_{\partial E} \overline{\delta x}^2 + ... \, , \qquad (2.71)$$

It should be stressed that, while the LHS is evaluated at ∂D, the RHS is evaluated at ∂E. Moving on, we now propose a power series expansion for the lowest-order poloidal flux in terms of the triangularity:

$$\psi_0 = \psi_0^{(0)} + \alpha \, \psi_0^{(1)} + ... \qquad (2.72)$$

and we substitute it back in the equilibrium problem: both in the partial differential equation (Eq. 2.70) and in the boundary condition, as given by the Taylor expansion 2.71. In this way, we end up with a collection of problems corresponding to progressively higher $O(\alpha^k)$ corrections, each one of them with boundary conditions at ∂E.

The $O(\alpha^0)$ problem:

$$(\overline{\nabla}^2 + \lambda)\psi_0^{(0)} = A + C\,\overline{x}, \quad \psi_0^{(0)}\big|_{\partial E} = 0, \tag{2.73}$$

has already been solved in the previous section. Its solution is given by Eq. 2.58. Higher order corrections obey a homogeneous PDE, with an inhomogeneous Dirichlet boundary condition dependent upon lower order corrections

$$(\overline{\nabla}^2 + \lambda)\psi_0^{(i)} = 0, \quad \psi_0^{(i)}\big|_{\partial E} \neq 0, \quad \text{B.C. depends on } \psi_0^{(i-1)}, \psi_0^{(i-2)}, \dots \psi_0^{(0)}. \tag{2.74}$$

In particular, the order $O(\alpha)$ boundary condition is

$$\psi_0^{(1)}\big|_{\partial E} = -\overline{\delta x_1}\,\frac{\partial\psi_0^{(0)}}{\partial\overline{x}}\bigg|_{\partial E}, \tag{2.75}$$

and the $O(\alpha^2)$ boundary condition is

$$\psi_0^{(2)}\big|_{\partial E} = -\overline{\delta x_1}\,\frac{\partial\psi_0^{(1)}}{\partial\overline{x}}\bigg|_{\partial E} - \overline{\delta x_2}\,\frac{\partial\psi_0^{(0)}}{\partial\overline{x}}\bigg|_{\partial E} - \frac{\overline{\delta x_1}^2}{2}\,\frac{\partial^2\psi_0^{(0)}}{\partial\overline{x}^2}\bigg|_{\partial E}. \tag{2.76}$$

The generic solution to the i-th problem in Eq. 2.74 is found by employing the Green's functions for an elliptic cross-section we constructed in section 2.8. The solution is given by a contour integral of the boundary condition over ∂E and it can be expressed as a superposition of the radial and angular Mathieu functions:

$$\overset{\text{D-shape}}{\psi_0^{(i)}(\zeta, \eta)} = \sum_{n=0}^{\infty} C_n^{(i)}\mathrm{Je}_n(\zeta, \Lambda)\mathrm{ce}_n(\eta, \Lambda) + \sum_{n=1}^{\infty} A_n^{(i)}\mathrm{Jo}_n(\zeta, \Lambda)\mathrm{se}_n(\eta, \Lambda). \tag{2.77}$$

43

Eq. 2.77 has been written in terms of oscillatory radial Mathieu functions by assuming a $\Lambda >$ 0 scenario. For $\Lambda < 0$ it is necessary to employ the evanescent radial Mathieu functions instead. The first and second-order α-corrections are provided in Appendix C but higher-order corrections can be constructed using the Green's function given in Appendix A.

Figure 2.7 exemplifies D-shaped configurations for realistic, ITER-like parameters in elongation ($\kappa = 1.7$), inverse aspect ratio ($\epsilon = 0.32$) and triangularity ($\delta = 0.23, 0.32$). The illustrations consider the 1-st and 2-nd order corrections in terms of the triangularity, as well as FLOW-generated numerical solutions for comparison. In particular, contrary to the elliptical case, the curve defined by the condition $\Psi_{analytic} = 0$ matches the plasma edge only if enough correction terms have been added. In this respect, figure 2.7b shows that the $O(\alpha)$ order correction "goes beyond" the plasma edge, but the $O(\alpha^2)$ "pulls the solution back", closer to the correct boundary. Figures 2.7b and 2.7c illustrate more extreme cases for larger values of the triangularity. In the first case, the curve defined by $\Psi_{analytic} = 0$ is not even closed to first approximation, but with the second order correction, the solution "recovers" and approaches the correct boundary; in the second figure, both the $O(\alpha)$ and $O(\alpha^2)$ curves are open near the boundary. This behavior is not surprising: since the D-shape solution was built by transferring the boundary conditions from ∂D to ∂E, it calls to reason that a higher order correction is needed as the triangularity increases.

Finally, figure 2.8 provides the relative error between FLOW-generated solution and the analytical approximation for different values of the triangularity. Here, we illustrate the $O(\alpha^0)$, $O(\alpha)$ and $O(\alpha^2)$ solutions; it is evident that higher order approximations perform better. As in the circular and elliptical cases, a linear trend between the relative error and the inverse aspect ratio is observed.

2.10   Summary of results

In this chapter, we have constructed high-beta analytic approximations for axisymmetric equilibria with diffuse toroidal and poloidal velocity profiles. The solutions correspond to the lowest-order part in an inverse aspect ratio approximation of the Grad-Shafranov-Bernoulli

(a)   (b)

(c)
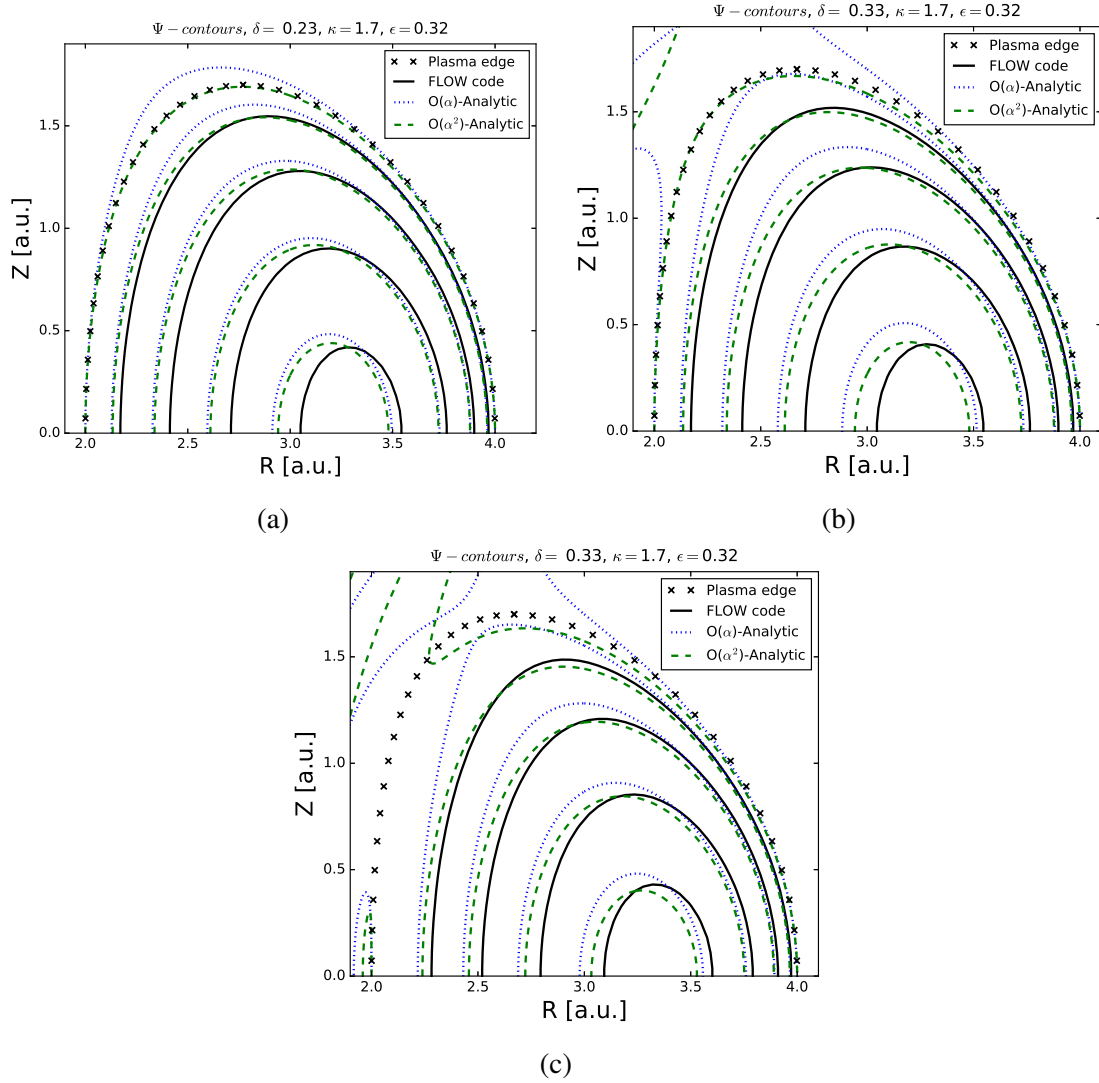
Figure 2.7: Magnetic surfaces in D-shaped configurations for realistic values of elongation ($\kappa = 1.7$), inverse aspect ratio ($\epsilon = 0.32$) and triangularities ($\delta = 0.23$ and $\delta = 0.33$). Since the plasma is of up-down symmetric only the upper half section is shown. Figures (a) and (b) differ from its triangularity value but otherwise correspond to Case II from Table 2.2 while Fig. (c) corresponds to Case III from the same table. The plasma edge is determined by the parametrization in Eqs. 2.65-2.66. The figure show the 1-st and 2-nd order analytical approximations in terms of the triangularity, as well as the FLOW-generated numerical solution.
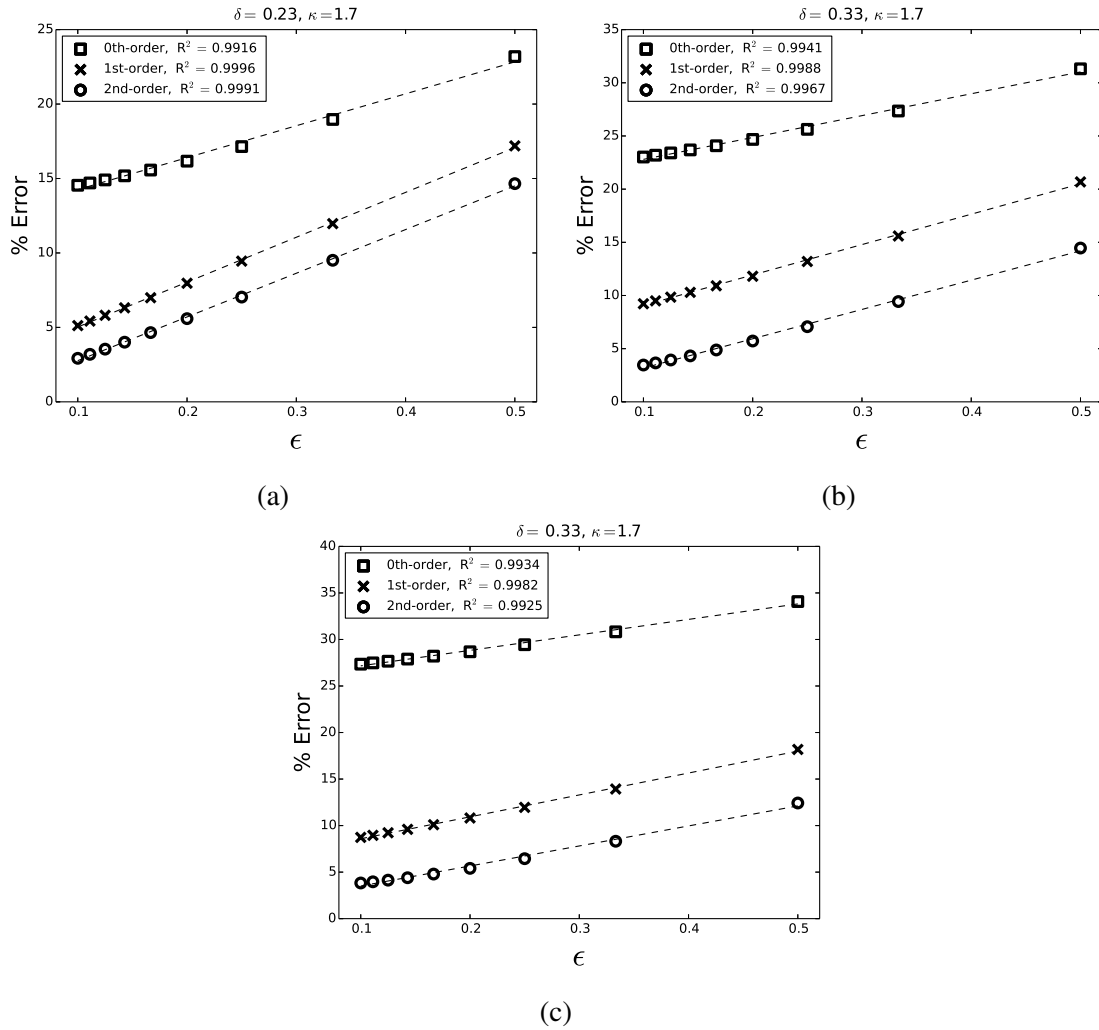
Figure 2.8: Relative error between the analytical and FLOW-generated poloidal flux as a function of the inverse aspect ratio for D-shaped configurations with realistic values of elongation $\kappa = 1.7$ and triangularity ($\delta = 0.23, 0.33$). We show the $O(\alpha^0)$, $O(\alpha)$ and $O(\alpha^2)$ approximations. R^2 stands here for the coefficient of determination. Figures (a) and (b) correspond to the set of parameters referred to as Case II in Table 2.2 while (c) to case III.

system, and under a polynomial dependence of the free functions on the poloidal flux. Moreover, the analytic solutions are flexible in terms of the cross-section over which they are defined, being possible to describe circular, elliptical and D-shaped configurations.

Circular and elliptical equilibria are constructed by the Green's function method. The result is a closed-form solution for the circular case, which is determined by Bessel functions and the Meijer-G-function. It is controlled by three parameters whose physical interpretation is straightforward: the kink safety factor, the plasma beta, and the magnetic shear. For plasmas with an elliptical cross-section of arbitrary elongation, we have obtained a series-form solution in terms of Mathieu functions. By construction, both solutions satisfy $\Psi_{analytic} = 0$ at the plasma edge.

To deal with the D-shaped cross-section we have applied a boundary perturbation method which effectively transfers the Dirichlet condition to the elliptical boundary. The method requires an extra power series expansion, this time in terms of the triangularity. In contrast with the circular and elliptical solutions, the vanishing of the poloidal flux on the boundary is only approximately satisfied over the D-shaped boundary. However, higher order approximations in terms of the triangularity result in increased performance, and we have been able to reutilize the Green's functions constructed for the elliptical case to obtain such approximations.

The relative error between the FLOW-generated numerical solutions and the analytical approximations has been shown to linearly decrease as the inverse aspect ratio diminishes. As exemplified in several test cases (whose specific parameters are given for completeness), the analytical solutions can deal with experiment-relevant values of elongation, inverse aspect ratio, and triangularity.

Chapter 3

Low-n external ballooning-kink modes in the presence of resistive walls and a diffuse toroidal
flow profile

3.1 Introduction

In the present chapter, we carry out a linear stability analysis for the high-beta, stationary, dif-
fuse circular equilibrium model. Our aim is to investigate the behavior of external ballooning-
kink modes under a diffuse toroidal rotation profile. The analysis consists of two parts: in
the first part, the plasma column dynamics is expressed as a set of independent ordinary dif-
ferential equations (eigenmode equations) for the different poloidal harmonics of the plasma
displacement; in the second part, these harmonics are coupled together at the plasma-vacuum
interface and, additionally, ideal or resistive-wall effects are incorporated. The analysis is built
upon Betti's sharp-boundary, rigid-toroidal-rotation formalism for the study of these instabili-
ties [60]. In Betti's formalism, the eigenmode equation is solved analytically in a perturbative
way and, ultimately, a set of coupled algebraic equations is cast as a matrix whose determinant
leads to the system's dispersion relation, which can then be efficiently studied by root-finding
methods. This analysis is possible, in part, due to the simplicity of the inner plasma region,
as described by the sharp-boundary model with solid toroidal rotation. In contrast, the eigen-
mode equation obtained for our diffuse model is not analytically tractable, as a consequence, a
different scheme was implemented. We rely on a multidimensional shooting method as the so-
lution technique. For a given set of equilibrium parameters, the implemented strategy consists
in computing eigenfunctions and eigenvalues with the aid of Betti's formalism, which are then
used as a first-guess for the shooting method. In practice, this strategy works because there are
regions of parameter space where the sharp-boundary model and the diffuse model resemble

each other; once a solution has been obtained in these regions, it is possible to progressively alter the equilibrium parameters and study regions where the two models are not alike.

The present chapter is organized as follows. In section 3.2 we complete the equilibrium model by specifying the vacuum state. Next, in section 3.3, a scalar eigenmode equation for the m-th harmonic of the radial plasma displacement is found. In section 3.4, by imposing matching conditions at the plasma-vacuum interface and at the wall, we obtain a set of coupled equations which serve as boundary conditions for the eigenmode equations. Next, we present wall position versus plasma-beta marginal stability curves for an ideal plasma surrounded by an ideal wall (section 3.6) and a resistive wall (section 3.7). A summary is given in section 3.8.

3.2 Determination of the equilibrium vacuum magnetic field

As a first step towards the stability analysis of external modes, it is mandatory to complete the specification of the equilibrium configuration by determining quantities in between the plasma column edge ($r = a$) and the first wall ($r = r_w > a$). Although some models consider a "cold-plasma" as a transition medium (see, for example, [83]), a more widely used approach assumes vacuum. Thus, the problem consists on determining the vacuum magnetic field only. As with the determination of the plasma equilibrium state in the previous chapter, this is done to leading order in an inverse aspect ratio expansion.

The equilibrium toroidal and poloidal magnetic fields just inside the circularly shaped boundary are given by

$$\boldsymbol{B}_\varphi(a,\theta) = \frac{F_a}{R_o + a\cos\theta}\hat{\boldsymbol{e}}_\phi \ \text{ and } \ \boldsymbol{B}_\theta(a,\theta) = B_\theta(a,\theta)\hat{\boldsymbol{e}}_\theta, \tag{3.1}$$

respectively, where the F free function has been specified in Eq. 2.20 and

$$F_a \equiv F(\Psi(a,\theta)) = constant. \tag{3.2}$$

Likewise, just outside, from the vacuum side, the magnetic field components are given by

$$\boldsymbol{B}_{V\varphi}(a,\theta) = \frac{F_{Va}}{R_o + a\cos\theta}\hat{\boldsymbol{e}}_\phi \text{ and } \boldsymbol{B}_{V\theta}(a,\theta) = B_{V\theta}(a,\theta)\hat{\boldsymbol{e}}_\theta, \tag{3.3}$$

where the constant F_{Va} corresponds to a free function for the vacuum side. Next, matching conditions at the plasma-vacuum transition must be imposed. The continuity of the normal component of the magnetic field is trivially satisfied. As for the continuity of the total pressure:

$$p(a,\theta) + \frac{B^2(a,\theta)}{2\mu_o} = \frac{B_V^2(a,\theta)}{2\mu_o}, \tag{3.4}$$

we observe that the kinetic pressure does not contribute. This happens because the entropy free function is, to leading order, proportional to the poloidal flux (Eq. 2.20) and the fact that we have imposed a homogeneous Dirichlet condition ($\Psi(a,\theta) = 0$) when solving the leading order Grad-Shafranov equation. Therefore, the magnetic pressure is continuous at the plasma-vacuum interface, a condition which can be cast as

$$B_{V\theta}^2(a,\theta) = \frac{F_a^2 - F_{Va}^2}{R_o^2}\left(1 - 2\epsilon\cos\theta\right) + B_\theta^2(a,\theta) + O(\epsilon^3 B_o^2). \tag{3.5}$$

Here, the first term on the RHS is related to surface poloidal currents at the plasma-vacuum interface. Although surface currents are a necessity when the kinetic pressure possesses a finite jump at the plasma plasma-vacuum interface as, for example, in some sharp-boundary models [60, 84, 85, 86, 87, 88], there is no reason for us to retain this contribution, thus, we set $F_{Va} = F_a$. The resulting poloidal magnetic field is continuous and, in particular, at the transition interface is given by

$$B_{V\theta}(a,\theta) = \frac{\epsilon B_o}{q_*}\left[1 + \nu\cos\theta\right]. \tag{3.6}$$

Finally, we construct the quantity:

$$q_V(a,\theta) \equiv \frac{\epsilon B_o}{B_{V\theta}(a,\theta)}, \tag{3.7}$$

and the averages

$$\langle q_V \rangle_a \equiv \frac{1}{2\pi} \int_0^{2\pi} q_V(a, \theta) d\theta, \tag{3.8}$$

$$\left\langle \frac{1}{q_V^2} \right\rangle_a \equiv \frac{1}{2\pi} \int_0^{2\pi} \frac{d\theta}{q_V(a, \theta)^2}, \tag{3.9}$$

which will appear at several points during the stability analysis in section 3.4. This completes the determination of the plasma column and vacuum equilibrium state.

3.3   Scalar eigenmode equation for the radial component of the plasma displacement

For the stability analysis, we employ the standard Frieman-Rotenberg formulation [45], as introduced in section 1.3.2. In this formulation, the Lagrangian displacement ($\boldsymbol{\xi}$) and the perturbed velocity ($\widetilde{\boldsymbol{v}}$) are related through Eq. 1.27. Next, by a Fourier decomposition in time and in the toroidal angle

$$\boldsymbol{\xi}(r, \varphi, \theta) = \boldsymbol{\xi}(r, \theta) e^{-i(n\varphi + \omega t)}, \tag{3.10}$$

Eq. 1.27 leads to $\widetilde{\boldsymbol{v}} = -i\overline{\omega}(\psi)\boldsymbol{\xi}$, where the flux-surface-dependent, Doppler-shifted frequency is defined as

$$\overline{\omega}(\psi) \equiv \omega + n\Omega(\psi). \tag{3.11}$$

Here, it should be recalled that the dimensionless poloidal flux is of the form $\psi = \psi(r, \theta)$ and, for a circularly shaped plasma, it is given by equations 2.34-2.36. In fact, keeping track of this angular dependence makes the subsequent analysis algebraically more involved, even if conceptually not more complicated than the one carried out in [60].

Then, the linearized momentum equation 1.31 reduces to

$$\widetilde{\boldsymbol{F}}(\boldsymbol{\xi}) = -\rho\overline{\omega}^2\boldsymbol{\xi} - 2i\rho\overline{\omega}\Omega\hat{e}_Z \times \boldsymbol{\xi} - \widetilde{\rho}\Omega^2 R\hat{e}_R + (2\rho R\Omega\boldsymbol{\xi} \cdot \nabla\Omega)\hat{e}_R, \tag{3.12}$$

where the standard force operator is given by

$$\widetilde{\boldsymbol{F}}(\boldsymbol{\xi}) = -\nabla\widetilde{p} - \frac{(\nabla \times \widetilde{\boldsymbol{B}}) \times \boldsymbol{B}}{\mu_o} + \boldsymbol{J} \times \widetilde{\boldsymbol{B}}, \tag{3.13}$$

51

and the remainder perturbed quantities are expressed as function of the plasma displacement according to equations 1.27-1.30. In particular, we notice that the last term on the RHS of Eq. 3.12, represents here a finite contribution due to the diffuse nature of the toroidal angular velocity in our equilibrium model. Now, loosely speaking, the momentum equation is separated into a "magnetic part" ($\mathscr{M}$) which depends on the perturbed poloidal magnetic field and in an "inertial part" ($\mathscr{L}$) which depends on the perturbed density, velocity and pressure. This can be accomplished by either taking $\hat{\boldsymbol{e}}_\varphi \cdot \nabla \times (\text{ Eq. 3.12 })$ and, subsequently, eliminating the $\partial_Z(B_\varphi \widetilde{B}_\varphi)$ term from the Z component of the momentum equation, as done in [60] or, equivalently, by applying $\nabla\varphi \cdot \nabla \times (R^2 \text{ Eq. 3.12 })$; the end result is

$$\mathscr{L} = \mathscr{M}, \tag{3.14}$$

where the magnetic contribution is

$$\mathscr{M} = -\nabla\varphi \cdot \nabla \times \left[R^2 \widetilde{\boldsymbol{B}}_p \times \hat{\boldsymbol{e}}_\varphi J_\varphi + \boldsymbol{B} \times \left(\nabla \times \widetilde{\boldsymbol{B}}_p \right) R^2/\mu_o \right], \tag{3.15}$$

and the inertial contribution is given by

$$\mathscr{L} = -\nabla \cdot \left(\rho \overline{\omega}^2 R \boldsymbol{\xi} \times \hat{\boldsymbol{e}}_\varphi \right) + \partial_Z \left[2i\rho\overline{\omega}\Omega R \xi_\varphi + 2\rho R^2 \Omega \boldsymbol{\xi} \cdot \nabla\Omega - \widetilde{\rho}\Omega^2 R^2 - 2\widetilde{p} \right]. \tag{3.16}$$

Continuing, analytical progress is done by assuming an incompressible plasma response

$$\nabla \cdot \boldsymbol{\xi} = 0, \tag{3.17}$$

and by expressing the perpendicular component of both the Lagrangian displacement and perturbed magnetic field as

$$\boldsymbol{\xi}_\perp(r, \theta) = \frac{R^2}{F} \nabla \widetilde{U}(r, \theta) \times \boldsymbol{B}, \tag{3.18}$$

$$\widetilde{\boldsymbol{B}}_\perp(r, \theta) = \nabla \widetilde{\Psi}(r, \theta) \times \nabla\varphi, \tag{3.19}$$

52

respectively, where $\widetilde{U}$ and $\widetilde{\Psi}$ are stream functions. Next, we perform a Fourier decomposition of all perturbed quantities $(\widetilde{Q})$ in the form

$$\widetilde{Q}(r,\theta) = \sum_m \widetilde{Q}_m(r)e^{im\theta}, \tag{3.20}$$

naturally, because of periodicity the short way around the torus m should be an integer. Now, with the purpose of keeping the final expressions as simple as possible, we make the following critical approximations on the parallel gradient as applied to an arbitrary perturbed quantity:

$$\begin{aligned}
\boldsymbol{B} \cdot \nabla \widetilde{Q} &= \sum_m \left[B_r(r,\theta)\frac{d\widetilde{Q}_m(r)}{dr} + i\left[\frac{mB_\theta(r,\theta)}{r} - \frac{nB_\varphi(r,\theta)}{R} \right] \widetilde{Q}_m(r) \right\} e^{i(m\theta - n\varphi)} \\
&= -\sum_m \left[\frac{iB_o}{R_o}h_m(r) + O(\nu) \right][1 + O(\epsilon)]\,\widetilde{Q}_m(r)e^{i(m\theta - n\varphi)},
\end{aligned} \tag{3.21}$$

where the factor h_m is given by

$$h_m(r) = n - m/q(r), \tag{3.22}$$

the safety factor being defined in terms the poloidal flux contribution in Eq. 2.35 as

$$q(r) = \left(\frac{\psi_a'(\overline{r})}{\overline{r}} \right)^{-1}. \tag{3.23}$$

The ϵ approximation is standard when obtaining a simplified governing eigenmode equations. Most notably, Wahlberg and collaborators have approached a variety of stationary plasma scenarios (e.g., [53, 58, 89, 90, 91, 92]) in a systematic way by means of inverse aspect ratio expansions obtaining, in each case, a sequence of governing eigenmode equations up to the required accuracy. On the other hand, an additional approximation in terms of ν has also been performed. In connection with this, we recall that the equilibrium beta limit sets the upper bound $\nu < 1$. The plasma beta parameter ν will come into play through the angular velocity and pressure gradient terms in the final eigenmode equation.

The Fourier decomposition leads to the m-harmonic for the plasma displacement stream function

$$\widetilde{U}_m(r) = \frac{r}{imR_o}\xi_{r,m}(r), \tag{3.24}$$

and, through Faraday's law, to

$$\widetilde{\Psi}_m(r) = \frac{rh_mB_o}{m}\xi_{r,m}(r), \tag{3.25}$$

where $\xi_{r,m}$ represents the m-th harmonic for the radial component of the plasma displacement. Moreover, the $m = 0$ mode ($\xi_{r,0}$) is easily seen to vanish due to incompressibility, it will implicitly be excluded from know on.

Putting all these pieces together we arrive at the m-th poloidal harmonic of the eigenmode equation

$$\mathscr{L}_m = \mathscr{M}_m, \tag{3.26}$$

where the m-th harmonic of the "magnetic term" is the same as in [60]:

$$\begin{aligned}
\mathscr{M}_m &= \left[-\frac{1}{\mu_o}\boldsymbol{B}\cdot\nabla\left(\Delta^*\widetilde{\Psi}\right) + \nabla\varphi \times \nabla(RJ_\varphi)\cdot\nabla\widetilde{\Psi}\right]_m \\
&= \left(-\frac{R_o}{imr}\right)\frac{B_o^2}{\mu_oR_o^2}\left\{(1-m^2)h_m^2\xi_{r,m} + \frac{1}{r}\frac{d}{dr}\left[r^3h_m^2\frac{d\xi_{r,m}}{dr}\right]\right\},
\end{aligned} \tag{3.27}$$

but the m-th poloidal contribution of the "inertial term" is now

$$\begin{aligned}
\mathscr{L}_m &= \left(-\frac{R_o}{imr}\right)\left(\frac{1}{r}\frac{d}{dr}\left[\rho_o\left(\Gamma_m^2 r^3 - KR_o r^2\right)\frac{d\xi_{r,m}}{dr}\right]\right. \\
&\quad \left. - \rho_o\left[(m^2-1)\left(\Gamma_m^2 - \frac{dK}{dr}R_o\right) + Y_m^2\right]\xi_{r,m} + \frac{p_0}{2R_oB_o}P_m(\widetilde{\Psi}_m)\right),
\end{aligned} \tag{3.28}$$

where

$$p_0 = -\epsilon\frac{B_o^2}{\mu_o}\frac{C(\lambda, q_*)}{2}, \tag{3.29}$$

$C(\lambda, q_*)$ being defined by Eq. 2.41.

The non-trivial expressions for the various terms in the inertial contribution result because of a number of reasons: toroidicity, the poloidal flux dependence on the Doppler-shifted frequency, the diffuse nature of the equilibrium angular frequency, etc. In what follows, we find convenient to introduce the radially dependent angular frequencies

$$\Omega_a \equiv \Omega(\psi_a(r)), \tag{3.30}$$

$$\Omega_b \equiv \Omega(\psi_b(r)), \tag{3.31}$$

as well as of the following Doppler-shifted one:

$$\overline{\omega}_a \equiv \omega + n\Omega(\psi_a(r)), \tag{3.32}$$

where the dimensionless poloidal flux contributions $\psi_a(r)$ and $\psi_b(r)$ have been defined before (Eqs. 2.34-2.36). The $\Gamma_m^2(r)$ and $Y_m(r)$ terms are a generalization of the ones which appear in [60]:

$$
\begin{aligned}
\Gamma_m^2(r) \equiv & \left[\overline{\omega}_a^2 + \frac{n^2\Omega_b^2}{2}\right]\left[1 + \frac{1}{h_{m-1}^2} + \frac{1}{h_{m+1}^2}\right] \\
& - \left[2\overline{\omega}_a\Omega_a + \frac{n\Omega_b^2}{2}\right]\left[\frac{1}{h_{m-1}} + \frac{1}{h_{m+1}}\right] - \frac{n^2\Omega_b^2}{2h_{m-1}h_{m+1}},
\end{aligned}
\tag{3.33}
$$

$$
\begin{aligned}
Y_m(r) \equiv & \; r(m-1)\frac{d}{dr}\left[\frac{1}{h_{m+1}^2}\left(\overline{\omega}_a^2 + \frac{n^2\Omega_b^2}{2}\right) - \frac{2\overline{\omega}_a\Omega_a + n\Omega_b^2}{h_{m+1}}\right] \\
& - r(m+1)\frac{d}{dr}\left[\frac{1}{h_{m-1}^2}\left(\overline{\omega}_a^2 + \frac{n^2\Omega_b^2}{2}\right) - \frac{2\overline{\omega}_a\Omega_a + n\Omega_b^2}{h_{m-1}}\right] \\
& - r\frac{d}{dr}\left[\overline{\omega}_a^2 + \frac{n^2\Omega_b^2}{2}\right] - \frac{r}{2}\frac{dQ_m}{dr} - m^2 Q_m,
\end{aligned}
\tag{3.34}
$$

where we have introduced the auxiliary function

$$Q_m \equiv \Omega_b^2 n\left(\frac{1}{h_{m+1}} + \frac{1}{h_{m-1}} - \frac{n}{h_{m+1}h_{m-1}}\right). \tag{3.35}$$

On the other hand, both $K(r)$ and $P_m(r)$ represent new contributions. Interestingly,

$$K(r) \equiv \Omega_a\Omega_b, \tag{3.36}$$

is proportional to ν (throughout the Ω_b term); it represents a high-beta, shear-flow effect that comes into play due to the equilibrium poloidal flux dependence on the angular variable. Finally, the pressure-gradient drive:

$$
P_m\left(\widetilde{\Psi}_m\right) \equiv -m \left\{ \frac{d}{dr}\left[\left(\frac{1}{h_{m+1}} + \frac{1}{h_{m-1}} \right) \psi_b \frac{d\widetilde{\Psi}_m}{dr} \right] + \frac{m}{r}\left(\frac{1}{h_{m+1}} - \frac{1}{h_{m-1}} \right) \psi_b \frac{d\widetilde{\Psi}_m}{dr} + \right.
$$
$$
\left. -m\frac{d}{dr}\left[\left(\frac{1}{h_{m+1}} - \frac{1}{h_{m-1}} \right) \frac{d\psi_b}{dr}\widetilde{\Psi}_m \right] - \frac{m^2}{r}\left(\frac{1}{h_{m+1}} + \frac{1}{h_{m-1}} \right) \frac{d\psi_b}{dr}\widetilde{\Psi}_m \right\},
$$

$$(3.37)$$

has been written in terms of the m-th harmonic for the perturbed poloidal flux.

By equating the inertial and magnetic parts we obtain the governing eigenmode equation. It is more neatly expressed in dimensionless form instead of the SI units we have dealt with so far

$$
\frac{1}{\bar{r}}\frac{d}{d\bar{r}}\left[\left(\bar{r}^3\left(\widetilde{\Gamma}_m^2 - h_m^2 \right) - \frac{\bar{r}^2\widetilde{K}}{\epsilon} \right) \frac{d\widetilde{\xi}_m}{d\bar{r}} \right]
$$
$$
-\left[(m^2-1)\left(\widetilde{\Gamma}_m^2 - h_m^2 - \frac{1}{\epsilon}\frac{d\widetilde{K}}{d\bar{r}} \right) + \widetilde{Y}_m^2 \right]\widetilde{\xi}_m + \frac{\beta_{0\varphi}}{4\epsilon}\widetilde{P}_m(\widetilde{\psi}_m) = 0,
$$

$$(3.38)$$

where $\bar{r} \equiv r/a$, $\widetilde{\xi}_{r,m} \equiv \xi_{r,m}/a$, $\widetilde{\Gamma}_m^2 \equiv \Gamma_m^2/\omega_A^2$, $\widetilde{K} \equiv K/\omega_A^2$, $\widetilde{Y}_m^2 \equiv Y_m^2/\omega_A^2$, $\widetilde{P}_m\left(\widetilde{\psi}_m\right) \equiv P_m\left(\widetilde{\Psi}_m\right)/B_o^2$ and $\widetilde{\psi}_m \equiv \widetilde{\Psi}_m/(B_o a^2)$. Here, $\omega_A \equiv V_{Ao}/R_o$ is the Alfvén frequency at the geometrical center, and $\beta_{0\varphi} \equiv 2\mu_o p_0/B_o^2$ is the plasma beta as defined with the aid of the pressure constant in Eq. 3.29.

By setting $\psi_b \to 0$, $\overline{\omega}(\psi) \to \overline{\omega} = constant$ and $\Omega(\psi_0) \to \Omega = constant$ we recover, save for a centrifugal term, the governing eigenmode equation in [60]. In [60], the toroidal velocity is assumed to scale as $\Omega/\omega_A \sim O(\sqrt{\epsilon})$, on the other hand, in the present model, it has been assumed a slower toroidal rotation profile: $\Omega/\omega_A \sim O(\epsilon)$ (see Table 2.1). The missing centrifugal contribution (corresponding to the last term in [60, Eq. 61]), is negligible in our model.

The eigenmode equation controls the evolution of the m-th harmonic for the plasma displacement. Now, poloidal coupling is an inevitable consequence of the angular (θ) dependence of equilibrium quantities, yet, we have disregarded it when deriving Eq. 3.38. This should be

understood as an extra assumption. Poloidal coupling will be considered at the plasma-vacuum transition.

3.4   Matching conditions

The stability analysis continues by recognizing that the perturbed value of the total pressure (as introduced in Eqs. 1.35, 1.36) is continuous at the movable plasma-vacuum interface:

$$\left[\left[\widetilde{p} + \frac{B\widetilde{B}_{\parallel}}{\mu_o} + \xi_n \nabla_n \left(p + \frac{B^2}{2\mu_o}\right)\right]\right]_a = 0, \tag{3.39}$$

where n stands for the normal direction at this interface, that is, for the radial direction given we are considering a circular plasma edge. Two contributions can be readily recognized in Eq. 3.39: the "fixed boundary jump" (the first two terms) and the "free boundary jump" (the term proportional to the normal plasma displacement). The "fixed boundary jump" can be handled, on the plasma side, by direct manipulation of the linearized eigenmode equation 3.12 and, in the vacuum side, by the introduction of a magnetic scalar potential as explained later on. On the other hand, the "free boundary jump" can, in turn, be split into two contributions, one corresponding to a kink mode drive for instabilities and the other one associated with a ballooning mode drive. In either case, their evaluation requires the computation of the normal component of the curvature vector both from the plasma and vacuum sides, which are computed to leading order in an inverse aspect-ratio expansion. Continuing, the kink mode drive appears as the average magnetic pressure times the jump in the curvature at the interface and can be cast as a quantity proportional to the difference $\langle 1/q_V^2 \rangle_a - 1/q_a^2$. Even though the equilibrium magnetic field is continuous at the plasma-vacuum interface, the kink mode drive is finite due to the θ dependence of the poloidal vacuum magnetic field, which we constructed in the last section (see Eq. 3.6). In regard to the ballooning mode drive, this quantity appears as the plasma pressure times the average curvature across the interface. However, as already argued, the equilibrium pressure vanishes at the plasma edge, implying that the ballooning drive vanishes. This is not to say that pressure driven modes are not captured by our model, in fact, the opposite is true. Contrary to surface current models, where pressure driven modes come into play from

the evaluation of the "free boundary jump", our diffuse model incorporates this drive in a "distributed way" across the plasma column at the differential equation level (as shown in Eqs. 3.37-3.38). As the result of these algebraic manipulations, the m-th Fourier component for the matching condition 3.39 is written as:

$$\frac{h_m(a)a\widetilde{\Psi}'_m(a)}{m}\left[\frac{\Gamma^2_{2m}}{\omega^2_A h^2_m}-1\right]_a + \widetilde{\Psi}_m(a)\left[\frac{3\nu^2}{2q^2_*}\frac{m}{h_m}+\frac{\Xi^2_m}{\omega^2_A h_m}\right]_a = R^2_o\left[\frac{\boldsymbol{B}_V\cdot\widetilde{\boldsymbol{B}}_V}{B_o}\right]_m\bigg|_a. \quad (3.40)$$

The terms Γ^2_{2m} and Ξ^2_m come from the fixed boundary jump evaluation and are given by the non-trivial expressions:

$$\begin{aligned}\Gamma^2_{2m} \equiv &\left[\overline{\omega}^2_a+\frac{n^2\Omega^2_b}{2}\right]\left[1+\frac{1}{h^2_{m-1}}+\frac{1}{h^2_{m+1}}\right]\\&-\left[2\overline{\omega}_a\Omega_b+\frac{n\Omega^2_b}{2}\right]\left[\frac{1}{h_{m-1}}+\frac{1}{h_{m+1}}\right]-\frac{R_o\Omega_a\Omega_b}{ma},\end{aligned} \quad (3.41)$$

and

$$\begin{aligned}\Xi^2_m \equiv &\left[\overline{\omega}^2_a+\frac{n^2\Omega^2_b}{2}\right]\left[\frac{1}{h^2_{m-1}}-\frac{1}{h^2_{m+1}}\right]+\frac{n^2\Omega^2_b}{2h_{m-1}h_{m+1}}\\&+2\left[\overline{\omega}_a\Omega_a+\frac{n\Omega^2_b}{2}\right]\left[\frac{1}{h_{m-1}}-\frac{1}{h_{m+1}}\right]-\frac{r}{q^2 h_m}\frac{dq}{dr}\Gamma^2_{2m}.\end{aligned} \quad (3.42)$$

The kink mode drive is identified here as the term proportional to ν^2/q^2_* in Eq. 3.40, has a larger destabilizing influence in high-beta regimes (which is also true in a static scenario [16, Eqns. 12.137-12.140]). Here, $\widetilde{\boldsymbol{B}}_V$ stands for the perturbed magnetic field in the vacuum region surrounding the plasma. As done extensively in the literature (e.g., [16]), the remaining stability analysis consists of incorporating the resistive wall physics into Eq. 3.40 regarding $\widetilde{\boldsymbol{B}}_V$ as an intermediate quantity.

Vacuum solutions are needed for both the vacuum region in between the plasma and the wall ($a < r < r_w$) and for the secondary vacuum region outside the wall itself ($r_w < r < \infty$). The wall is assumed to have a finite with (d), which is ordered as $d << r_w$ (the so-called "thin-wall approximation"), and to possess a finite electrical resistivity (η_w), so that the characteristic wall diffusion time is

$$\tau_w = \frac{\mu_o d r_w}{\eta_w}. \quad (3.43)$$

Vacuum solutions in each region are coupled by means of appropriate boundary conditions and then connected to Eq. 3.40 by imposing the continuity of the perturbed normal component of the magnetic field at the plasma-vacuum transition:

$$[[\widetilde{B}_r]]|_a = 0. \tag{3.44}$$

Given that the magnetic field is curl-free in vacuum regions, it can be written in terms of a magnetic potential

$$\widetilde{\boldsymbol{B}}_V = \nabla \widetilde{V}, \tag{3.45}$$

which obeys Laplace's equation

$$\nabla^2 \widetilde{V} = 0. \tag{3.46}$$

By expressing the Laplace's equation in toroidal coordinates and then employing an inverse aspect ratio expansion, the m-th Fourier component for the leading order inner vacuum potential is easily found to be

$$\widetilde{V}_m^{inner} = \left(C_{1,m}\hat{r}^{|m|} + C_{2,m}\hat{r}^{-|m|}\right) e^{-i\omega t + im\theta - in\varphi}, \tag{3.47}$$

while the outer contribution is

$$\widetilde{V}_m^{outer} = C_{3,m}\hat{r}^{-|m|} e^{-i\omega t + im\theta - in\varphi}, \tag{3.48}$$

where we have used the normalized variable $\hat{r} = r/r_w$. The thin wall approximation then translates into jump conditions for the magnetic potentials:

$$\frac{\partial \widetilde{V}_m^{outer}}{\partial r} = \frac{\partial \widetilde{V}_m^{inner}}{\partial r}, \tag{3.49}$$

$$\frac{\partial^2 \widetilde{V}_m^{outer}}{\partial r^2} = \frac{\partial^2 \widetilde{V}_m^{inner}}{\partial r^2} - \frac{i\omega\mu_o d}{\eta_w}\frac{\partial \widetilde{V}_m^{inner}}{\partial r}. \tag{3.50}$$

After a somewhat lengthy but standard manipulation, the RHS of Eq. 3.40 can be expressed as the superposition of multiple harmonics for the perturbed poloidal flux

$$R_o^2 \left[\frac{\boldsymbol{B}_V \cdot \nabla \widetilde{V}^{inner}}{B_o} \right]_m \bigg|_a = \sum_{\substack{j=-\infty \\ j \neq 0}}^{\infty} \hat{\delta}_{m,j} \widetilde{\Psi}_j(a), \tag{3.51}$$

the coupling coefficients $\hat{\delta}_{m,j}$ are given by the infinite sum

$$\hat{\delta}_{m,j} = \frac{j}{h_j(a)} \sum_{\substack{l=-\infty \\ l \neq 0}}^{\infty} |l|^{-1} \hat{\sigma}_l G_{l-j}^l(a) G_{m-l}^l(a). \tag{3.52}$$

As expected, they are progressively less significant because of the factor $|l|^{-1}$. The parameter G_l^m appears throughout the literature [16, 84] and it is defined by

$$G_l^m = \frac{1}{\pi} \int_0^\pi \left(\frac{m}{q_V(a, \theta)} - n \right) \cos(l\theta) d\theta, \tag{3.53}$$

yet, for our equilibrium model, it takes a very simple form

$$G_l^m = \left(\frac{m\nu}{2q_*} \right) \delta_{-1,l} + \left(\frac{m}{q_*} - n \right) \delta_{0,l} + \left(\frac{m\nu}{2q_*} \right) \delta_{1,l}, \tag{3.54}$$

here, $\delta_{i,l}$ stands for the standard Kronecker delta and should not be confused with $\hat{\delta}_{i,l}$, as defined by Eq. 3.52. Equation 3.54 implies that only a finite number of coupling terms in Eq. 3.52 do not vanish. That is to say, in our model, the poloidal coupling that enters through the boundary conditions is "not as extended" as in the sharp-boundary description [60]. Ultimately, this is because the equilibrium pressure profile vanishes at the plasma edge for the diffuse model. Additionally, as indicated by the ν dependence in Eq. 3.54, mode coupling is more pronounced in high-beta scenarios and, for a vanishing beta scenario, it disappears completely. Finally, the coefficient $\hat{\sigma}_l$ incorporates the resistive wall physics into the problem, it is given by

$$\hat{\sigma}_l = \frac{2|l| + i\omega\tau_w \left[1 + \left(\frac{a}{r_w} \right)^{2|l|} \right]}{2|l| - i\omega\tau_w \left[1 - \left(\frac{a}{r_w} \right)^{2|l|} \right]}. \tag{3.55}$$

60

Energy dissipation at the resistive wall renders the eigenvalue problem non-selfadjoint. Finally, ideal walls can be recovered in the $\tau_w \to \infty$ limit, where $\hat{\sigma}_l$ takes the form:

$$\hat{\sigma}_l = \frac{1 + \left(\frac{a}{r_w}\right)^{2|l|}}{1 - \left(\frac{a}{r_w}\right)^{2|l|}}. \qquad (3.56)$$

To sum up, each poloidal flux harmonic ($\widetilde{\Psi}_m$) is coupled with a small number of side-band components ($\widetilde{\Psi}_j$) by means of the equation

$$\frac{h_m(a)a\widetilde{\Psi}'_m(a)}{m}\left[\frac{\Gamma^2_{2m}}{\omega_A^2 h_m^2} - 1\right]_a + \frac{\widetilde{\Psi}_m(a)}{h_m(a)}\left[\frac{3\nu^2 m}{2q_*^2} + \frac{\Xi^2_m}{\omega_A^2}\right]_a = \sum_{\substack{j=-\infty \\ j \neq 0}}^{\infty} \hat{\delta}_{m,j}\widetilde{\Psi}_j(a). \qquad (3.57)$$

The formalism incorporates a kink mode drive for instabilities and resistive wall effects. In the vanishing beta limit, the modes decouple from each other. Pressure and shear-flow drives are captured by the eigenmode equation 3.38.

3.5   Multidimensional shooting method implementation

For a given collection of side-bands $M_{min} \leq m \leq M_{max}$ (with $m \neq 0$), the eigenvalue problem at hand consists in determining the solution of $M_{max} - M_{min} + 1$ ODE's of the form 3.38 and the corresponding complex eigenfrequency ω, which satisfy the coupling boundary conditions 3.57. Additionally, harmonic contributions for the plasma displacement ($\xi_{r,m}$) are required to be regular at the origin ($r = 0$). In connection with this, we note that the governing ODE possesses a regular singularity at the origin. This singularity is easily taken care of and the end result is that solutions near the origin behave as

$$\xi_{r,m} = c_m r^{-1+|m|}, \qquad (3.58)$$

where the collection of c_m's are arbitrary complex constants. Certainly, one of these constants can be chosen in an arbitrary way without loss of generality (say, the one corresponding to $m = M_{max}$). Thus, the eigenvalue problem consists on choosing $M_{max} - M_{min} + 1$ complex

numbers: $\{\omega,\ c_{M_{min}},\ c_{M_{min}+1},...,c_{M_{max}-1}\}$ consistent with the boundary conditions 3.57. In regards to the numerical integration, it is carried out starting at a point r_o (with $0 < r_o << a$) where continuity of the plasma displacement and its derivative, as computed from 3.58, are imposed.

The sharp-boundary formalism in [60] is ultimately expressed in terms of a dispersion relation, which can be solved by a root-finding method over the complex plane. On the other hand, in a multidimensional shooting method, like the one we have implemented, it is critical to have good initial guesses for the method to converge. The employed strategy is to choose equilibrium parameters for which the diffuse model resembles the sharp-boundary one and to subsequently obtain a good initial guess by solving for the eigenvalues and eigenvectors employing the matrix eigenvalue formalism from [60]. Then, by progressively changing equilibrium parameters, it is possible to explore regions of parameter space where the models significantly differ.

3.6 Beta limits of rotating ideal plasmas in the presence an ideal wall

The aim of this section is to study the onset of ideal external kinks modes (IKM's) in the presence of an ideal wall and toroidal plasma rotation. For (qualitative) comparison purposes, we present results corresponding to both our diffuse model and two variations of the sharp-boundary one.

We consider equilibria with fixed values of the kink safety factor $q_* = 1.6, 1.8$, an inverse aspect ratio of $\epsilon = 0.25$ and set $\lambda = 0$. Beta limits are computed for an ideal wall ($\tau_w \to \infty$) by using the coupling coefficient in Eq. 3.56. Stability boundaries are found for the $n = 1$ toroidal mode by retaining the coupling between six poloidal modes $m = -1, 1, 2, 3, 4, 5$ (as previously argued, $m = 0$ does not contribute). Figure 3.1 shows the results of these calculations in scenarios with and without plasma flow. These stability curves are found by fixing the wall radius (r_w), progressively increasing β and computing, at each point (r_w, β), eigenvector/eigenvalue pairs. Marginal stability is defined by the condition $\mathbb{Im}\{\omega\} = 0$; however, in practice, as we increase beta, we look for the first point at which $\mathbb{Im}\{\omega\}$ is larger than an arbitrarily chosen small positive number. By setting the plasma rotation to zero and the wall radius to $r_w/a = 300$ we

determine the "no-wall" stability boundaries $\beta/\epsilon = 0.0556$ and $\beta/\epsilon = 0.1283$ corresponding, respectively, to $q_* = 1.8$ and $q_* = 1.6$ (only the first of these limiting values being explicitly shown in the graph). Our study focuses on external kink modes when there are no resonant surfaces located inside the plasma; in this respect, as computed from Eq. 2.45, figure 3.2 shows an increase of the edge safety factor (q_a) with β/ϵ when the kink safety factor is constant. To avoid the onset of the $m/n = 2/1$ tearing mode, an upper limit $q_a < 2$ should be imposed, which translates into the $\beta/\epsilon < 0.2422$ and $\beta/\epsilon < 0.375$ constraints for $q_* = 1.8$ and $q_* = 1.6$, respectively. This is the reason why the stability curves in figure 3.1 are broken. For a fixed β value, below a given marginal curve the ideal wall is sufficiently close to provide stabilization, but above it IKM's set in. Before discussing the effect of rotation, let us qualitatively compare these curves with the ones computed from sharp-boundary models.
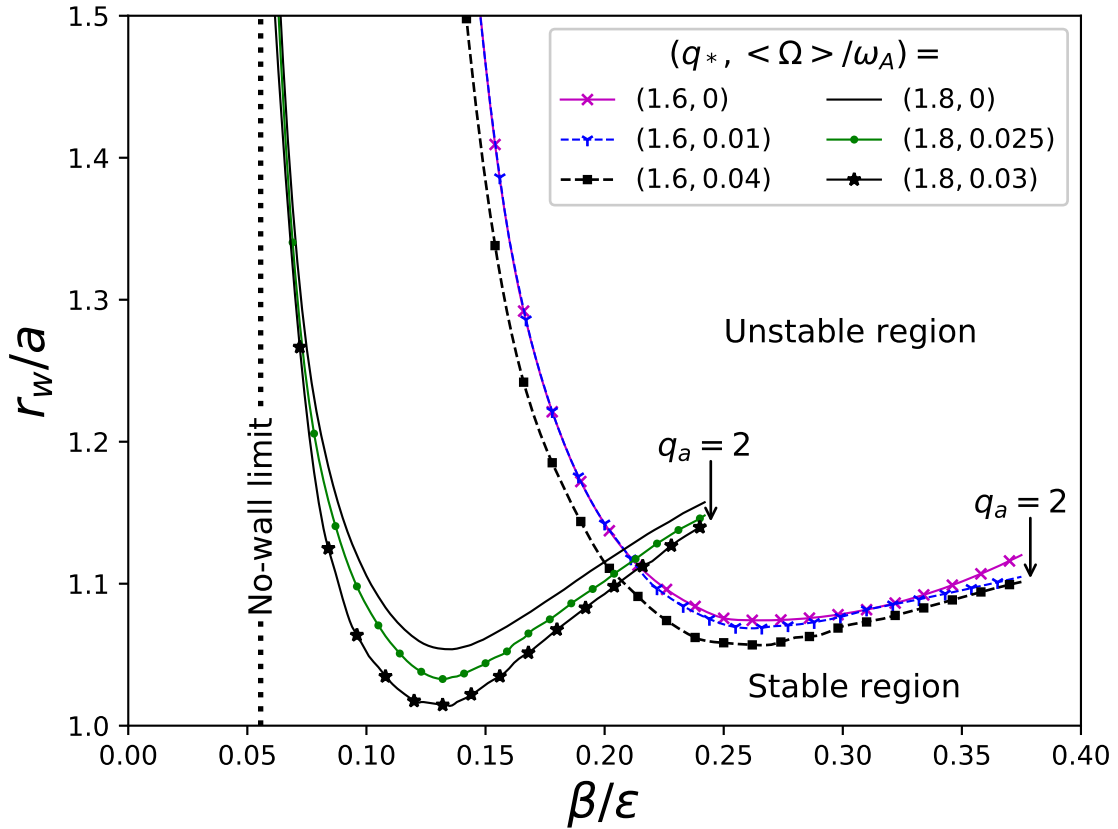
Figure 3.1: Beta limits versus wall position for the $n = 1$ mode in rotating ideal plasmas with an ideal wall. For all curves, $\epsilon = 0.25$ and $\lambda = 0$. For each curve, corresponding to a fixed value of the kink safety factor (q_*), the plasma beta is varied up to the value at which $q_a = 2$ (see figure 3.2). The no-wall limit for the $q_* = 1.8$ case is explicitly shown, it corresponds to $\beta/\epsilon = 0.0556$.
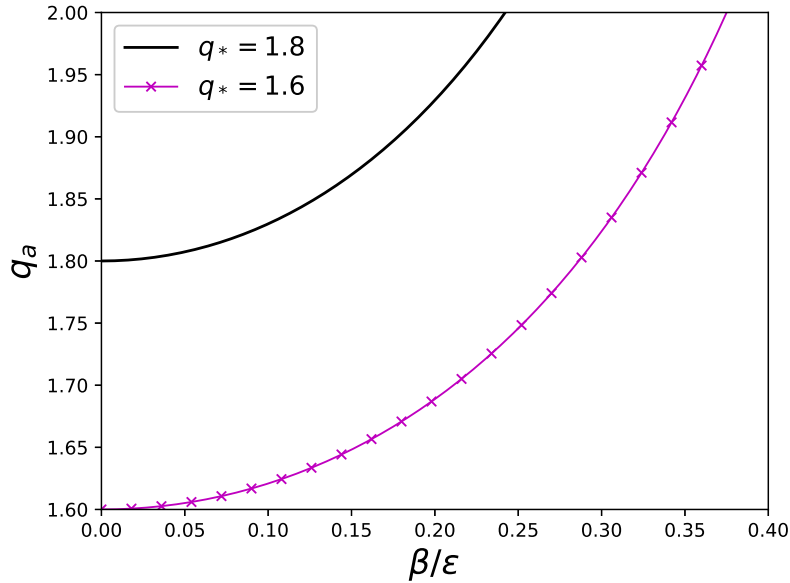
Figure 3.2: Safety factor at the plasma edge as function of β/ϵ as computed from Eq. 2.45.

In the sharp-boundary formalism introduced in [60], the plasma column is composed of an inner region with a constant safety factor ("the current channel") and an outer thin region ("the edge") where the safety factor grows quadratically. Tearing mode resonances can be accommodated at the edge. We consider equilibria with values of the safety factor at the center and at the edge of $q_0 = 1.1$ and $q_a = 1.9$, respectively, so that internal resonances are avoided. Figure 3.6 illustrates, for a static scenario with $\epsilon = 0.25$, how the $n = 1$ stability curves develop first and second stability regions as the average safety factor from the vacuum side takes the values $\langle q_V \rangle_a = 2.0, 2.2, 2.5$. As is commonly explained in the literature, for certain values of the wall radius, as β is increased, the plasma transitions from the first stability regime to an unstable one followed by a second stability window. As previously discussed, in our diffuse model the plasma pressure profile vanishes at the plasma edge, ultimately implying $\langle q_V \rangle_a = q_a$, yet, first and second stability regions are clearly seen for the diffuse model in figure 3.1.

The sharp-boundary results presented here have a two-fold purpose, they constitute a scenario the diffuse model can be compared against and, equally important, they are the basis for the "first-guess-generator". Coming back to the stability boundaries in figure 3.6, it should be pointed out that they are approximate; specifically, although correct matching conditions at the current channel-edge transition have been imposed, we have assumed that the form of the

eigenfunction at the plasma edge is the same as in the current channel. A more comprehensive, perturbative method, was developed to deal with this region in [60], mainly to incorporate internal resonances; however, as already pointed out, we exclude them from this work. For the purposes of building a simple first-guess-generator we have removed the plasma edge from the sharp-boundary model, i.e., the eigenmode equation and boundary conditions in [60] have been consistently simplified. The resultant configuration possesses a constant safety factor across the plasma column. Since the form of the eigenfunctions is analytically known in such simple scenario, the result is a straightforward "exact" (up to numerical accuracy and number of poloidal modes included) eigenpair generator. Some benchmarks for the sharp-boundary numerical codes include: i) recovering the $\beta/\epsilon = 0.21$ no-wall stability limit for the static, current-free plasma with a constant pressure profile from [84, 60] as well as ii) stability curves for the $n = 1, 2, 3$ modes appearing in Fig. 4 from [84] and iii) recovering the approximate stability curves for the $n = 1$ mode in an ideal plasma with an ideal wall from Fig. 2 in [60].

Figure 3.6 illustrates beta limits versus wall position for the simplified sharp-boundary model. We have set $\epsilon = 0.25$ and vary the kink safety factor $q_* = 1.1 - 1.8$. In this model $q_a = q_*$. On the other hand, in spite of the discontinuous character of the sharp boundary model at the plasma-vacuum transition, it is possible to set $\langle q_V \rangle_a = q_a$ as in the diffuse model. In figure 3.6, it is seen that the stability boundaries associated with $q_* = 1.6$ and $q_* = 1.8$ maintain the same relative position as in figure 3.1, however, they are "mostly flat" along the β-window, and display only a relatively narrow second stability region at high-β values. Overall, the marginal stability curves predicted by means of the diffuse equilibrium lie below the sharp-boundary ones (with and without the plasma edge), i.e., the stable operational space for the diffuse model is restricted compared to the one corresponding to a sharp-boundary scenario.

The effect of toroidal rotation is exemplified in figures 3.1 and 3.5 for the diffuse model and for the sharp-boundary one without the plasma edge, respectively. We consider equilibria with rotation values of few percent the Alfvén frequency. Angular toroidal rotation is solid for the sharp-boundary model but depends on the poloidal flux variable for the diffuse equilibrium. For the diffuse model, we define the average angular toroidal rotation ($\langle \Omega \rangle$) over the plasma
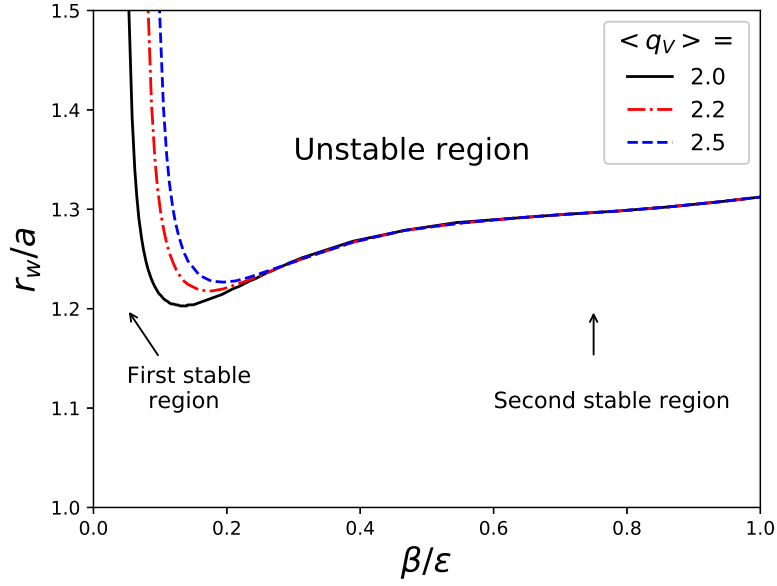
Figure 3.3: Beta limits versus wall position for the $n = 1$ mode in ideal plasmas with an ideal wall under a sharp boundary model. We employ the sharp bundary model on [60], consisting of a constant safety factor across most of the plasma column, but which grows quadratically in a thin region at the plasma edge. We have set the central value for the safety factor to $q_0 = 1.1$, its value at the edge to $q_a = 1.9$ and vary the quantity $< q_V >$. Also, $\epsilon = 0.25$ and $\Omega = 0$. Compare the first and second stable regions with the ones in figure 3.1
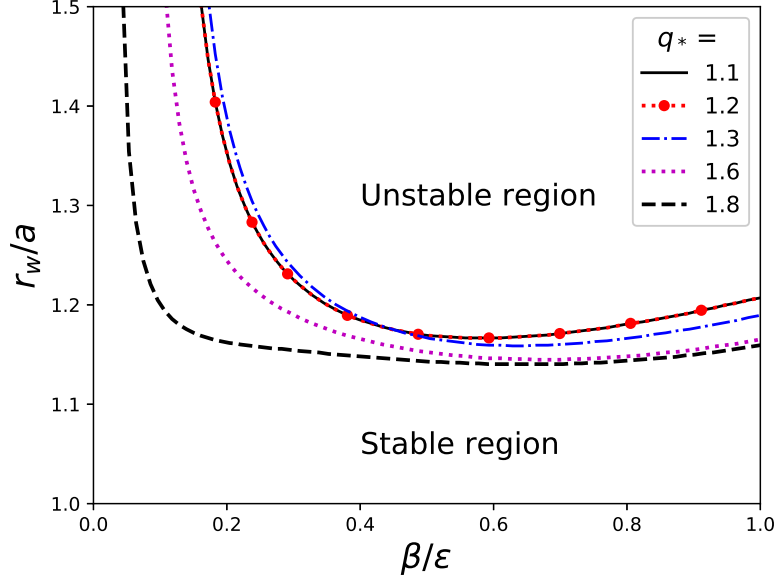
Figure 3.4: Beta limits versus wall position for the $n = 1$ mode in ideal plasmas with an ideal wall. We employ a sharp boundary model based in [60] with a constant safety factor across the plasma column. In this model $q_* = q_a$. To compute these curves, we have set $< q_V >= q_a$, $\epsilon = 0.25$ and $\Omega = 0$.

volume (V_p) as the quantity

$$\langle \Omega \rangle \equiv \frac{1}{V_p} \int \Omega(\psi(\overline{r}, \theta)) d^3\overline{r}. \tag{3.59}$$

66

For the sharp-boundary model, the presence of rotation is slightly destabilizing in the low-beta region and slightly stabilizing in the high-beta region. However, a meaningful comparison with the diffuse model can only be done in the low-beta regime and, for this reason, we have limited the β-window in figure 3.5 to the same one in figure 3.1. It is clear that, for the same rotation values, rotation has a stronger destabilizing effect for the diffuse model than for the sharp-boundary one. Plausibly, the stronger destabilizing effect flow has on the diffuse equilibrium results from a global shear-flow drive, absent in the sharp-boundary model due to its solid body rotation.
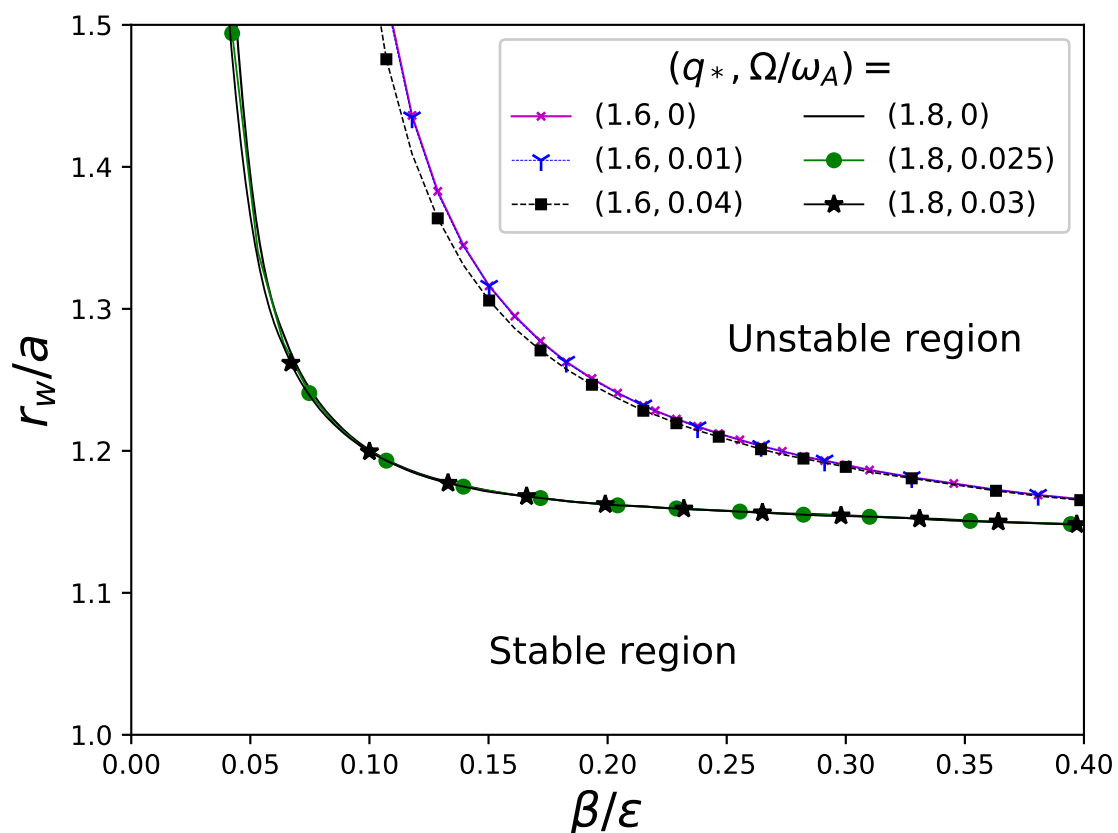
Figure 3.5: Beta limits versus wall position for the $n = 1$ mode in rotating ideal plasmas with an ideal wall. As in figure 3.6, the equilibrum model is a sharp boundary one with a constant safety factor across the plasma column. We have set $< q_V >= q_a$ and $\epsilon = 0.25$. In this model, the plasma rotation is as a solid body. To ease comparison with the stability curves for the diffuse model from figure 3.1, we plot the results in the same β/ϵ window and employ the same rotation values.

The destabilizing effect of flow is further illustrated in figures 3.6 and 3.7 for the diffuse equilibrium. At a fixed wall radius of $r_w/a = 1.1$, and parameters $q_* = 1.8$, $\epsilon = 0.25$,

$\lambda = 0$, they illustrate the onset of ideal external kink modes as the pressure increases and the subsequent transition into the second stability region. It is seen that the growth rates ($\gamma \equiv \mathbb{Im}\{\omega\}$) are a fraction of the Alfvén frequency. The maximum value of the growth rate slightly increases with rotation, and the beta limits decrease with it. The destabilizing nature of flow has been identified before as the combined of centrifugal, Coriolis and (in our case) shear-flow effects.
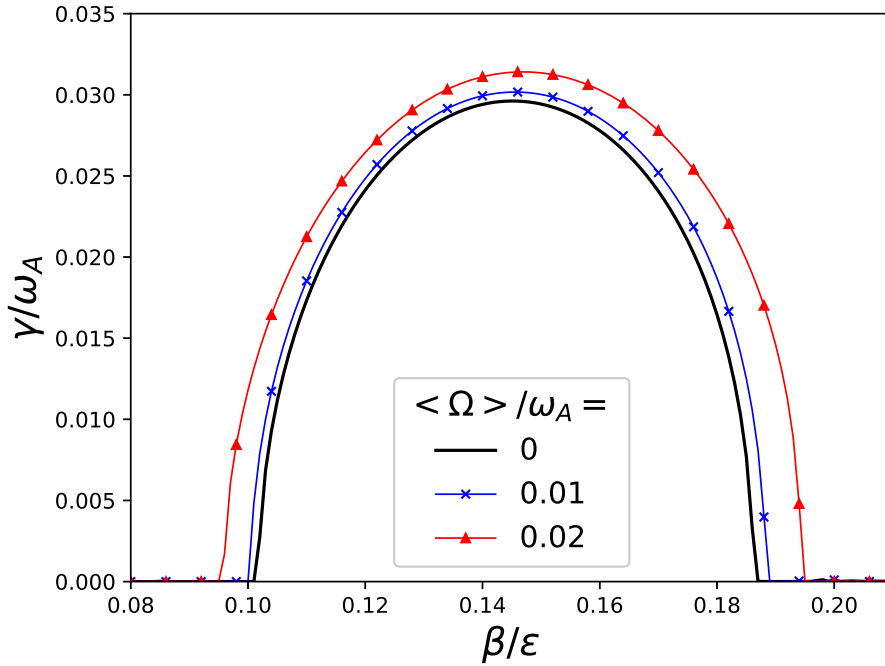
Figure 3.6: Growth rate versus β/ϵ for the $n = 1$ mode in rotating ideal plasmas with an ideal wall. For all curves, $q_* = 1.8$, $\epsilon = 0.25$, $\lambda = 0$ and $r_w = 1.1a$. These curves represent ideal external kink modes (IKM's).

3.7 Beta limits in the presence of resistive walls

It is well established that the presence of resistive walls allows the perturbed magnetic field to diffuse across them in the characteristic time τ_w. Ideal plasmas possessing betas above the no-wall limit, which originally are stabilized by an ideal wall, will develop slowly growing modes as the perturbed magnetic flux penetrates the resistive wall. Effectively, a resistive wall reduces the beta-limits to the no-wall limits.

Figure 3.8 illustrates, for the same parameters employed in figure 3.6: $q_* = 1.8$, $\epsilon = 0.25$, $\lambda = 0$ and $r_w/a = 1.1$, the development of an ideal-plasma-resistive-wall-mode (IPRWM).
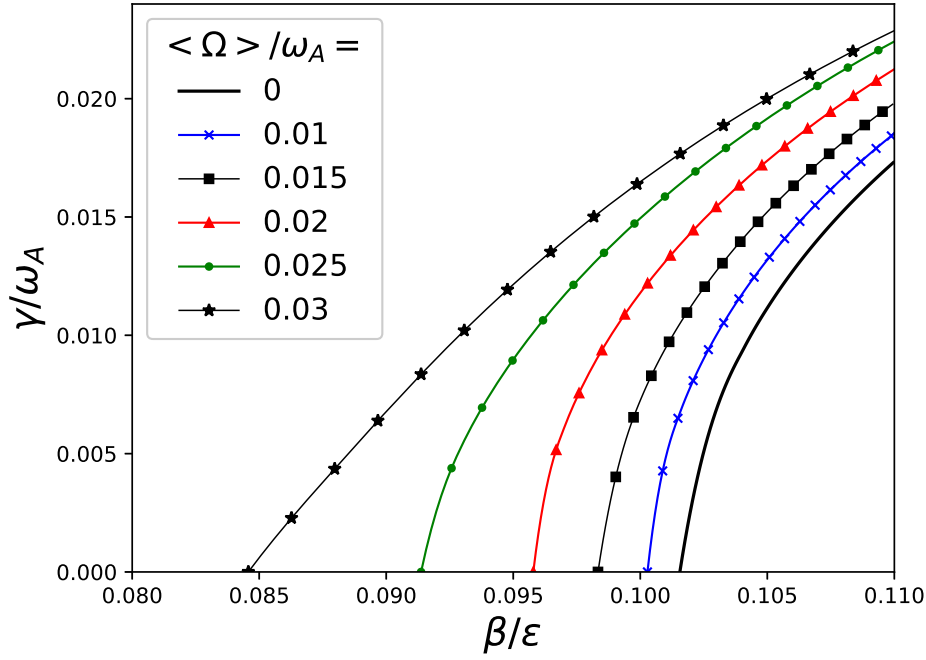
Figure 3.7: Growth rate versus β/ϵ for the $n = 1$ mode in rotating ideal plasmas with an ideal wall. This plot corresponds to zooming into the low-beta regime in figure 3.6, and the same parameters are employed for all curves: $q_* = 1.8$, $\epsilon = 0.25$, $\lambda = 0$ and $r_w = 1.1a$.

Figure 3.8 shows three static equilibria, the first one with an ideal wall and the remaining two with resistive walls, their characteristic time being equal to $\tau_w \omega_A = 2 \times 10^3, 4 \times 10^3$. In this respect, observe that for a deuterium plasma with a minor radius $a = 1\ m$, a major radius $R_o = 4\ m$ and an ion temperature $T_i = 3keV$, the characteristic Alfvén time is $\tau_A = 1/\omega_A = 1.1 \times 10^{-5}s$, moreover, setting $r_w \sim a$ and assuming a $d = 1\ mm$ thick stainless steel wall with a resistivity $\eta = 11 \times 10^{-8} Ohms\ m$ we obtain a resistive time of $\tau_w = 1.1 \times 10^{-2}s$ and a product $\tau_w \omega_A = 1.1 \times 10^3$, similar to the cases seen in figure 3.8. Further, from figure 3.8 it is seen that both resistive curves correctly converge to the $\beta/\epsilon = 0.0556$ no-wall limit; additionally, consistent with standard theory, we note that IPRWM's destroy the second stability region. The "restive domes" presented here are similar to the ones in sharp-boundary models seen in Fig. 5 from [60] and Fig. 2 from [88].

The ideal wall case is handled using the coupling coefficient in Eq. 3.56, while resistive cases use Eq. 3.55. In regards to the numerical solution, due to the complicated fashion in which the eigenfrequency appears in the coupling coefficient for the resistive case, as compared to the ideal case, it is intuitive that "IKM domes" are easier to compute than resistive modes.

Further, as the the diffusion time (τ_w) increases, computing the resistive tails might become challenging since their growth rate scales as $O(\tau_w^{-1})$. However, our code is currently able to deal with realistic values of the wall diffusion time.
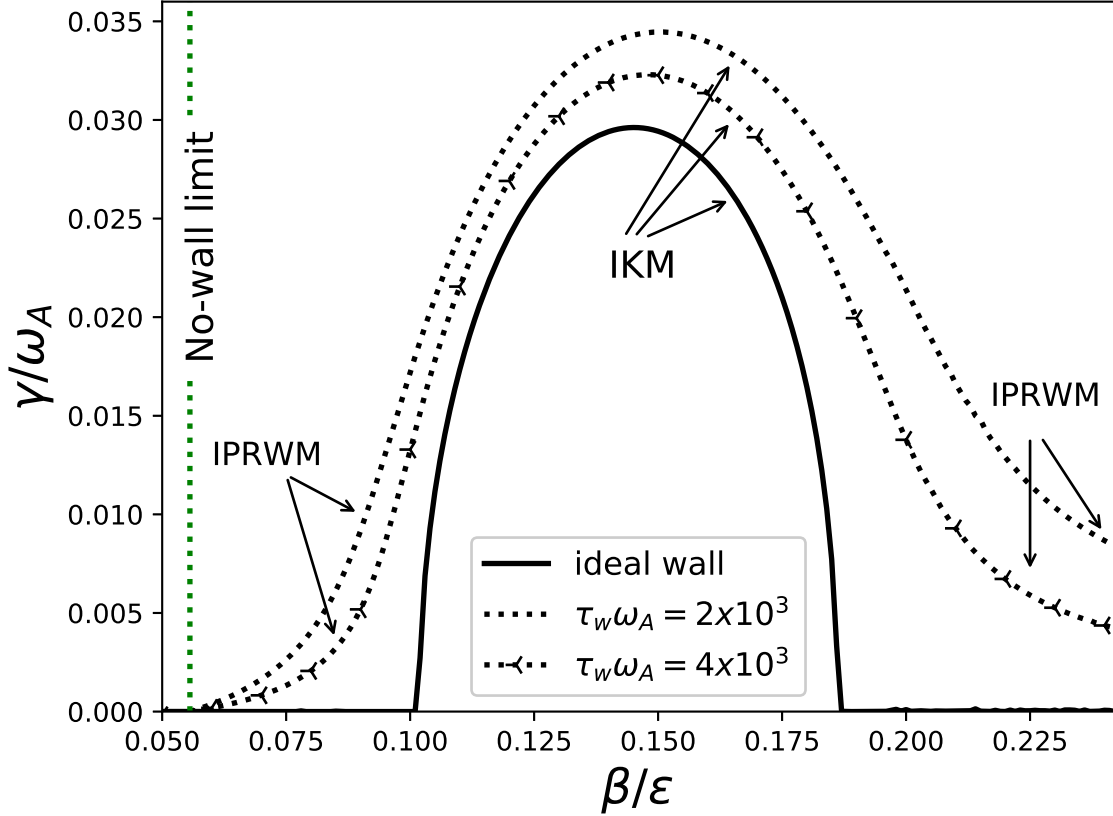
Figure 3.8: Growth rate versus β/ϵ for the $n = 1$ mode in static ideal plasmas with resistive and ideal walls. The tails of these curves represent ideal-plasma-resistive-wall-modes (IPRWM's). For all curves, $q_* = 1.8$, $\epsilon = 0.25$, $\lambda = 0$, $r_w = 1.1a$ and $< \omega >= 0$. We have also indicated the no-wall limit from figure 3.1.

The combined effect of rotation and resistivity is shown in figure 3.9. Here, we have set $q_* = 1.8, \epsilon = 0.25 , \lambda = 0, r_w/a = 1.1, \tau_w\omega_A = 2\times10^3$ and $< \omega > /\omega_A = 0, 0.01, 0.025, 0.03$. Solid curves represent IKM's originally shown in figure 3.7, while dotted lines correspond to IPRWM's resultant by the addition of resistivity in the wall. It is seen that the presence of both rotation and resistivity reduces the beta stability limits to values slightly below the no-wall (static) limit.
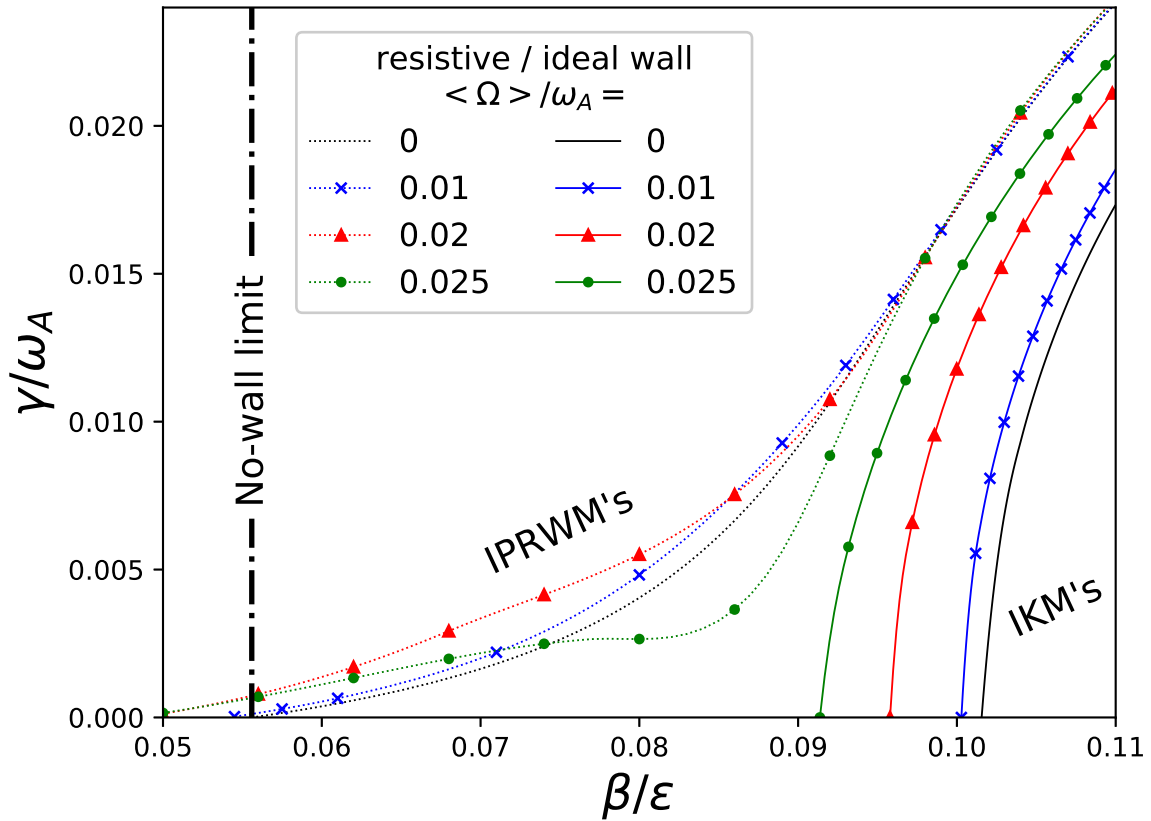
Figure 3.9: Growth rate versus β/ϵ for the $n = 1$ mode in rotating ideal plasmas with ideal and resistive walls in the low-beta regime. Solid/dotted lines correspond to ideal/resistive walls. The IKM's shown here (solid curves), are also presented in figure 3.7. For all curves: $q_* = 1.8$, $\epsilon = 0.25$, $\lambda = 0$ and $r_w = 1.1a$. For the resistive case we consider $\tau_w \omega_A = 2 \times 10^3$. We have also indicated the no-wall limit from figure 3.1.

3.8   Summary of results

In this chapter, we have studied the development of ideal external kink modes (IKM's) and ideal-plasma-resistive-wall-modes (IPRWM's) in the presence of a diffuse angular toroidal rotation profile. The stability analysis is built upon the closed-form analytical equilibrium for a circular cross-section constructed in chapter 2, which incorporates flows in a self-consistent way.

The linear stability analysis carried out here is standard in the field: it consists of reducing the Frieman-Rotenberg formulation to a set of scalar second order eigenmode equations, each one describing the evolution of a given Fourier harmonic, and all of them being coupled together at the plasma-vacuum transition by means of appropriate matching conditions, which

in turn incorporate the effect of the resistive wall. The resulting formalism is a generalization of the sharp-boundary model presented in [60]. While the stability problem for the sharp-boundary equilibrium model is recast as a matrix eigenvalue problem [60], a possibility arising from the perturbative way its associated eigenmode equation is solved, the diffuse model is not tractable in this way. Instead, a multidimensional shooting method has been implemented. Although, in general, multidimensional shooting methods fail to converge unless a good guess is provided, the dispersion relation supplied by the sharp-boundary formalism constitutes an efficient way to generate the necessary first guesses.

The Frieman-Rotenberg formulation reduction to a second order normal mode equation for the radial displacement is accomplished under a number of assumptions, which are done in order to make analytical progress. We identify three critical assumptions: i) the plasma perturbation is incompressible (even though at the equilibrium level the plasma is compressible), ii) the parallel component of the wave vector is computed as if the equilibrium poloidal flux depends on the radial component only and iii) poloidal coupling can be neglected across the plasma column and enters through the matching conditions at the plasma-vacuum transition exclusively. Assumption i) is common in the literature, yet, contrary to static situations, where the most unstable perturbations are incompressible, here, it would require additional justification (for a justification of this point, in the context of a solid rotation profile, see Appendix C in [60]). Assumption ii) is valid in the vanishing ν (beta) limit; in connection with this, we note that results from sections 3.6-3.7 are focused on the low-beta regime, even if the originally stated reason we have restricted our study to this region has been to avoid internal resonances. As a consequence of these approximations, the eigenvalue problem is cast as a set of algebraic equations which incorporate a kink mode drive for instabilities and resistive wall effects, while pressure and shear-flow drives are captured by the eigenmode equation 3.38.

Although a full numerical implementation would be beneficial to evaluate the validity of the approximations previously mentioned, our results are consistent with standard theory, at least in a qualitative way. In particular, the diffuse model possesses first and second stability regions. For a fixed wall radius and an ideal wall, as the mean toroidal rotation increments,

IKM's growth rate increases and stability boundaries are pushed to lower beta values. In addition, in the resistive wall case, the low-beta tails corresponding to IPRWM's in static situations converge to the no-wall limit and rotation renders these scenarios slightly more unstable. In general, the qualitative character of IKM's and IPRWM's for a diffuse and solid body rotation profiles are similar. The one important difference between the diffuse and solid body rotation models is that the beta limits versus wall position stability curves are more strongly affected by the mean value of the flow ($\langle \Omega \rangle$) in the former case, which is clearly seen by comparing figures 3.1 and 3.5. Presumably, this difference is due to a global shear-flow drive present in the diffuse model only.

The previous stability analysis has been tailored to study a circular configuration, but it could be extended to accommodate non-circular cross-sections as well. Such analysis would be based on the analytic series-form solution for an elliptical or a D-shaped scenario, both of which were introduced in chapter 2.

Chapter 4

Summary

In this work, we have explored some characteristics of tokamak plasmas with flows. The analysis consists of a self-consistent construction of a high-beta equilibrium configuration with flows and a subsequent linear stability analysis of external modes.

In the equilibrium part, starting from the Grad-Shafranov-Bernoulli system, we have obtained a new family of high-beta MHD stationary axisymmetric states. Using a combination of a variational perturbative scheme in terms of the inverse aspect ratio, a boundary perturbation approach in terms of the triangularity and the Green's function method, we find a closed-form solution for a circular geometry and series solutions in terms of Mathieu functions for elliptical and D-shaped scenarios [93]. The analytical approximations account for diffuse rotation profiles in both the toroidal and poloidal directions and show excellent performance against the FLOW code [61]. In particular, we have shown that the poloidal flux solution in a circular geometry converges to Freidberg's static counterpart [16] by taking the appropriate limit and is characterized by a small number of intuitive parameters: the inverse aspect ratio, the mean magnetic shear, the kink safety factor, and the plasma beta. This economic, closed-form solution should be useful as the first step in stability analyses which aim to incorporate flow in a self-consistent way. The series solution for the elliptical and D-shaped cross-sections are able to accommodate realistic values for the elongation and triangularity. Furthermore, it should be possible to extend the boundary perturbation method to deal with configurations whose boundaries deviate slightly from an ellipse as, for example, diverted boundaries with a single or double X-point. Additionally, the solution for a D-shaped configuration could be used as

the starting point of stability analyses for scenarios with negative triangularity, a topic which is currently drawing attention [94, 95].

In regards to linear stability analyses including toroidal flow, generally, they either consider rigid rotation and are performed in an analytical (or semi-analytical) way or assume a more realistic, diffuse rotation scenario, and a full numerical approach is taken. Here, we have performed an analysis "in between" these two approaches: a semi-analytical stability study of a diffuse toroidal rotation profile. This approach is possible in view of the economic, analytic equilibrium solutions of the GSB system we have previously constructed. Although the current analysis is tailored for a circular cross-section, we could extend it to account for finite plasma shaping.

The stability analysis focuses on the effect a diffuse toroidal rotation profile has on the development of ideal-plasma-resistive-wall-modes (IPRWM's) and external ideal kink modes (IKM's). The analytical part of the problem is tackled in analogy to the sharp-boundary formalism with a solid body toroidal rotation developed in [60]. Matching conditions are expressed as a set of algebraic equations which incorporate a kink mode drive for instabilities and resistive wall effects, while pressure and shear-flow drives are captured at the eigenmode equation level. The solution method consists of a multidimensional shooting method for the coupled Fourier harmonics of the plasma displacement. Here, we take advantage of the matrix eigenvalue approach elaborated in [60] in order to obtain first guesses for the eigenvalues and eigenvectors.

In general, results indicate that the qualitative character of IKM's and IPRWM's in the presence of a diffuse or a solid body rotation are similar. A number of standard results from the literature are recovered for the diffuse model, indicating the plausibility of our approximations. In particular, wall position versus beta marginal curves show the presence of first and second stability regions. For increasing toroidal velocities of few percent the Alfvén frequency, IKM's growth rates increase while beta limits decrease. Additionally, the resistive tails, corresponding to IPRWM's, correctly converge to the static no-wall limit and second stability regions cease to exits when walls are resistive. On the other hand, the presence of both flow and resistivity render the plasma slightly more unstable than it would be in a static state, as indicated by the resistive tails growing below the no-wall limit when rotation is present. The main difference

between the diffuse and solid body rotation models is seen in wall position versus plasma beta marginal stability curves in the presence of an ideal wall, here, rotation has a stronger destabilizing effect in the former model. Specifically, at a given beta, if instabilities are to be suppressed by the ideal wall, an increase in the mean value of the toroidal rotation requires the wall to be significantly closer to the plasma in the diffuse case than in the solid body rotation scenario. Arguably, this difference is due to a global shear-flow drive effect.

Appendix A

Green's functions for the two-dimensional Helmholtz equation over circular and elliptical
geometries

We work with Green's functions which involve an expansion in a complete set of functions
for the angular variable and a piecewise function for the radial variable. For details on the
constructions of Green's function by this the method see, for example, [96, section 12.4]. The
Green's function have the generic form:

$$g\left(u, v | u', v'\right) = G \sum_{m=M}^{\infty} \frac{f_{1m}\left(u_<\right) f_{4m}\left(u_>\right)}{f_{1m}\left(u_o\right)} f_{3m}(v, v'), \qquad (A.1)$$

where u and v represent the radial and angular variables, respectively. $\left(u_<, u_>\right)$ refer to the
minimum or maximum between the point of observation u and the integration variable u', u_o
is the scaled radial variable at the boundary, G is a constant and $f_{4m}\left(u\right)$ is an antisymmetric
combination that ensures that the solution vanishes at the boundary:

$$f_{4m}\left(u, u_o\right) = f_{1m}(u_o)f_{2m}(u) - f_{1m}(u)f_{2m}(u_o). \qquad (A.2)$$

To construct the circular or elliptical Green's functions simply put together the terms in Table
A.1. The elliptical Green's function is actually a sum of two terms like Eq. (A.1). The two
types of $f_{4m}\left(u\right)$ functions for the elliptical case appear in the solution for the poloidal flux in
the elliptical and D-shaped cross sections, so they are given special names:

$$\mathrm{JNe}_m(\zeta, \Lambda) := \mathrm{Je}_m(\zeta_o, \Lambda)\mathrm{Ne}_m(\zeta, \Lambda) - \mathrm{Je}_m(\zeta, \Lambda)\mathrm{Ne}_m(\zeta_o, \Lambda), \qquad (A.3)$$

$$\text{JNo}_m(\zeta, \Lambda) := \text{Jo}_m(\zeta_o, \Lambda)\text{No}_m(\zeta, \Lambda) - \text{Jo}_m(\zeta, \Lambda)\text{No}_m(\zeta_o, \Lambda). \tag{A.4}$$

Type	u_o	G	M	f_1	f_2	f_3
Circle ($\lambda > 0$)	1	$1/4$	$-\infty$	$\text{J}_m\left(\sqrt{\lambda}\,r\right)$	$\text{N}_m\left(\sqrt{\lambda}\,r\right)$	$\cos\left(m(\theta - \theta')\right)$
Circle ($\lambda < 0$)	1	$-1/(2\pi)$	$-\infty$	$\text{I}_m\left(\sqrt{|\lambda|}\,r\right)$	$\text{K}_m\left(\sqrt{|\lambda|}\,r\right)$	$\cos\left(m(\theta - \theta')\right)$
Ellipse	ζ_o	$1/2$	0	$\text{Je}_m(\zeta, \Lambda)$	$\text{Ne}_m(\zeta, \Lambda)$	$\text{ce}_m(\eta, \Lambda)\,\text{ce}_m(\eta', \Lambda)$
($\Lambda > 0$)	ζ_o	$1/2$	1	$\text{Jo}_m(\zeta, \Lambda)$	$\text{No}_m(\zeta, \Lambda)$	$\text{se}_m(\eta, \Lambda)\,\text{se}_m(\eta', \Lambda)$
Ellipse	ζ_o	$-1/\pi$	0	$\text{Ie}_m(\zeta, \Lambda)$	$\text{Ke}_m(\zeta, \Lambda)$	$\text{ce}_m(\eta, \Lambda)\,\text{ce}_m(\eta', \Lambda)$
($\Lambda < 0$)	ζ_o	$-1/\pi$	1	$\text{Io}_m(\zeta, \Lambda)$	$\text{Ko}_m(\zeta, \Lambda)$	$\text{se}_m(\eta, \Lambda)\,\text{se}_m(\eta', \Lambda)$

Table A.1: For the 2D Helmholtz equation defined over circular and elliptical domains, Green's functions which involve an expansion in a complete set of functions for the angular variable and a piecewise function for the radial variable are constructed using the expressions from this table.

Amplitude$_m$	Radial$_m$	Integrand$_m$	Angular$_m$
κ	$A'_{2m}(\zeta_o, \Lambda)$	$\overline{\delta x}_2 \sin(\eta) J^{-1}(\zeta_o, \eta)$	$\text{ce}_{2m}(\eta, \Lambda)$
$-\overline{f}^2\kappa/2$	$A'_{2m}(\zeta_o, \Lambda)$	$\overline{\delta x}_1^2 \cos(\eta) \sin(\eta) \sin(2\eta) J^{-3}(\zeta_o, \eta)$	$\text{ce}_{2m}(\eta, \Lambda)$
$-\kappa^3$	$A'_{2m}(\zeta_o, \Lambda)$	$\overline{\delta x}_1^2 \sin^2(\eta) J^{-3}(\zeta_o, \eta)$	$\text{ce}_{2m}(\eta, \Lambda)$
$\kappa/2$	$A'_{2m}(\zeta_o, \Lambda)$	$\overline{\delta x}_1^2 J^{-2}(\zeta_o, \eta)$	$\text{ce}_{2m}(\eta, \Lambda)$
$\kappa^2/2$	$A''_{2m}(\zeta_o, \Lambda)$	$\overline{\delta x}_1^2 \sin^2(\eta) J^{-2}(\zeta_o, \eta)$	$\text{ce}_{2m}(\eta, \Lambda)$
κ	$A'_{2m}(\zeta_o, \Lambda)$	$\overline{\delta x}_1^2 \cos(\eta) \sin(\eta) J^{-2}(\zeta_o, \eta)$	$\text{ce}'_{2m}(\eta, \Lambda)$
κ	$A^{(1)}_{m+1}(\Lambda)\text{Jo}'_{m+1}(\zeta_o, \Lambda)$	$\overline{\delta x}_1 \sin(\eta) J^{-1}(\zeta_o, \eta)$	$\text{se}_{m+1}(\eta, \Lambda)$
1	$A^{(1)}_{m+1}(\Lambda)\text{Jo}_{m+1}(\zeta_o, \Lambda)$	$\overline{\delta x}_1 \cos(\eta) J^{-1}(\zeta_o, \eta)$	$\text{se}'_{m+1}(\eta, \Lambda)$

Table A.2: Building blocks to construct the $C^{(2)}_{nm}(\Lambda)$ coefficients for the D-shaped solution. To compute the $A^{(2)}_{nm}(\Lambda)$ coefficients it is necessary to make the replacements $A_{2m}(\zeta_o, \Lambda) \to C_{2m+1}(\zeta_o, \Lambda)$, $A^{(1)}_{m+1}(\Lambda) \to C^{(1)}_m(\Lambda)$ and $\text{Jo}_{m+1}(\zeta_o, \Lambda) \to \text{Je}_m(\zeta_o, \Lambda)$ in the Radial$_m$ functions and both $\text{ce}_{2m}(\eta, \Lambda) \to \text{se}_{2m+1}(\eta, \Lambda)$ and $\text{se}_{m+1}(\eta, \Lambda) \to \text{ce}_m(\eta, \Lambda)$ in the Angular$_m$ terms.

Green's functions which involve an expansion in a complete set of functions for both the angular radial variables can be also constructed. For a generic method to construct such Green's functions see [97, section 7.3.3-2].

Appendix B

Fourier decomposition of angular Mathieu functions

The Fourier coefficients of the Mathieu functions of integral order are [78]:

$$D_0^{2m}(\Lambda) := \frac{1}{2\pi} \int_0^{2\pi} \mathrm{ce}_{2m}\left(\eta, \Lambda\right) d\eta, \tag{B.1}$$

$$D_{2r}^{2m}(\Lambda) := \frac{1}{\pi} \int_0^{2\pi} \mathrm{ce}_{2m}\left(\eta, \Lambda\right) \cos(2r\eta) d\eta, r \neq 0, \tag{B.2}$$

$$D_{2r+1}^{2m+1}(\Lambda) := \frac{1}{\pi} \int_0^{2\pi} \mathrm{ce}_{2m+1}\left(\eta, \Lambda\right) \cos((2r+1)\eta) d\eta, \tag{B.3}$$

$$B_{2r+1}^{2m+1}(\Lambda) := \frac{1}{\pi} \int_0^{2\pi} \mathrm{se}_{2m+1}\left(\eta, \Lambda\right) \sin((2r+1)\eta) d\eta, \tag{B.4}$$

$$B_{2r+2}^{2m+2}(\Lambda) := \frac{1}{\pi} \int_0^{2\pi} \mathrm{se}_{2m+2}\left(\eta, \Lambda\right) \sin((2r+2)\eta) d\eta, \tag{B.5}$$

where $m, r = 0, 1, 2, \ldots$.

Appendix C

D-shaped first- and second-order corrections

Integrating the $O(\alpha)$-inhomogeneity in Eq. (2.75) with the aid of the previously constructed elliptical Green's functions we obtain the coefficients $C_n^{(1)}(\Lambda)$ and $A_n^{(1)}(\Lambda)$:

$$
\begin{Bmatrix} C_n^{(1)}(\Lambda) \\ A_n^{(1)}(\Lambda) \end{Bmatrix} = -\frac{\overline{f}\cosh(\zeta_o)}{\pi} \begin{Bmatrix} \mathrm{Je}_n^{-1}(\zeta_o,\Lambda) \\ \mathrm{Jo}_n^{-1}(\zeta_o,\Lambda) \end{Bmatrix} \sum_{m=0}^{\infty} \begin{Bmatrix} C'_{2m+1}(\zeta_o,\Lambda) \\ A'_{2m}(\zeta_o,\Lambda) \end{Bmatrix}
$$
$$
\times \int_0^{2\pi} d\eta' \frac{\overline{\delta x_1}\,\sin(\eta')}{J(\zeta_o,\eta')} \begin{Bmatrix} \mathrm{se}_{2m+1}(\eta',\Lambda)\mathrm{ce}_n(\eta',\Lambda) \\ \mathrm{ce}_{2m}(\eta',\Lambda)\mathrm{se}_n(\eta',\Lambda) \end{Bmatrix},
\tag{C.1}
$$

where radial derivatives of $C_m(\zeta,\Lambda)$ and $A_m(\zeta,\Lambda)$, evaluated at the elliptical boundary, are:

$$
A'_m(\zeta_o,\Lambda) = \frac{A\overline{f}^2}{2\mathrm{Je}_m(\zeta_o,\Lambda)} \int_0^{\zeta_o} \mathrm{Je}_m(\zeta',\Lambda)\mathrm{KA}_m(\zeta',\Lambda)d\zeta',
\tag{C.2}
$$

$$
C'_m(\zeta_o,\Lambda) = \frac{C\overline{f}^3}{2\mathrm{Jo}_m(\zeta_o,\Lambda)} \int_0^{\zeta_o} \mathrm{Jo}_m(\zeta',\Lambda)\mathrm{KC}_m(\zeta',\Lambda)d\zeta'.
\tag{C.3}
$$

It is also useful to evaluate the second derivatives:

$$
A''_m(\zeta_o,\Lambda) = \frac{A\overline{f}^2}{2}\mathrm{KA}_m(\zeta_o,\Lambda),
\tag{C.4}
$$

$$
C''_m(\zeta_o,\Lambda) = \frac{C\overline{f}^3}{2}\mathrm{KC}_m(\zeta_o,\Lambda).
\tag{C.5}
$$

$J(\zeta, \eta)$ is the Jacobian of the elliptical change of coordinates defined in Eqs. (2.52)-(2.53):

$$J(\zeta, \eta) := \frac{\overline{f}^2}{2} \left(\cosh(2\zeta) - \cos(2\eta) \right). \tag{C.6}$$

From the $O(\alpha^2)$-inhomogeneity in Eq. (2.76) we get the second-order coefficients $C_n^{(2)}(\Lambda)$ and $A_n^{(2)}(\Lambda)$. Each coefficient is given by a sum:

$$C_n^{(2)}(\Lambda) = \sum_m C_{nm}^{(2)}(\Lambda), \tag{C.7}$$

$$A_n^{(2)}(\Lambda) = \sum_m A_{nm}^{(2)}(\Lambda), \tag{C.8}$$

$C_{nm}^{(2)}(\Lambda)$ and $A_{nm}^{(2)}(\Lambda)$ are computed substituting the elements of Table A.2 in the expression:

$$
\begin{Bmatrix} C_{nm}^{(2)}(\Lambda) \\ A_{nm}^{(2)}(\Lambda) \end{Bmatrix} = -\frac{Amplitude_m}{\pi} \begin{Bmatrix} \mathrm{Je}_n^{-1}(\zeta_o, \Lambda) \\ \mathrm{Jo}_n^{-1}(\zeta_o, \Lambda) \end{Bmatrix} \sum_{m=0}^{\infty} \left[Radial_m \right]
$$
$$
\times \int_0^{2\pi} d\eta' Integrand_m(\eta') \, Angular_m(\eta') \begin{Bmatrix} \mathrm{ce}_n(\eta', \Lambda) \\ \mathrm{se}_n(\eta', \Lambda) \end{Bmatrix}. \tag{C.9}
$$

Appendix D

Extension of the single-fluid equilibrium to compute the two-fluid velocity component normal
to magnetic surfaces

In this appendix, we consider an extension of the single-fluid ideal MHD model, constructed in chapter 2, to deal with two-fluid effects. Specifically, we estimate the two-fluid component of the velocity which is perpendicular to magnetic surfaces. In the context of axisymmetric equilibrium scenarios, a single-fluid MHD description guarantees that streamlines are tangent to magnetic surfaces (Eq. 1.22). Yet, in a two-fluid description, where a distinction between electrons and ions is made, this constraint disappears. Since the electron mass is negligible as compared to the ion mass, the macroscopic flow is governed by the velocity of the ions. Therefore, while electrons are, to a good approximation, still constrained to move on magnetic surfaces, ions finite inertia "pushes" streamlines away from magnetic surfaces.

Two-fluid axisymmetric scenarios have been studied by several authors [98, 99, 100, 101, 102, 103]. These analyses are analogous to the one presented in chapter 2, where the Grad-Shafranov and Bernoulli equations were introduced. Two-fluid axisymmetric scenarios are also determined by a set of free functions, which must be specified from the outset. As expected, the single-fluid formalism can be recovered from the two-fluid one by an appropriate limiting procedure [102, 67].

As pointed out in [67], the interest in computing the two-fluid component of the velocity which is normal to magnetic surfaces originates from the possible effect this component has on the linear properties of unstable modes localized on magnetic resonant surfaces. Here, we provide a simple estimation of this component based on the single-fluid, closed-form solution given by Eqs. 2.34-2.36, for a tokamak with a circular cross-section.

Let Ψ^{tf} and $\boldsymbol{V}$ be the poloidal flux and ion velocity, as determined by two-fluid theory, respectively. The component of the velocity normal to magnetic surfaces is given by

$$V_\psi \equiv \boldsymbol{V} \cdot \frac{\nabla \Psi^{tf}}{|\nabla \Psi^{tf}|}. \tag{D.1}$$

Now, in the reduced massless electrons case, the two-fluid ion velocity is given by

$$\boldsymbol{V} = \frac{\phi^{tf}(\Psi_i)}{n} \nabla \Psi_i \times \nabla \varphi + V_\varphi \hat{\boldsymbol{e}}_\varphi, \tag{D.2}$$

where Ψ_i is a stream function for the ions, n is the plasma number density, and ϕ^{tf} is a free function analogous to the single-fluid one (Φ). We recall that the right-handed coordinate systems (R, φ, Z) and (r, φ, θ) have been introduced in section 1.2.1. In this model, the poloidal flux and the ion velocity stream function are related by

$$\Psi_i = \Psi^{tf} + \frac{m_i R V_\varphi}{e}, \tag{D.3}$$

where m_i and e correspond, respectively, to the mass and charge of the ions constituting the plasma. For typical experimental values in confinement devices it turns out that

$$\delta \Psi \equiv \frac{m_i R V_\varphi}{e} << \Psi^{tf}, \tag{D.4}$$

that is to say, in practice, two-fluid flux surfaces and stream surfaces differ by a quantity which is small.

Figure D.1 illustrates, for a rotating deuterium plasma in a configuration with an inverse aspect ratio $\epsilon = 0.25$, single- and two-fluid magnetic flux surfaces. They were computed by means of the single- and two-fluid codes FLOW [61] and FLOW2 [67], respectively. This figure also shows contours corresponding to the analytical, single-fluid solution, as computed by Eqs. 2.34-2.36. Continuing, it is clear that single- and two-fluid flux surfaces differ from each other, and that the difference increases as the magnetic axis is approached. However, for our purposes, we will regard them as being identical. This approximation, together with the
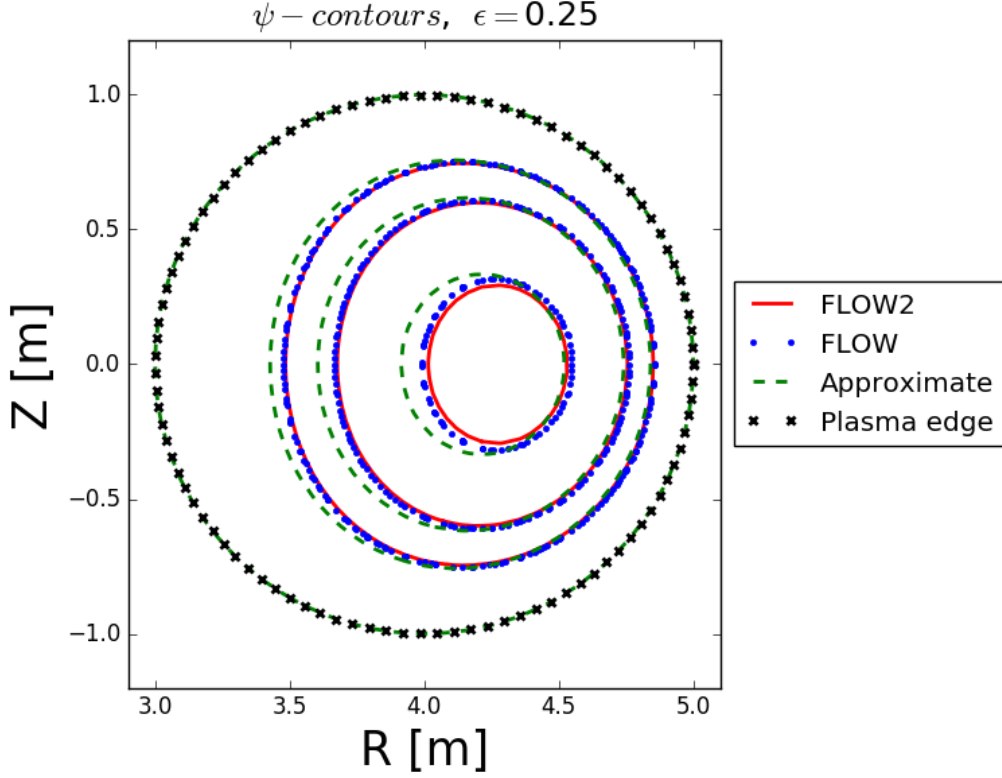
Figure D.1: Magnetic surfaces in a circular configuration computed using FLOW2 (two-fluid code), FLOW (single-fluid code) and an analytical approximation. We are assuming a deuterium plasma with a mass $m_i = 3.34 \times 10^{-27} kg$.

smallness of the term in D.4, allow us to express the normal component of the velocity as

$$V_\psi = -\frac{2m_i\Phi(\psi)\Omega(\psi)}{\sqrt{\mu_o}e\rho(\psi)\left[1 - \Phi^2(\psi)/\rho(\psi)\right]}\frac{\boldsymbol{B}_p}{B_p} \cdot \hat{\boldsymbol{e}}_R + O(\delta\Psi), \tag{D.5}$$

all quantities being single-fluid ones. In particular, ψ is given by Eqs. 2.34-2.36. An alternative expression is

$$V_\psi = \frac{2m_i\Phi(\psi)\Omega(\psi)}{\sqrt{\mu_o}e\rho(\psi)\left[1 - \Phi^2(\psi)/\rho(\psi)\right]}\frac{1}{\sqrt{r^2\left(\frac{\partial\psi}{\partial r}\right)^2 + \left(\frac{\partial\psi}{\partial\theta}\right)^2}}\left(r\sin\theta\frac{\partial\psi}{\partial r} + \cos\theta\frac{\partial\psi}{\partial\theta}\right). \tag{D.6}$$

Figure D.2 illustrates both the analytical approximation and FLOW2 results for V_ψ as a function of the angular variable θ. The curves shown there correspond to the magnetic surfaces illustrated in figure D.1.
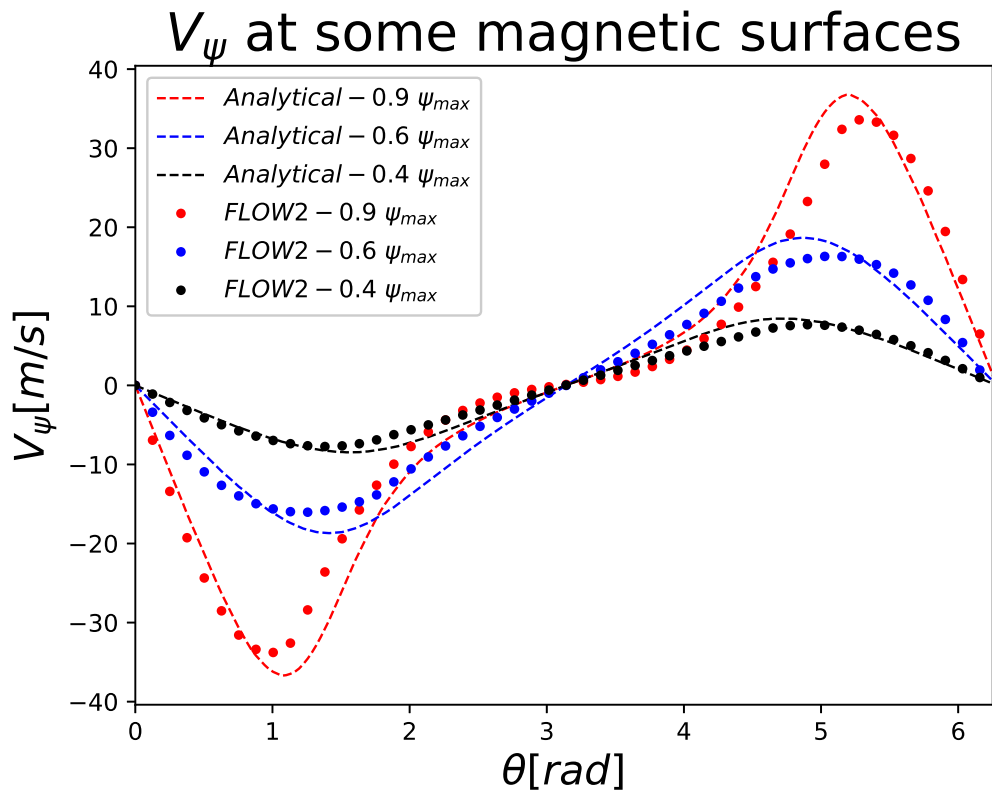
Figure D.2: FLOW2 and analytical approximation calculations for the normal component of the ion velocity at several magnetic surfaces. They correspond to the same magnetic surfaces shown in figure D.1.

Appendix E

A comment on Chandrasekhar's classical solution for the Kelvin-Helmholtz instability
employing the Spectral-Web-Method

Among the MHD instabilities in the presence of background flow, the one caused by gradients in the velocity profile is referred to as the Kelvin-Helmholtz instability (KH). In truth, this instability has a hydrodynamic origin [104, 105]. In an MHD context, the problem is to understand the interplay between the flow-shear and the magnetic field. In regards to magnetic confinement fusion, the KH instability might become important in future spherical tokamaks, having larger velocity gradients than the ones present in current experiments [106]. In any case, an understanding of the KH instability is important since it illustrates a destabilizing mechanism static scenarios do not possess.

A classical treatment on the KH instability in the presence of a background magnetic field is due to Chandrasekhar [62]. From his formalism, the main conclusion is that magnetic field lines are able to provide stabilization against a sheared-background flow. Naturally, the relative direction between the magnetic and flow fields matters, and the stabilizing effect of the former is most pronounced when it is aligned with the latter. Chandrasekhar's derivation is a slab-geometry case study, where a discontinuous; but otherwise constant, background velocity profile acts as the source of free energy, and a constant magnetic field in the streaming direction provides a surface tension-like suppression mechanism. Interestingly, the equilibrium situation considered by Chandrasekhar is not a self-consistent MHD equilibrium.

Goedbloed has studied some aspects of the KH instability by employing the Spectral-Web method [107]. In this short appendix, we consider an exact MHD equilibrium consisting of

a continuous, sheared-velocity profile which we use to recover Chandrasekhar's results in the infinite shear limit, and employ Spectral-Web method as a visualization aid.

E.1 The Spectral-Web-Method

The Spectral-Web-Method was introduced by J. P. Goedbloed over a series of papers [108, 107, 109, 110] as a way to exploit the self-adjointness nature of the eigenvalue problem 1.31. The result is a "connecting structure" (the Spectral-Web) in the complex plane along which the eigenvalues of the system are distributed. Since this method is not widely used in the community we provide a description. The interested reader should refer to the original papers to get the full picture.

The construction of the Spectral-Web starts from recasting the problem at hand. It is convenient to decompose the quadratic form associated with the potential energy in two contributions:

$$W[\boldsymbol{\xi}] = W_{plasma}[\boldsymbol{\xi}] + W_{boundary}[\boldsymbol{\xi}].$$ (E.1)

The first contribution is an integral over the plasma volume and it can be shown to be self-adjoint by a direct calculation [45, 47], which should be the case since there is no mechanism through which an ideal MHD plasma could dissipate energy. The second contribution corresponds to the energy gained or lost at the plasma boundary (∂V).

$$W_{boundary}[\boldsymbol{\xi}] = -\frac{1}{2} \int_{\partial V} \xi_n [[\widetilde{P}(\boldsymbol{\xi})]] dA,$$ (E.2)

where $\widetilde{P}$ is the perturbed total pressure of the system (as defined by Eq. 1.35) and dA is an element of area. Evidently, under the boundary conditions for internal modes 1.34 or for external modes 1.36-1.37, the energy interchange term E.2 vanishes. The eigenvalue problem 1.31 can then be cast as

$$I[\boldsymbol{\xi}]\omega^2 - V[\boldsymbol{\xi}]\omega - W_{plasma}[\boldsymbol{\xi}] = W_{boundary}[\boldsymbol{\xi}].$$ (E.3)

We now assume that neither the boundary condition for internal modes 1.34 nor for external modes 1.36-1.37 are satisfied. That is, we let the boundary conditions unspecified. As discussed before, changing the boundary conditions destroys the self-adjointness nature of the operators in the general case; however, a direct calculation shows that the Doppler-Coriolis operator is independent of boundary conditions, so it remains self-adjoint. The end result of "opening up the boundaries" is that the RHS of Eq. E.3 is not zero anymore.

To finish up the description of the Spectral-Web we assume a one-dimensional system. The associated eigenmode equation is typically a second order homogeneous ordinary differential equation (ODE). To begin with, we impose the correct left boundary condition (like $\xi|_{r=0} = 0$) but we open up the right boundary. For a given value of ω this equation could be solved if $\xi'|_{r=0}$ was specified as well. However, since the ODE in question has been assumed to be homogeneous we can set this derivative as any finite value without loss of generality. We can then carry out the integration (numerically) and evaluate the boundary term defined by Eq. E.2, which, for the one-dimensional system under consideration, has the simpler form

$$W^{1-D}_{boundary}[\xi(a)] = -\frac{1}{2}\xi(a)[[\widetilde{P}(\xi(a))]], \tag{E.4}$$

where $r = a$ corresponds to the right boundary. If we happen to pick an ω for which Eq. E.4 vanishes then, by definition, that would correspond to have found an eigenvalue of either the fixed or the free boundary value problem, which could then be easily discriminated by direct evaluation of the plasma and total pressure perturbations. The locus of ω's for which the real part of E.4 vanishes is named "solution path", likewise, the curve defined by setting the imaginary part of E.4 equal to zero is the "conjugate path". The intersection of these curves occurs at the eigenvalues of the system. The resulting structure in the complex plane constitutes the Spectral-Web.

The Spectral-Web has been constructed from the requirement of no energy interchange at the plasma boundary. But the importance of this connecting structure lies in the fact that it leads to real and complex oscillations theorems [108] which generalize the static theorems of node counting to the stationary case. Pragmatically, all we have done is to consider Eq. E.4

as a target function and compute the contour levels $\mathbb{Re}\{W_{boundary}\} = 0$ and $\mathbb{Im}\{W_{boundary}\} = 0$. Certainly, for the purposes of determining the eigenvalues, we can come up with other alternatives such as:

$$W_{target,1} = \xi(a), \tag{E.5}$$

$$W_{target,2} = [[\widetilde{P}(\xi(a))]], \tag{E.6}$$

and so on. But the oscillations theorems would not apply in curves defined by these target functions. There are also arguments of improved numerical accuracy when looking for eigenvalues along the solution and conjugate paths [108]. We will mainly employ the Web-Spectrum as a visualization tool, so we do not dwell on these important results.

E.2 Obtaining the eigenmode equation

Chandrasekhar's starting point is the set of MHD equations 1.12-1.18, but where the closure equation 1.14 is replaced by the incompressibility condition:

$$\nabla \cdot \boldsymbol{u} = 0. \tag{E.7}$$

The stationary configuration of interest being

$$\boldsymbol{u}_0(\boldsymbol{r}) = u_{0z}(x)\hat{\boldsymbol{e}}_z, \tag{E.8}$$

$$\boldsymbol{B}_0(\boldsymbol{r}) = B_{0z}\hat{\boldsymbol{e}}_z, \tag{E.9}$$

$$\rho_0(\boldsymbol{r}) = \rho_0(x), \tag{E.10}$$

$$p_0(\boldsymbol{r}) = p_0(x), \tag{E.11}$$

which corresponds to a constant magnetic field in the direction of streaming, with an equilibrium velocity varying in the x-direction. For the stability analysis, perturbed quantities ($\widetilde{Q}$) are Fourier-analyzed in the ignorable coordinates and in time in the usual way:

$$\widetilde{Q}(x,y,z,t) = \widetilde{Q}(x)e^{i(k_z z + k_y y - \omega t)}, \tag{E.12}$$

so that if $\mathbb{Im}\{\omega\} > 0$ the equilibrium configuration is unstable. After straightforward algebra, Chandrasekhar reduced the stability problem to an eigenmode equation, which we write in terms of the perturbed x-component of the velocity ($\widetilde{u}_x$) and magnetic field ($\widetilde{B}_x$) as:

$$
\frac{d}{dx}\left[\rho_0\left(k_z u_{0z} - \omega\right)\frac{d\widetilde{u}_x}{dx} - k_z \rho_0 \widetilde{u}_x \frac{du_{0z}}{dx}\right]
$$
$$
- k^2 \rho_0 \left(k_z u_{0z} - \omega\right)\widetilde{u}_x - \frac{k_z B_{0z}}{\mu_o}\left[\frac{d^2 \widetilde{B}_x}{dx^2} - k^2 \widetilde{B}_x\right] = 0,
\tag{E.13}
$$

where

$$
\widetilde{B}_x = \frac{k_z B_{0z}}{k_z u_{0z} - \omega}\widetilde{u}_x,
\tag{E.14}
$$

and

$$
k^2 \equiv k_z^2 + k_y^2.
\tag{E.15}
$$

No other assumption has been used to obtain this eigenmode equation. In particular, no assumption has been made in regards to the actual form of the profile $u_{0z}(x)$ so far.

E.3   Boundary conditions: a tight plasma due to incompressibility

Given an arbitrary open surface, it is a standard exercise to show that the following boundary conditions hold for an incompressible plasma:

$$
[[\rho]] = 0,
\tag{E.16}
$$

$$
\left[\left[p + \frac{B_t^2}{2\mu_o}\right]\right] = 0,
\tag{E.17}
$$

$$
\rho u_n [[\boldsymbol{u}_t]] - \frac{B_n}{\mu_o}[[\boldsymbol{B}_t]] = \boldsymbol{0},
\tag{E.18}
$$

$$
B_n [[\boldsymbol{u}_t]] - u_n [[\boldsymbol{B}_t]] = \boldsymbol{0},
\tag{E.19}
$$

$$[[u_n]] = 0, \tag{E.20}$$

where n and t refer to the normal and tangential components of a given field with respect to the surface under consideration. It is then easily seen that

$$\left(\rho u_n^2 - \frac{B_n^2}{\mu_o} \right) [[\boldsymbol{B}_t]] = \boldsymbol{0}, \tag{E.21}$$

so, unless the open surface is locally moving at the Alfvén-like velocity determined by the normal component of the magnetic field at that locality, the tangential component of the magnetic field is continuous:

$$\text{if} \quad u_n \neq \frac{B_n}{\sqrt{\mu_o \rho}} \implies [[\boldsymbol{B}_t]] = \boldsymbol{0}, \tag{E.22}$$

which immediately implies

$$[[\boldsymbol{u}_t]] = \boldsymbol{0}, \tag{E.23}$$

and

$$[[p]] = 0. \tag{E.24}$$

The "tightness" of the configuration is due to the incompressibility condition, in the sense that it is the first equation one thinks of modifying when trying to loosen up the system, though there are other ways to accomplish this: including two-fluid corrections in the momentum equation or Ohm's law, etc.

E.3.1 Chandrasekhar's approximation: a discontinuous change of the velocity

A slightly simpler configuration than the one considered by Chandrasekhar is the case in which there is a discontinuous jump in the velocity profile at the plane $x = 0$ [62, pp. 508-511]:

$$u_{0z}(x) = u_o \;\; \text{if} \;\; x > 0 \;\; \text{and} \;\; u_{0z}(x) = -u_o \;\; \text{if} \;\; x < 0, \tag{E.25}$$

and both the equilibrium density and pressure are regarded as constants:

$$\rho_0(x) = \rho_o \ \text{ and } \ p_0(x) = p_o. \tag{E.26}$$

It should be recognized that this situation is in contradiction with the previously derived boundary condition in Eq. E.23 and it is not an MHD equilibrium. In any case, by integrating the governing Eq. E.13 from $x = -\epsilon$ to $x = +\epsilon$, and then taking the limit $\epsilon \to 0$ we obtain:

$$\left[\left[\rho_o\left(k_z u_{0z}(x) - \omega\right)\frac{d\widetilde{u}_x}{dx}\right]\right]_{x=0} - \frac{k_z^2 B_{0z}^2}{\mu_o}\left[\left[\frac{1}{k_z u_{0z}(x) - \omega}\frac{d\widetilde{u}_x}{dx}\right]\right]_{x=0} = 0, \tag{E.27}$$

where we have imposed the continuity condition:

$$\left[\left[\frac{\widetilde{u}_x(x)}{k_z u_{0z}(x) - \omega}\right]\right] = 0, \tag{E.28}$$

at the interface. There are two equally compelling ways to think about this equation. One way is to notice that the normal component of the magnetic field in equation E.14 should be continuous:

$$[[\widetilde{B}_x]] = 0. \tag{E.29}$$

Alternatively, it is possible to consider an equation for the plasma displacement (δx):

$$\frac{\partial}{\partial t}\delta x + u_{0z}\frac{\partial}{\partial z}\delta x = \widetilde{u}_x, \tag{E.30}$$

from which, after a decomposition into normal modes, the condition under discussion follows:

$$[[\delta x]] = \left[\left[\frac{\widetilde{u}_x(x)}{k_z u_{0z}(x) - \omega}\right]\right] = 0. \tag{E.31}$$

The point here is that the Eulerian variable ($\widetilde{u}_x$) is discontinuous but the Lagrangian one δx is not. Continuing, the solution for the perturbed velocity in the two regions can be written as

$$u_{1x}(x) = A_1 \exp(-kx) \ \text{if} \ x > 0 \ \text{and} \ u_{1x}(x) = A_2 \exp(kx) \ \text{if} \ x < 0, \tag{E.32}$$

where A_1 and A_2 are some as of yet undetermined coefficients. Moreover, we have set the velocity at infinity equal to zero. Applying the boundary conditions in Eqs. E.27 and E.28 we obtain a system of two equations in two unknowns and, by setting the determinant of the associated matrix equal to zero, we obtain the dispersion relation

$$\omega = \pm k_z \sqrt{\frac{B_{0z}^2}{\mu_o \rho_o} - u_o^2} = \pm k_z \sqrt{V_a^2 - u_o^2}, \tag{E.33}$$

where the Alfvén speed is $V_a = B_{0z}/\sqrt{\mu_o \rho_o}$. That is to say, if the jump in the velocity across the plane of discontinuity is sufficiently large, the configuration is unstable. Clearly, the magnetic field acts in a stabilizing way.

E.4   Recovering Chandrasekhar's solution as a strong shear limiting case

As an alternative way to derive Chandrasekhar's dispersion relation, we consider the exact MHD equilibrium defined by the continuous velocity profile

$$u_{0z} = \sqrt{5} V_A \tanh\left[\tau \left(x - \frac{1}{2}\right)\right], \tag{E.34}$$

where τ is a velocity-shear parameter. As illustrated in figure E.1a, the velocity profile develops an increasingly abrupt transition as τ increases. In the limit of τ being infinitely large we obtain

$$u_{0z}(x) = \sqrt{5} V_A \ \text{if} \ x > 0 \ \text{and} \ u_{0z}(x) = -\sqrt{5} V_A \ \text{if} \ x < 0, \tag{E.35}$$

that is, this profile mimics Chandrasekhar's discontinuous velocity profile. After straightforward algebra, it is possible to derive an eigenmode equation for the Lagrangian plasma displacement (ξ_x):

$$\frac{d}{dx}\left[\left[x^3\left(\overline{\omega}^2 - \omega_A^2\right)\right]\frac{d\xi_x}{dx}\right] - k_z^2\left[\left(\overline{\omega}^2 - \omega_A^2\right)\right]\xi_x = 0, \tag{E.36}$$

where the Doppler-shifted frequency ($\overline{\omega}$) is given by

$$\overline{\omega}(x) \equiv \omega - k_z u_{0z}(x), \tag{E.37}$$

and the Alfvén frequency is defined in this context as

$$\omega_A \equiv k_z V_A. \tag{E.38}$$

In regards to the Spectral-Web, consider figure E.2. The meaning of the solution and conjugate paths has been explained in section E.1. Due to the symmetric way in which the plasma displacement and the pressure perturbation appear in equation E.4, the points of intersection of these paths correspond either to the actual eigenvalues of the system ("true eigenvalues") or to points where the pressure perturbation vanishes at the right boundary ("false eigenvalues"). In particular, figure E.2b, which corresponds to a strongly sheared scenario, has as its eigenvalues

$$\omega \approx 2V_A k_z i,$$

which is consistent with Chandrasekhar's dispersion relation Eq. E.33. Finally, figures E.3 and E.4 illustrate real and false eigenmodes, respectively. A distinctive feature of a KH instability is the localization of the eigenmode around the point of maximum velocity shear.
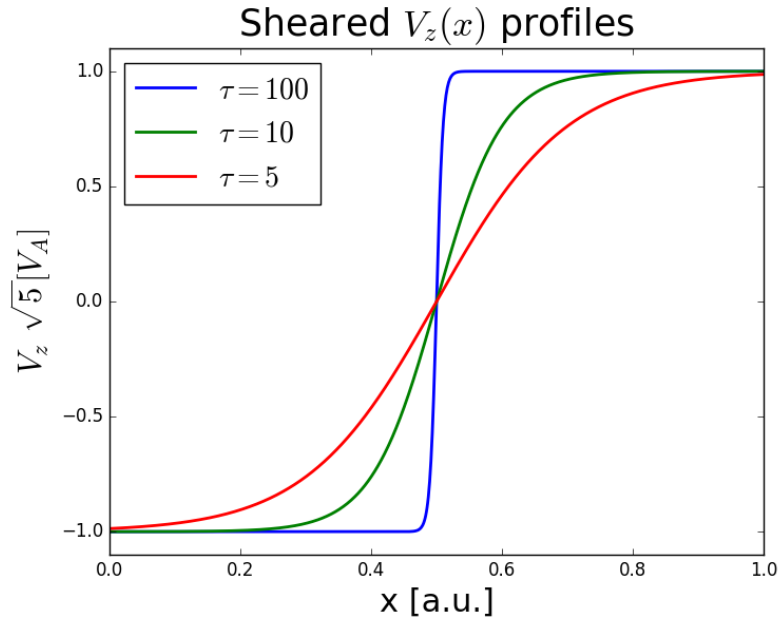
(a) Sheared velocity profile.
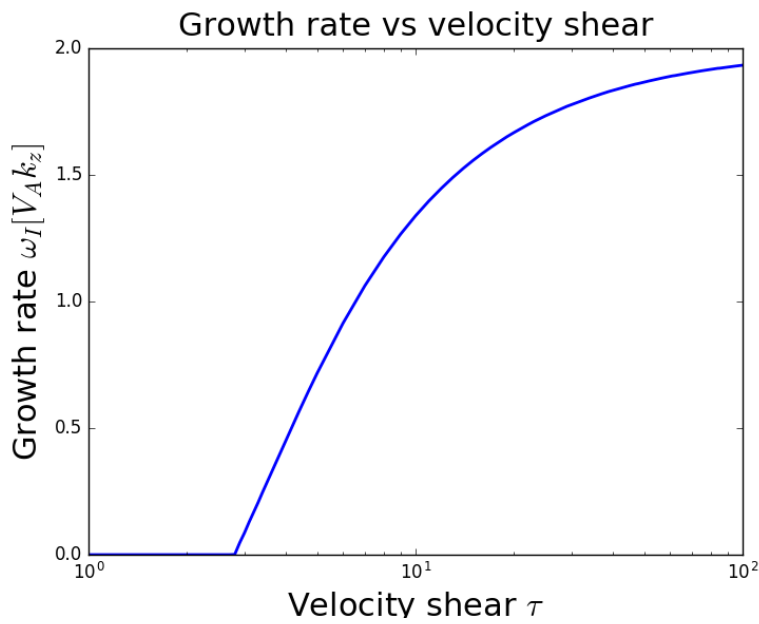
(b) Marginal stability occurs at $\tau = 2.8$.

Figure E.1: Sheared-velocity profile. (a) Sheared-velocity profile as given by Eq. E.34, (b) Growth rate as a function of the velocity-shear parameter (τ).

(a) Spectral-Web for $\tau = 5$.

(b) Spectral-Web in Chandrasekar's limit.
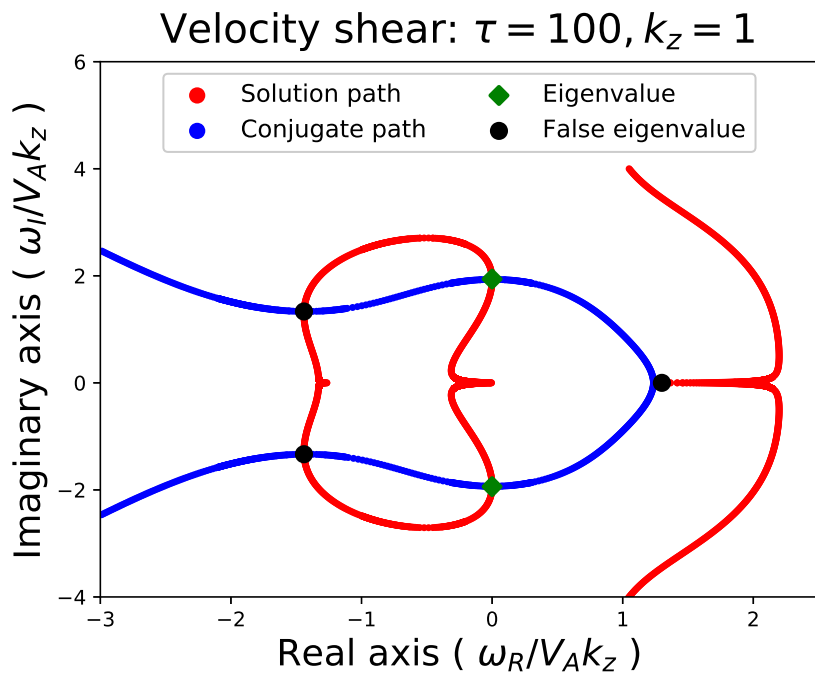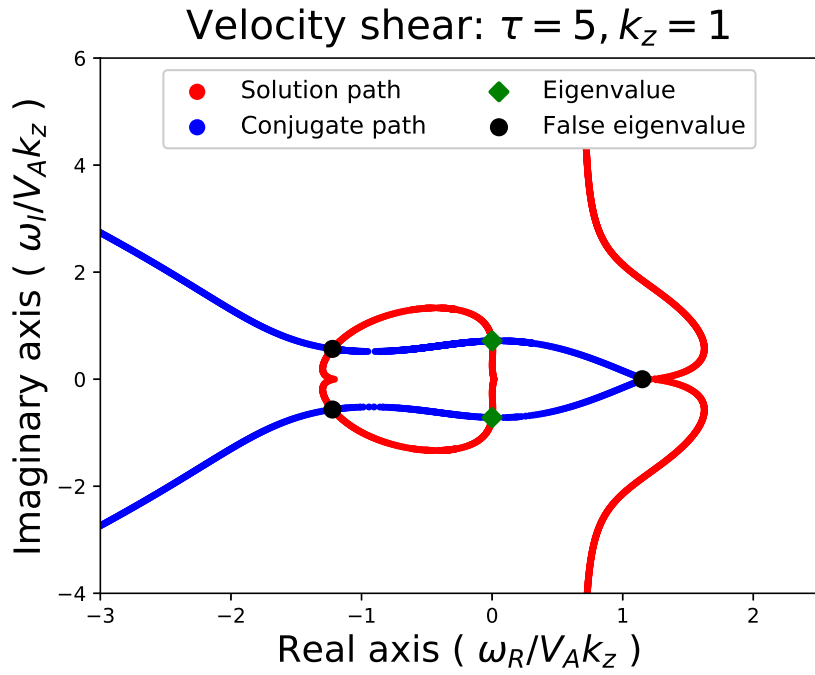
Figure E.2: Spectral-Webs. (a) Spectral-Web for $\tau = 5$, (b) Spectral-Web for $\tau = 100$, which "effectively" corresponds to Chandrasekhar's situation.
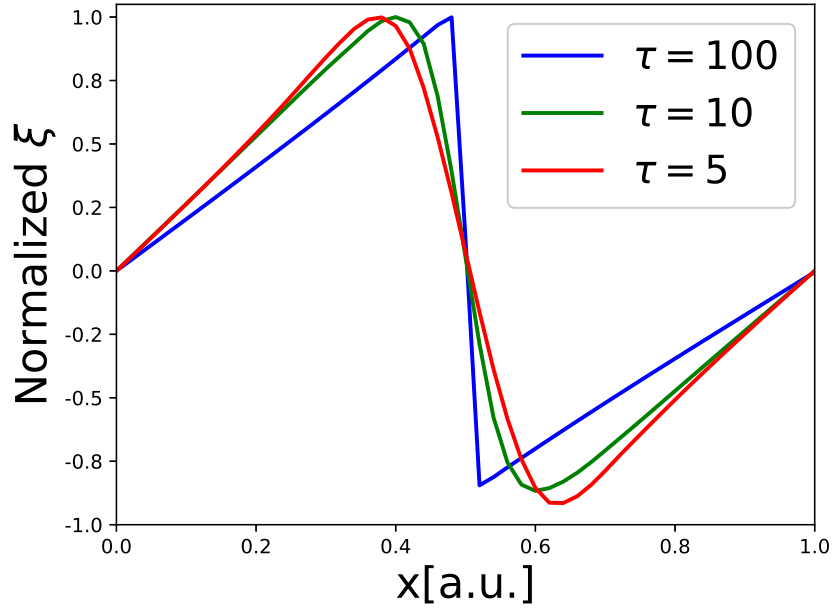
(a) Plasma displacement.
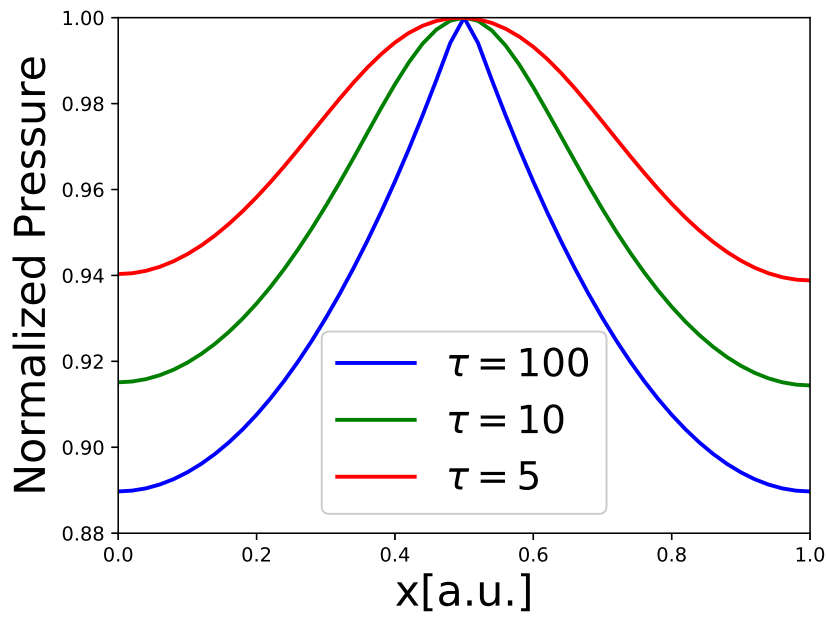
(b) Pressure perturbation.

Figure E.3: True eigenmodes for different values of the velocity shear (τ). Localization of (a) the plasma displacement and (b) the pressure perturbation, around the point of maximum velocity shear. For a true eigenmode, the plasma displacement satisfies boundary conditions.
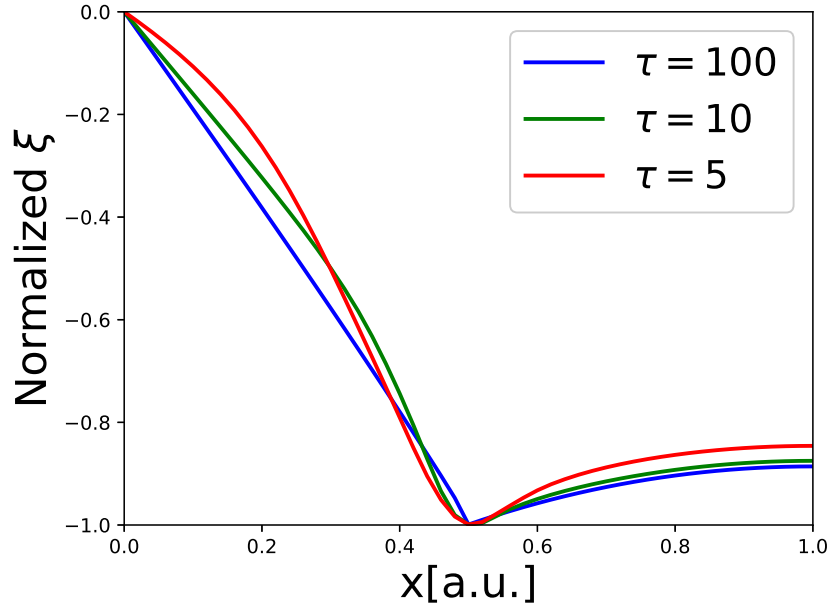
(a) Plasma displacement.
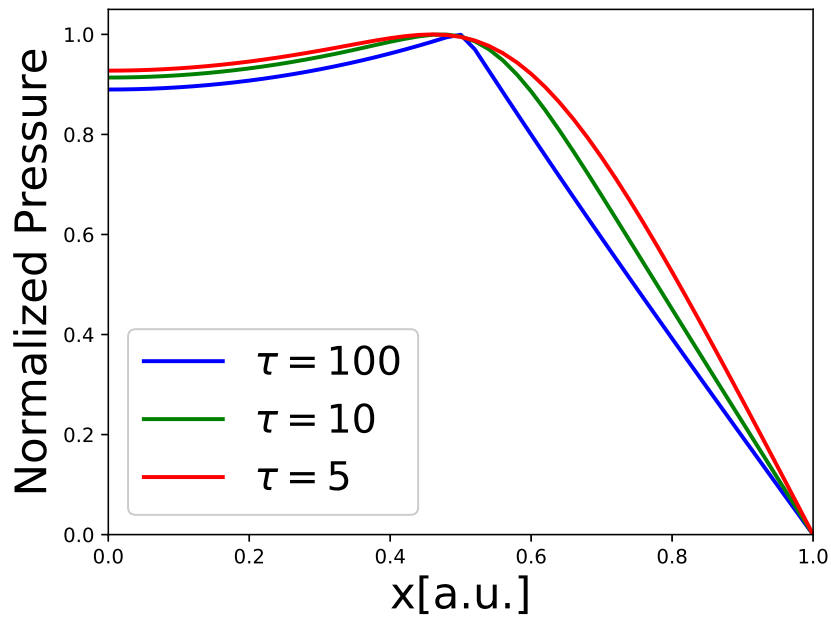
(b) Pressure perturbation.

Figure E.4: False eigenmodes for different values of the velocity shear (τ). (a) The plasma perturbation fails to vanish at the right boundary, (b) For a false eigenmode, it is the pressure perturbation which vanishes at the right boundary.

References

[1] J. D. Lawson. Some criteria for a power producing thermonuclear reactor. *Proceedings of the Physical Society. Section B*, **70**:6, 1957.

[2] J. P. Freidberg. *Plasma Physics and Fusion Energy*. Cambridge University Press, Cambridge UK, 2007.

[3] L. Guazzotto and R. Betti. Tokamak two-fluid ignition conditions. *Phys. Plasmas*, **24**:082504, 2017.

[4] V. D. Shafranov. Hydromagnetic Stability of a Current-Carrying Pinch in a Strong Longitudinal Magnetic Field. *Soviet Physics Technical Physics*, **15**:175, 1970.

[5] J. A. Wesson. Hydromagnetic stability of tokamaks. *Nucl. Fusion*, **18**:87, 1978.

[6] F. Troyon, R. Gruber, H. Saurenmann, S. Semenzato, and S. Succi. MHD-limits to plasma confinement. *Plasma Phys. Control. Fusion*, **26**:209, 1984.

[7] E. J. Strait. Stability of high beta tokamak plasmas. *Phys. Plasmas*, **1**:1415, 1994.

[8] C. Mercier. A necessary condition for hydromagnetic stability of plasma with axial symmetry. *Nucl. Fusion*, **1**:47, 1960.

[9] J. W. Connor, R. J. Hastie, and J. B. Taylor. Shear, periodicity, and plasma ballooning modes. *Phys. Rev. Lett.*, **40**:396, 1978.

[10] ITER Physics Expert Group on Disrup MHD and ITER Physics Basis Editors. Chapter 3: MHD stability, operational limits and disruptions. *Nucl. Fusion*, **39**:2251, 1999.

[11] ITER Physics Expert Group on Confinement Transport, ITER Physics Expert Group on Confinement Database, and ITER Physics Basis Editors. Chapter 2: Plasma confinement and transport. *Nucl. Fusion*, **39**:2175, 1999.

[12] M. Greenwald. Density limits in toroidal plasmas. *Plasma Phys. Control. Fusion*, **44**:R27, 2002.

[13] L. L. Lao and T. H. Jensen. Magnetohydrodynamic equilibria of attached plasmas after loss of vertical stability in elongated tokamaks. *Nucl. Fusion*, **31**:1909, 1991.

[14] A. J. Cerfon and J. P. Freidberg. "One size fits all" analytic solutions to the Grad-Shafranov equation. *Phys. Plasmas*, **17**:032502, 2010.

[15] K. Miyamoto. *Plasma Physics for Nuclear Fusion*. The MIT Press, revised english language edition edition, 1989.

[16] J. P. Freidberg. *Ideal MHD*. Cambridge University Press, Oxford England, 2014.

[17] L. Woltjer. Hydromagnetic equilibrium II. Stability in the variational formulation. *Astrophys. J.*, **130**:405, 1959.

[18] H. P. Zehrfeld and B. J. Green. Stationary toroidal equilibria at finite beta. *Nucl. Fusion*, **12**:569, 1972.

[19] E. Hameiri. The equilibrium and stability of rotating plasmas. *Phys. Fluids*, **26**:230, 1983.

[20] L. Guazzotto and E. Hameiri. A model for transonic plasma flow. *Phys. Plasmas*, **21**:022512, 2014.

[21] V. D. Shafranov. On magnetohydrodynamical equilibrium configurations. *Soviet Phys.-JETP*, **33**:710, 1957.

[22] H. Grad and H. Rubin. *Proc. of the 2nd United Nations Conference on the Peaceful Use of Atomic Energy, United Nations, Geneva*, **31**:190, 1958.

[23] R. Lüst and A. Schlüter. *Z. Naturforschung*, **12a**:850, 1957.

[24] L. S. Solov'ev. *Zh. Eksp. Teor. Fiz.*, **53**:626, 1967.

[25] E. K. Maschke. Exact solutions of the MHD equilibrium equation for a toroidal plasma. *Plasma Physics*, **15**:535, 1973.

[26] R. Kleibergen and J. P. Goedbloed. A high-beta tokamak equilibrium. *Plasma Phys. Control. Fusion*, **30**:1939, 1988.

[27] S. C. Cowley, P. K. Kaw, R. S. Kelly, and R. M. Kulsrud. An analytic solution of high-beta equilibrium in a large aspect ratio tokamak. *Phys. Fluids B*, **3**:2066, 1991.

[28] S. B. Zheng, A. J. Wootton, and E. R. Solano. Analytical tokamak equilibrium for shaped plasmas. *Phys. Plasmas*, **3**:1176, 1996.

[29] P. J. Mc Carthy. Analytical solutions to the gradshafranov equation for tokamak equilibrium with dissimilar source functions. *Phys. Plasmas*, **6**:3554, 1999.

[30] R. H. Weening. Analytic spherical torus plasma equilibrium model. *Phys. Plasmas*, **7**:3654, 2000.

[31] C. V. Atanasiu, S. Günter, K. Lackner, and I. G. Miron. Analytical solutions to the Grad-Shafranov equation. *Phys. Plasmas*, **11**:3510, 2004.

[32] B. Shi. Analytic description of high poloidal beta equilibrium with a natural inboard poloidal field null. *Phys. Plasmas*, **12**:122504, 2005.

[33] L. Guazzotto and J. P. Freidberg. A family of analytic equilibrium solutions for the Grad-Shafranov equation. *Phys. Plasmas*, **14**:112508, 2007.

[34] S. Suckewer, H. P. Eubank, R. J. Goldston, J. McEnerney, N. R. Sauthoff, and H. H. Towner. Toroidal plasma rotation in the PLT tokamak with neutral-beam injection. *Nucl. Fusion*, **21**:1301, 1981.

[35] L-G Eriksson, E. Righi, and K-D Zastrow. Toroidal rotation in ICRF-heated H-modes on JET. *Plasma Phys. Control. Fusion*, **39**:27, 1997.

[36] K. H. Burrell, T. N. Carlstrom, E. J. Doyle, D. Finkenthal, P. Gohil, R. J. Groebner, D. L. Hillis, J. Kim, H. Matsumoto, R. A. Moyer, T. H. Osborne, C. L. Rettig, W. A. Peebles, T. L. Rhodes, H. StJohn, R. D. Stambaugh, M. R. Wade, and J. G. Watkins. Physics of the L-mode to H-mode transition in tokamaks. *Plasma Phys. Control. Fusion*, **34**:1859, 1992.

[37] J. W. Connor and H. R. Wilson. A review of theories of the L-H transition. *Plasma Phys. Control. Fusion*, **42**:R1, 2000.

[38] C. Wahlberg, I. T. Chapman, and J. P. Graves. Importance of centrifugal effects for the internal kink mode stability in toroidally rotating tokamak plasmas. *Phys. Plasmas*, **16**:112512, 2009.

[39] D. Maisonnier, I. Cook, S. Pierre, B. Lorenzo, L. Di Pace, L. Giancarli, P. Norajitra, A. Pizzuto, and PPCS Team. DEMO and fusion power plant conceptual studies in Europe. *Fusion Eng. Des.*, **81**:1123, 2006.

[40] D. Maisonnier, D. Campbell, I. Cook, L. Di Pace, L. Giancarli, J. Hayward, A. Li Puma, M. Medrano, P. Norajitra, M. Roccella, P. Sardain, M.Q. Tran, and D. Ward. Power plant conceptual studies in Europe. *Nucl. Fusion*, **47**:1524, 2007.

[41] J. Li, H. Y. Guo, B. N. Wan, X. Z. Gong, Y. F. Liang, G. S. Xu, K. F. Gan, J. S. Hu, H. Q. Wang, L. Wang, L. Zeng, Y. P. Zhao, P. Denner, G. L. Jackson, A. Loarte, R. Maingi, J. E. Menard, M. Rack, and X. L. Zou. A long-pulse high-confinement plasma regime in the experimental advanced superconducting tokamak. *Nature Physics*, **9**:817, 2013.

[42] R. D. Hazeltine and J. D. Meiss. *Plasma Confinement*. Dover Publicationsm Inc., 2003.

[43] J. A. Almaguer, E. Hameiri, J. Herrera, and D. D. Holm. Lyapunov stability analysis of magnetohydrodynamic plasma equilibria with axisymmetric toroidal flow. *The Physics of Fluids*, **31**:1930, 1988.

[44] D. D. Holm, J. E. Marsden, T. Ratiu, and A. Weinstein. Nonlinear stability of fluid and plasma equilibria. *Physics Reports*, **123**:1, 1985.

[45] E. Frieman and M. Rotenberg. On hydromagnetic stability of stationary equilibria. *Rev. Mod. Phys.*, **32**:898, 1960.

[46] E. M. Lifshitz L. D. Landau and L. P. Pitaevskii. *Electrodynamics of Continuous Media.* ELSEVIER Academic Press, 1981.

[47] J. P. Goedbloed, R. Keppens, and S. Poedts. *Advanced Magnetohydrodynamics*. Cambridge University Press, 2010.

[48] G. B. Arfken and H. J. Weber. *Mathematical Methods for Physicists*. ELSEVIER Academic Press, 2005.

[49] L. R. Baylor, K. H. Burrell, R. J. Groebner, W. A. Houlberg, D. P. Ernst, M. Murakami, and M. R. Wade. Comparison of toroidal rotation velocities of different impurity ions in the DIII-D tokamak. *Phys. Plasmas*, **11**:3100, 2004.

[50] S. A. Sabbagh, A. C. Sontag, J. M. Bialek, D. A. Gates, A. H. Glasser, J. E. Menard, W. Zhu, M. G. Bell, R. E. Bell, A. Bondeson, C. E. Bush, J. D. Callen, M. S. Chu, C. C. Hegna, S. M. Kaye, L. L. Lao, B. P. LeBlanc, Y. Q. Liu, R. Maingi, D. Mueller, K. C. Shaing, D. Stutman, K. Tritz, and C. Zhang. Resistive wall stabilized operation in rotating high beta NSTX plasmas. *Nucl. Fusion*, **46**:635, 2006.

[51] F. Wagner, G. Becker, K. Behringer, D. Campbell, A. Eberhagen, W. Engelhardt, G. Fussmann, O. Gehre, J. Gernhardt, G. v. Gierke, G. Haas, M. Huang, F. Karger, M. Keilhacker, O. Klüber, M. Kornherr, K. Lackner, G. Lisitano, G. G. Lister, H. M. Mayer, D. Meisel, E. R. Müller, H. Murmann, H. Niedermeyer, W. Poschenrieder, H. Rapp, H. Röhr, F. Schneider, G. Siller, E. Speth, A. Stäbler, K. H. Steuer, G. Venus, O. Vollmer, and Z. Yü. Regime of Improved Confinement and High Beta in Neutral-Beam-Heated Divertor Discharges of the ASDEX Tokamak. *Phys. Rev. Lett.*, **49**:1408, 1982.

[52] K. H. Burrell, M. E. Austin, D. P. Brennan, J. C. DeBoo, E. J. Doyle, C. Fenzi, C. Fuchs, P. Gohil, C. M. Greenfield, R. J. Groebner, L. L. Lao, T. C. Luce, M. A. Makowski, G. R. McKee, R. A. Moyer, C. C. Petty, M. Porkolab, C. L. Rettig, T. L. Rhodes, J. C. Rost, B. W. Stallard, E. J. Strait, E. J. Synakowski, M. R. Wade, J. G. Watkins, and W. P. West. Quiescent double barrier high-confinement mode plasmas in the DIII-D tokamak. *Phys. Plasmas*, **8**:2153, 2001.

[53] C. Wahlberg and A. Bondeson. Stabilization of the mercier modes in a tokamak by toroidal plasma rotation. *Phys. Plasmas*, **8**:3595, 2001.

[54] M. S. Chu. Shear flow destabilization of a slowly rotating tokamak. *Phys. Plasmas*, **5**:183, 1998.

[55] W. A. Cooper. Ballooning instabilities in tokamaks with sheared toroidal flows. *Plasma Phys. Control. Fusion*, **30**:1805, 1988.

[56] F. L. Waelbroeck and L. Chen. Ballooning instabilities in tokamaks with sheared toroidal flows. *Physics of Fluids B: Plasma Physics*, **3**:601, 1991.

[57] F. L. Waelbroeck. Gyroscopic stabilization of the internal kink mode. *Phys. Plasmas*, **3**:1047, 1996.

[58] C. Wahlberg and A. Bondeson. Stabilization of the internal kink mode in a tokamak by toroidal plasma rotation. *Phys. Plasmas*, **7**:923, 2000.

[59] M. S. Chu, J. M. Greene, T. H. Jensen, R. L. Miller, A. Bondeson, R. W. Johnson, and M. E. Mauel. Effect of toroidal plasma flow and flow shear on global magnetohydrodynamic MHD modes. *Phys. Plasmas*, **2**:2236, 1995.

[60] R. Betti. Beta limits for the N=1 mode in rotating-toroidal-resistive plasmas surrounded by a resistive wall. *Phys. Plasmas*, **5**:3615, 1998.

[61] L. Guazzotto, R. Betti, J. Manickam, and S. Kaye. Numerical study of tokamak equilibria with arbitrary flow. *Phys. Plasmas*, **11**:604, 2004.

[62] S. Chandrasekhar. *Hydrodynamic and hydromagnetic stability*. International Series of Monographs on Physics. Clarendon Press, Oxford, UK, 1961.

[63] S. Semenzato, R. Gruber, and H. P. Zehrfeld. Computation of symmetric ideal mhd flow equilibria. *Comp. Phys. Rep*, **1**:389, 1984.

[64] A. J. C. Beliën, M. A. Botchev, J. P. Goedbloed, B. van der Holst, and R. Keppens. FINESSE: Axisymmetric MHD Equilibria with Flow. *J. Comput. Phys.*, **182**:91, 2002.

[65] R. Zelazny, R. Stankiewicz, A. Galkowski, and S. Potempki. Solutions to the flow equilibrium problem in elliptic regions. *Plasma Phys. Control. Fusion*, **35**:1215, 1993.

[66] J. W. S. Blokland, B. van der Holst, R. Keppens, and J. P. Goedbloed. PHOENIX: MHD spectral code for rotating laboratory and gravitating astrophysical plasmas. *J. Comput. Phys.*, **226**:509, 2007.

[67] L. Guazzotto and R. Betti. Two-fluid equilibrium with flow: FLOW2. *Phys. Plasmas*, **22**:092503, 2015.

[68] E. K. Maschke and H. Perrin. Exact solutions of the stationary MHD equations for a rotating toroidal plasma. *Plasma Physics*, **22**:579, 1980.

[69] E. K. Maschke and H. J. Perrin. An analytic solution of the stationary MHD equations for a rotating toroidal plasma. *Phys. Lett. A*, **102A**:106, 1984.

[70] G. N. Throumoulopoulos and G. Pantis. Analytic axisymmetric magnetohydrodynamic equilibria of a plasma torus with toroidal mass flow. *Phys. Fluids B*, **1**:1827, 1989.

[71] F. Bacciotti and C. Chiuderi. Axisymmetric magnetohydrodynamic equations: Exact solutions for stationary incompressible flows. *Phys. Fluids B*, **4**:35, 1992.

[72] L. Guazzotto and R. Betti. Magnetohydrodynamics equilibria with toroidal and poloidal flow. *Phys. Plasmas*, **12**:056107, 2005.

[73] E. Hameiri. Variational principles for equilibrium states with plasma flow. *Phys. Plasmas*, **5**:3270, 1998.

[74] E. Hameiri. Quick asymptotic expansion aided by a variational principle. *Phys. Plasmas*, **20**:024504, 2013.

[75] J. P. Goedbloed and L. E. Zakharov. Helical equilibria of a plasma column with a diffuse current distribution. *Nucl. Fusion*, **20**:1515, 1980.

[76] J. M. Greene. An analytic large aspect ratio, high beta equilibrium. *Plasma Phys. Control. Fusion*, **30**:327, 1988.

[77] R. Betti and J. P. Freidberg. Radial discontinuities in tokamak magnetohydrodynamic equilibria with poloidal flow. *Phys. Plasmas*, **7**:2439, 2000.

[78] NIST Digital Library of Mathematical Functions. http://dlmf.nist.gov/, Release 1.0.11 of 2016-06-08. Online companion to [111].

[79] M. Abramowitz and I. Stegun, editors. *Handbook of Mathematical Functions with Formulas, Graphs and Mathematica Tables*. National Bureau of Standards Applied Math Series 55, Washington, DC, 1965.

[80] N. W. McLachlan. *Theory and Application of Mathieu Functions*. Claredon Press, Oxford England, 1951.

[81] J. C. Gutiérrez-Vega, R. M. Rodríguez-Dagnino, M. A. Meneses-Nava, and S. Chávez-Cerda. Mathieu functions, a visual approach. *Am. J. Phys.*, **71**:233, 2003.

[82] Ch. Simintzis, G. N. Throumoulopoulos, G. Pantis, and H. Tasso. Analytic magneto-hydrodynamic equilibria of a magnetically confined plasma with sheared flows. *Phys. Plasmas*, **8**:2641, 2001.

[83] J. P. Goedbloed, D. Pfirsch, and H. Tasso. Instability of a pinch surrounded by a resistive wall. *Nucl. Fusion*, **12**:649, 1972.

[84] J. P. Freidberg and F. A. Haas. Kink instability in a high-β tokamak. *Phys. Fluids*, **16**:1909, 1973.

[85] J. P. Freidberg and F. A. Haas. Kink instabilities in a high tokamak with elliptic cross section. *The Physics of Fluids*, **17**:440, 1974.

[86] J. P. Freidberg and W. Grossmann. Magnetohydrodynamic stability of a sharp boundary model of tokamak. *The Physics of Fluids*, **18**:1494, 1975.

[87] R. Fitzpatrick. A sharp boundary model for the vertical and kink stability of large aspect-ratio vertically elongated tokamak plasmas. *Phys. Plasmas*, **15**:092502, 2008.

[88] Dov J. Rhodes, A. J. Cole, D. P. Brennan, J. M. Finn, M. Li, R. Fitzpatrick, M. E. Mauel, and G. A. Navratil. Shaping effects on toroidal magnetohydrodynamic modes in the presence of plasma and wall resistivity. *Phys. Plasmas*, **25**:012517, 2018.

[89] C. Wahlberg. Analytical stability condition for the ideal m=n=1 kink mode in a toroidal plasma with elliptic cross section. *Phys. Plasmas*, **5**:1387, 1998.

[90] C. Wahlberg. Structure of the compressible MHD equations for the internal kink mode in a toroidal plasma with large aspect ratio. *J. Plasma Phys.*, **62**:165, 1999.

[91] C. Wahlberg. A comparison of compressible and incompressible magnetohydrodynamics in toroidal plasmas. *Phys. Plasmas*, **3**:1619, 1996.

[92] C. Wahlberg and A. Bondeson. Stability analysis of the ideal m=n=1 kink mode in toroidal geometry by direct expansion of the hydromagnetic equations. *J. Plasma Phys.*, **57**:327, 1997.

[93] O. E. López and L. Guazzotto. High-beta analytic equilibria in circular, elliptical, and D-shaped large aspect ratio axisymmetric configurations with poloidal and toroidal flows. *Phys. Plasmas*, **24**:032501, 2017.

[94] M. Kikuchi, T. Takizuka, S. Medvedev, T. Ando, D. Chen, J.X. Li, M. Austin, O. Sauter, L. Villard, A. Merle, M. Fontana, Y. Kishimoto, and K. Imadera. L-mode-edge negative triangularity tokamak reactor. *Nuclear Fusion*, **59**:056017, 2019.

[95] M. E. Austin, A. Marinoni, M. L. Walker, M. W. Brookman, J. S. deGrassie, A. W. Hyatt, G. R. McKee, C. C. Petty, T. L. Rhodes, S. P. Smith, C. Sung, K. E. Thome, and A. D. Turnbull. Achievement of reactor-relevant performance in negative triangularity shape in the DIII-D tokamak. *Phys. Rev. Lett.*, **122**:115001, 2019.

[96] E. Butkov. *Mathematical Physics*. Addison-Wesley Publishing Company, USA, 1968.

[97] A. D. Polyanin. *Handbook of Linear Partial Differential Equations for Engineers and Scientist*. Chapman & Hall/CRC, Oxford England, 2002.

[98] L. C. Steinhauer. Formalism for multi-fluid equilibria with flow. *Phys. Plasmas*, **6**:2734, 1999.

[99] L. C. Steinhauer and A. Ishida. Nearby-fluids equilibria. I. Formalism and transition to single-fluid magnetohydrodynamics. *Phys. Plasmas*, **13**:052513, 2006.

[100] J. P. Goedbloed. Variational principles for stationary one- and two-fluid equilibria of axisymmetric laboratory and astrophysical plasmas. *Phys. Plasmas*, **11**:L81, 2004.

[101] A. Thyagaraja and K. G. McClements. Toroidal and poloidal flows in single-fluid and two-fluid tokamak equilibria. *Phys. Plasmas*, **13**:062502, 2006.

[102] E. Hameiri. Some improvements in the theory of plasma relaxation. *Phys. Plasmas*, **21**:044503, 2014.

[103] A. Ito, J. J. Ramos, and N. Nakajima. High-Beta Axisymmetric Equilibria with Flow in Reduced Single-Fluid and Two-Fluid Models. *Plasma Fusion Res.*, **3**:034, 2008.

[104] H. Helmholtz. *Wissenschaftliche Abhandlungen*. Leipzig Barth, 1882.

[105] Lord Kelvin. *Mathematical and Physical Papers, IV, Hydrodynamics and General Dynamics*. Cambridge University Press, 1910.

[106] I. T. Chapman, S. Brown, R. Kemp, and N. R. Walkden. Toroidal velocity shear kelvin-helmholtz instabilities in strongly rotating tokamak plasmas. *Nucl. Fusion*, **52**:042005, 2012.

[107] J. P. Goedbloed. New construction of the magnetohydrodynamic spectrum of stationary plasma flows. II. Rayleigh-Taylor and Kelvin-Helmholtz instability. *Phys. Plasmas*, **16**:122111, 2009.

[108] J. P. Goedbloed. New construction of the magnetohydrodynamic spectrum of stationary plasma flows. I. Solution path and alternator. *Phys. Plasmas*, **16**:122110, 2009.

[109] J. P. Goedbloed. The spectral web of stationary plasma equilibria. I. General theory. *Phys. Plasmas*, **25**:032109, 2018.

[110] J. P. Goedbloed. The spectral web of stationary plasma equilibria. II. Internal modes. *Phys. Plasmas*, **25**:032110, 2018.

[111] F. W. J. Olver, D. W. Lozier, R. F. Boisvert, and C. W. Clark, editors. *NIST Handbook of Mathematical Functions*. Cambridge University Press, New York, NY, 2010. Print companion to [78].